POLISH ACADEMY OF SCIENCE
COMMITTEE FOR ELECTRONICS AND TELECOMMUNICATIONS

ELECTRONICS AND TELECOMMUNICATIONS QUARTERLY

KWARTALNIK ELEKTRONIKI I TELEKOMUNIKACJI

VOLUME 53 — No 2

WARSAW 2007

Address of Editorial Office
00-665 Warszawa, ul. Nowowiejska 15/19 Politechnika, pok. 470
Instytut Telekomunikacji, Gmach im. prof. JANUSZA GROSZKOWSKIEGO

Editor-on-duty
Wednesdays and Fridays
From 2pm to 4pm
Phone number: (022) 234 77 37

Telephone numbers
Editor-in-Chief: 0607240533
Deputy Editor-in-Chief: 0502660096
Responsible Secretary: 0500044131

Ark. wyd. 9,7 Ark. druk. 7,75	Podpisano do druku w lipcu 2007 r.
Papier offset. kl. III 80 g. B-1	Druk ukończono w lipcu 2007 r.

Publishing
Warszawska Drukarnia Naukowa PAN
00-656 Warszawa, ul. Śniadeckich 8
Tel./fax: 628-87-77

The
Editoria

1. **PUB**
Starting
English
Each art
(e.g. 2 p
must be
correctn

2. **COV**
Starting
is introd
authors
PLN for
financial
next E&
to increa
articles,
In case
amount
In justifi
from bas
into acco
S.A. Wa
Electroni

IMPORTANT MESSAGE FOR THE AUTHORS

The Editorial Board during their meeting on the 18th of January 2006 authorized the Editorial Office to introduce the following changes:

1. PUBLISHING THE ARTICLES IN ENGLISH LANGUAGE ONLY

Starting from No 1'2007 of E&T Quarterly, all the articles will be published in English only.

Each article prepared in English must be supplemented with a thorough summary in Polish (e.g. 2 pages), including the essential formulas, tables, diagrams etc. The Polish summary must be written on a separate page. The articles will be reviewed and their English correctness will be verified.

2. COVERING THE PUBLISHING EXPENSES BY AUTHORS

Starting from No'2007 of E&T Quarterly, a principle of publishing articles against payment is introduced, assuming non-profit making editorial office. According to the principle the authors or institutions employing them, will have to cover the expenses in amount of 760 PLN for each publishing sheet. The above amount will be used to supplement the limited financial means received from PAS for publishing; particularly to increase the capacity of next E&T Quaterly volumes and verify the English correctness of articles. It is neccessary to increase the capacity of E&T Quarterly volumes due to growing number of received articles, which delays their publishing.

In case of authors written request to accelerate the publishing of an article, the fee will amount to 1500 PLN for each publishing sheet.

In justifiable cases presented in writing, the editorial staff may decide to relieve authors from basic payment, either partially or fully. The payment must be made by bank transfer into account of Warsaw Science Publishers The account number: Bank Zachodni WBK S.A. Warszawa Nr 94 1090 1883 0000 0001 0588 2816 with additional note: "For Electronics and Telecommunications Quarterly".

Editors

Elect
Elektrote

The
of Polish
Quarterl
theoretic
recognise
tronics, r

The a
young re

The a
critical e
branch c
mathema
and ISO

All t
specialist
The publ
Science a

The
telecomm
Moreover

Each
distributio
author. Th
accessible

The ar
and the
publicatio
editorial c

The ar
office adc

Dear Authors,

Electronics and Telecommunications Quarterly continues tradition of the ''Rozprawy Elektrotechniczne'' quarterly established 53 years ago.

The E&T Quarterly is a periodical of Electronics and Telecommunications Committee of Polish Academy of Science. It is published by Warsaw Science Publishers of PAS. The Quarterly is a scientific periodical where articles presenting the results of original, theoretical, experimental and reviewed works are published. They consider widely recognised aspects of modern electronics, telecommunications, microelectronics, optoelectronics, radioelectronics and medical electronics.

The authors are outstanding scientists, well-known experienced specialists as well as young researchers – mainly candidates for a doctor's degree.

The articles present original approaches to problems, interesting research results, critical estimation of theories and methods, discuss current state or progress in a given branch of technology and describe development prospects. The manner of writing mathematical parts of articles complies with IEC (International Electronics Commision) and ISO (International Organization of Standardization) standards.

All the articles published in E&T Quarterly are reviewed by known, domestic specialists which ensures that the publications are recognized as author's scientific output. The publishing of research work results completed within the framework of *Ministry of Science and Higher Education* GRANTs meets one of the requirements for those works.

The periodical is distributed among all those who deal with electronics and telecommunications in national scientific centres, as well as in numeral foreign institutions. Moreover it is subscribed by many specialists and libraries.

Each author is entitled to free of charge 20 copies of article, which allows for easier distribution to persons and institutions domestic and abroad, individually chosen by the author. The fact that the articles are published in English makes the quarterly even more accessible.

The articles received are published within half a year if the cooperation between author and the editorial staff is efficient. Instructions for authors concerning the form of publications are included in every volume of the quarterly; they may also be obtained in editorial office.

The articles may be submitted to the editorial office personally or by post; the editorial office address is shown on editorial page in each volume.

Editors

CONTENTS

The

dis
mu
tow
of
are

Ke

In t
standard
ters. It is
standard
tion radi
lopment
of such
ceivers)
architect
tion in v
etc.) in
rates). I

ELECTRONICS AND TELECOMMUNICATIONS QUARTERLY, 2007, 53, no. 2, pp. 107–126

The Parameter-Driven Flexible Front-End for Multi-Mode, Multi-Standard Radio Terminals

ADRIAN KLIKS, HANNA BOGUCKA

Poznan University of Technology Piotrowo 3A,
60-965 Poznań, Poland
akliks@et.put.poznan.pl,
hbogucka@et.put.poznan.pl

Received 2006.10.22
Authorized 2007.02.07

The key aspects of front-ends of the existing and future-developed wireless systems are discussed in this paper. The most promising flexible front-end architectures for multi-mode, multi-standard and multi-band terminals are presented, and new trends in the evolution towards full reconfigurability of front-end architectures are depicted. Critical components of these architectures and their impact on the generalized multicarrier baseband processing are discussed.

Keywords: front-end, multi-mode, multi-standard, flexibility, homodyne, intermodulation

1. INTRODUCTION

In the recent years, the flexibility of wireless transceivers and wideband multi-standard (or multi-mode) operations has gained a lot of attention in many research centers. It is said that reconfiguration of the transceiver and the possibility of using different standards (or modes) at the same time would be the milestones towards fourth generation radio communication systems. One of the main problems in the design and development of the flexible wideband multi-standard transceiver is the RF-part (front-end) of such device. The solution for some particular applications (e.g. dual-mode transceivers) has been presented so far, but the generic flexible multi-standard front end architecture has not been defined, yet. The flexible radio terminal should enable operation in various standards (i.e. WiMAX, UMTS, WiFi, Bluetooth, ZibBee, DVB, DAB etc.) in a variety of modes (i.e. duplex configurations, constellation orders or coding rates). In addition, modes and standards can be described by a set of parameters, and reconfiguration from one mode or standard to another one implies the change of the parameter set values. Such a Canonical Parametric Description (CPD) is one of the key targets in the European project URANUS (*Universal RAdio link platform for efficieNt User-centric accesS*) realized within the framework of Sixth Framework Program in the years 2006–2008 [1].

The main objectives of the URANUS are: to investigate and to design a universal radio link open and flexible platform that can be incorporated in any proprietary or standardized air interfaces, to support simultaneous usage of different available air interfaces and to ease the introduction of future personalized communications and reconfigurable air interfaces. As opposed to the software radio (SR) terminals, where all stages of data signal transmission and detection should be done by the downloaded software, the URANUS terminal will be based on the Generalized Multicarrier Representation (GMCR) of signals generated for multiple standards and modes of operation and canonical parameter description of these signal waveforms. This paper presents the results of research undertaken within URANUS and pertaining to the flexible front-end architectures. After the review of existing flexible front-end realizations, the comparison of the novel solutions in the area of designing the generic flexible front-end has been made, and some proposals are suggested and discussed below. The critical components of such an architecture, and the nature of distortions have also been identified.

2. FLEXIBLE FRONT-END ARCHITECTURES

The idea of a multi-band, multi-standard, reconfigurable, parameter-driven radio terminal such as URANUS implies maximal reduction of almost all analog elements of an RF (*Radio Frequency*) front-end by the means of placing all of them in the digital stage. Nowadays, this solution, even if feasible, has one significant drawback that makes it unrewarding. It puts unrealistic high requirements on an A/D (*Analog/Digital*) converter in terms of a sampling rate and resolution resulting in an unacceptable increase of power consumption in contrast to all existing analog front-ends [2]. Moreover, the LNA (*Low Noise Amplifier*) has to have possibly linear characteristic and work in a wide range of frequency bands.

Let us note, that realization of the receiving front-end chain is a little more complicated than in the case of the transmitting chain. Receiving front-end is a source of serious distortions faced by the receiver baseband part. Therefore, below we concentrate on the receiver front-end design and its critical components. In section 3.2 we also discuss shortly impact of a power amplifier for the transmitter front-end chain on non-linear distortions. In what follows the advantages and drawbacks of the most promising receiver front-end architectures are described.

2.1. HETERODYNE ARCHITECTURE

The generic heterodyne structure is shown in Fig. 1 [3]. The possibility of changing the local oscillator frequencies caused that the heterodyne topology used to be one of the most developed architectures in multi-standard transceivers. With its low noise and low interference performance, the heterodyne topology was one of the most promising approach for multi-standard transceivers. Many solutions have been presented in the literature [3, 4]. One of them, which uses the programmable oscillator is shown below in Fig. 1. This receiver includes some separate receiving paths (each path dedicated to different standard), so the multi-standard idea is realized by multiplexing of receiving and decoding paths.

The major disadvantages of the above discussed heterodyne topology is its inability to support many wireless systems because of the necessity to separate the reception path for each system. Furthermore, this topology is characterized by large complexity of the structure caused by a large number of additional elements (when compared to the other structures), the resulting difficulty in achieving the appropriately high integration and high manufacturer costs. Finally, the heterodyne front-end topology has 50-Ohm load derived by the LNA due to the image rejection filters because the image-rejection filters are placed off-chip.

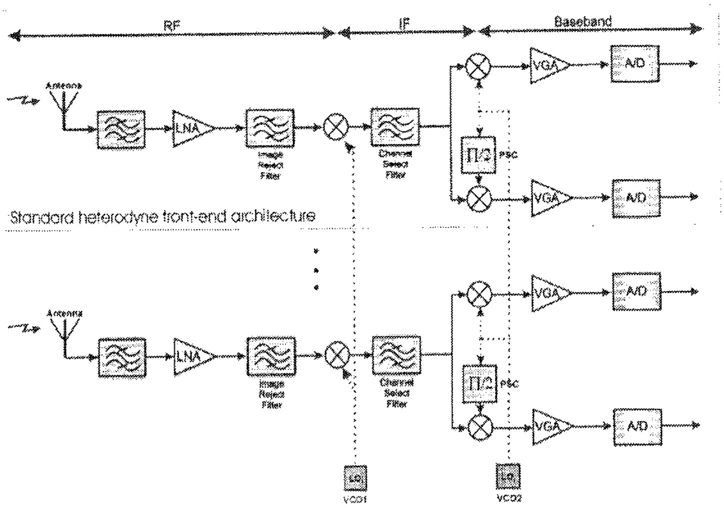

Fig. 1. Multiple-standard heterodyne receiver with programmable local oscillator (highlighted stage is the standard heterodyne receiver front end)

2.2. LOW-IF ARCHITECTURE

Another approach is the so-called low-IF receiver [11], [12]. The second stage of wide-band IF processing could be digitalized only if the chosen intermediate frequency is low enough. The proposed structure is shown in Fig. 2.

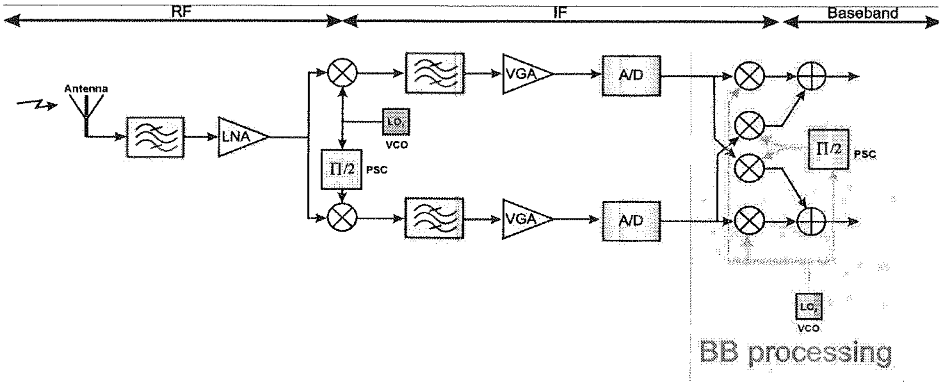

Fig. 2. The architecture of low-IF receiver front-end

The A/D converter is now placed right after the IF band-pass filter and VGA (*Variable Gain Amplifier*). Most of the requirements imposed on the image rejection structure is now shifted to the A/D converter. Moreover, the images occurs in much lower frequencies (comparing with high-IF receiver) so the image reject filters can be placed on-chip. The main disadvantage of low-IF structure is that the mirror signal may be larger than the wanted signal hence the mirror signal suppression is required.

2.3. HOMODYNE ARCHITECTURE

As indicated in the majority of publications (like [6, 7, 8, 9, 10,11]), the homodyne topology is recognized as the most promising architecture for the application in a flexible front-end receiver. Such a homodyne receiver has a decreased number of required elements in comparison with heterodyne structure, what is the milestone towards integration of the front-end elements. The homodyne receiver is also called the zero-IF or direct-conversion receiver. If the IF conversion is not applied, there is no problem with images of the received signal (because the IF frequency is zero), so the image rejection filter is unnecessary. Moreover, the SAW filters (*Surface Acoustic Wave* used in the heterodyne structure as IF filters) are replaced by the reconfigurable low-pass filters that are often integrated with the baseband amplifiers (such configuration is well-suited to monolithic integration [5]). There is no need for LNA to assure 50-Ohm load because of the lack of image rejection filters. The disadvantage of the zero-IF structure is that the offset voltage can corrupt the signal converted to zero frequency and saturate the following stages of a receiver. The DC (*Direct Current*) offset can be generated, for example, by the LO (*Local Oscillator*) leakage signal, which originates from the local antenna emission, signal reflection, and collection of this signal by the same antenna. The LO leakage signal interferes with the desired received signal and causes time-varying DC offset [11]. Besides the time-varying DC offset, the LO leakage signal produces constant DC component. It occurs in the situation when the isolation between LO and LNA is not ideal. The signal from LO can reflect from LNA output, go feedthrough the LNA and return back after amplification. This problem is called self-mixing. The similar effect appears when the received signal passes through the mixer (interference phenomena). The way of the DC component arising is depicted in Fig. 3.

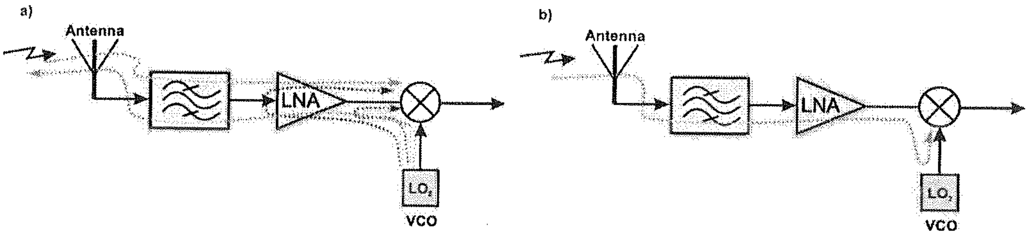

Fig. 3. a) The self-mixing and b) interference phenomena

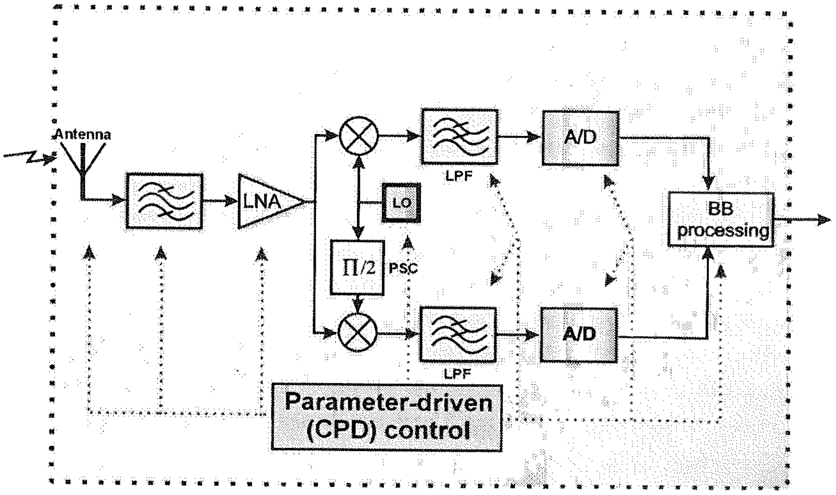

Fig. 4. The architecture of parameter-driven flexible front-end in URAUNS (receiver part); LO – local oscillator, A/D – analog-to-digital converter, LPF – low pass filter, LNA – low noise amplifier, PSC – phase shift circuit

Other drawbacks of the homodyne architecture are the I/Q mismatch that corrupt the constellation diagram, and the presence of the flicker noise whose power is proportional to $1/f$ and which originates from spurious emission of LO leakage signal.

The flicker-noise is located near zero frequency distorting the downconverted signal in zero-IF receiver architecture.

Nevertheless the zero-IF architecture is still considered as a good solution for flexible terminals with the recommendation to shift the digital domain as much as possible towards the antenna [6, 7, 8, 9] and [10].

For the considered application in the URANUS terminal this topology is suggested with the pragmatic approach to the flexible front-end design to control digitally (by the means of a set of parameters) the reconfigurable analog front-end elements. The configuration proposal of such a flexible parameter-driven front-end is presented in Fig. 4.

3. CRITICAL PARAMETERS AND COMPONENTS OF THE PROPOSED FLEXIBLE FRONT-END ARCHITECTURE, THE DESIGN PROCESS AND TESTS

In this section critical parameters which describe front-end distortions are given, and some tests, that are to be performed are shortly presented. Indication of the exact values of the abovementioned parameters can be accomplished as a result of the front-end design process, appropriately tailored to a particular system. The list of the most critical important parameters of the designed flexible front-end are the following:

- Reference Sensitivity Level (RSL) – the minimum input signal level necessary to achieve the required bit error rate,
- Maximum Input Level (MIL) – the upper border of the input power range (all signals with the power higher than MIL are clipped causing in-band distortion like intermodulation products and out-band distortion like interferences due to the signal leakage),
- Adjacent Channel Selectivity – the ratio of the receiver filter attenuation at the appropriately assigned channel frequency to the receive-filter attenuation at the adjacent frequencies,
- Desensitization – the ability of a receiver (usually wide-band receiver) to receive the information signal correctly (i.e. with the pre-defined bit error rate) at the assigned frequency in the presence of nearby narrow-band distortion or jammer signal,
- Isolation – the attenuation between the transmitter and the receiver chain in the transceiver.

During the design and tests of the flexible front-end suggested for the URANUS terminal, the authors identified another set of parameters related to the intermodulation and cross-modulation phenomena. The signals received from different standard-associated channels may be mixed together producing signals of undesired frequencies that distort the received signal in an expected standard or mode. The problem of intermodulation also occurs because of nonlinearity of some elements (e.g. LNA) in the front-end chain. Tests to determine the 2nd (IIP2) and the 3rd (IIP3) order intermodulation intercept point (indicated in Fig. 5) need to be performed.

Cross-modulation has a similar effect as intermodulation but it is usually defined as a result of intermodulation which occurs between separated frequency bands.

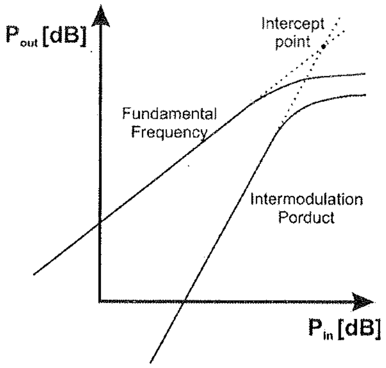

Fig. 5. The intermodulation intercept point

Below the critical components of a flexible front-end are described.

3.1. ANTENNAS

At the first stage of a wireless terminal, front-end antennas with the band-pass filters are located. In a multi-mode, multi-standard terminal such as URANUS the antenna has to serve different system standards and transmit/receive a variety of signals in different frequency bands. Under these circumstances at least two approaches can be applied that solve the antenna system-diversity problem. One solution is a single-feed antenna with the multiplex of the filter characteristics (the usage of one feeder and one filter requires the isolation between systems realized by the multiplex of the filter characteristics used to combine the frequency bands into a multi-band antenna structure with single feeder). The second solution is the multi-feed multi-band antenna structure. The later offers higher SNR and lower power consumption [9] and is proposed for the URANUS transceiver. In addition, when the single-feed antenna is used, the SNR desired to ensure the required BER is higher than in multi-feed antennas.

The contemporary manufacturers produce in most cases only multi-band antennas (dedicated for GSM, ISM bands and to frequencies around 5.8 GHz). The wideband antennas are offered rather very seldom, but if are then the frequency band is around 2–2.5 GHz (usually starting from 800 MHz, so covering GSM and ISM band).

A reconfigurable antenna tunable to different frequency band is presented in [15]. It uses the RF MEMS technology, which can be also applied alternatively in the URANUS transceiver front-end.

3.2. LOW NOISE AMPLIFIERS, HIGH POWER AMPLIFIERS (HPA), SWITCHES AND BALUNS

As mentioned in the previous section, in our proposition for URANUS one multi-standard (multi-band) antenna can be used. When one-antenna solution is chosen, low noise amplifiers must have very high performance, in the sense described in what follows. Because of high requirements (high resolution, high dynamic range, wide frequency band and low power consumption) separate LNAs with separate band-pass filters are placed right after the switch, which connects the antenna to the appropriate decoding path. Such a demultiplexing switch is controlled by the signal from the controller, which is driven by a set of parameters resulting from URANUS canonical parameter description, which identify a particular standard or a set of standards and frequency bands. The proposed architecture, with three different band-pass filters, three separate narrow band LNAs and one switch is shown in Fig. 6. The use of switch is often necessary when both the transmitter and the receiver have to be implemented. Let us note, that some parameters of the RF switch must be considered in the design process; i.e. appropriately wide operating frequency band (in contemporary switches it can be around 4.5 GHz) is desired, fast switching time (around 4–6 ns), low crosstalk, low insertion loss (the attenuation between input and output ports of the switch when the switch control voltage is in the "on" condition; typical value – around 0.2–1 dB at a specific frequency), high off isolation (isolation when the control voltage is off, typical value around 40–60 dB) and low return loss (the amount of reflected power).

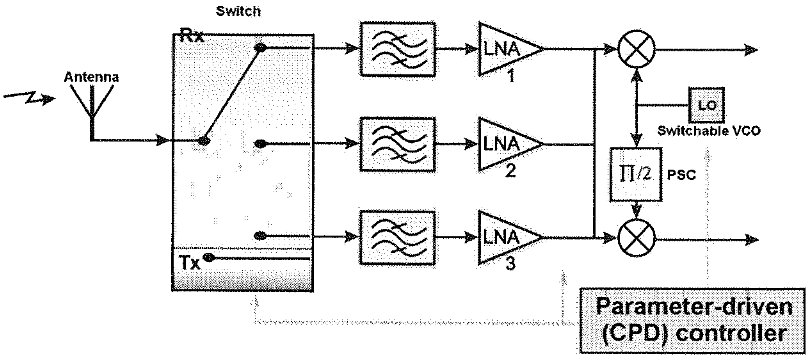

Fig. 6. Multi-standard front-end architecture using a parameter-steered switch in URANUS

The low noise amplifier is one of the critical elements in our flexible front-end design because it should be operative in wide frequency spectrum, have low noise figure, high gain and high linearity. Moreover, power consumption of LNA should be as small as possible. The requirements (for the LNA) usually encompass high linearity of the LNA characteristic, which reduces the intermodulation effects. Two major technologies can be used in LNAs: inductive emitter degeneration and additional charge storage across the base-emitter junction of the transistor [6], [17]. Furthermore, the LNA should be characterized by high stability, which means that oscillations have to be completely eliminated in the whole usable bandwidth when the input and output signals are both terminated in any passive real impedance, and by the low noise-figure. The noise figure of LNA has to be as low as possible. Today's transistors technology focuses on SiGe HBT (Heterojunction Bipolar Transistor – up to 40 GHz), GaAs IC (Integrated Circuit) MESFET and HEMT (up to 50 GHz), PHEMT. Many other solutions are being proposed, that are not yet mature today (like InP IC HEMT, GaN HEMT, GaSb HEMT). Finally, the direct current bias has to be matched upon the requirements with regard to the linearity, stability and the noise figure of an LNA.

On the transmitter side, the high power amplifier (HPA) is placed against of the LNA at the receiver. The requirements, which the HPA should fulfill, are similar to these which are essential in the low noise amplifier design. In the published papers, power amplifiers are realized as multi-stages architectures, where each stage is single-ended construction. The HPA has to be matched to the feeder and to the antenna in order to avoid the mismatch noise. The required isolation between the transmitter and the receiver side has to be assured. Some details about the HPA structures can be found in [16].

Very often the HPA is the main source of nonlinearities on transmitter side. Non-linear characteristic of the HPA and high Peak-to-Average Power Ratio (PAPR) of the transmitted signal (which is the case in multicarrier systems) causes clipping. Tests show, that when clipping occurs at 0.1% of the time, the BER degradation is only 0.1–0.2 dB. At 1% of clipping, the degradation is 0.5–0.6 dB. Besides BER performance degradation, clipping causes energy spilling into adjacent channels, which is a more severe problem.

To avoid clipping, the transmitter power amplifier should work in the linear range of its characteristic. However, this results in undesirable loss of the output power. The Rapp's AM/AM conversion is typical for the power amplifier modeling (output voltage is defined as $V_{\text{out}} = \left(1 + (|V_{\text{in}}|/V_{\text{sat}})^{2p}\right)^{1/2p}$, where V_{in} is the input voltage, V_{sat} is the saturate voltage and p is the smoothness factor). It appears that at the frequency equal to twice the nominal OFDM bandwidth, the power spectral density (PSD) of the ideal OFDM signal, for 64 subcarriers, equals −80 dB. At the same frequency, PSD of the amplified OFDM signal equals −65 dB for Rapp's parameter $p = 10$ and 8.7-dB backoff, and −40 dB for $p = 3$ and 5.3-dB backoff. Thus, the energy leakage out of the nominal bandwidth is quite high, even for a fairly linear power amplifier, i.e. $p = 10$, 8.7-dB backoff.

High PAPR also translates to high requirements for the precision of an D/A converter, and thus, to the system cost. Two methods of mitigating the effects of D/A clipping are usually proposed. One trades off clipping noise against increased quantization noise by scaling a potentially clipped signal. The other one is based on filtering of the clipping noise to reduce its spectral density at low frequencies, where SNR is expected to be higher.

In the URANUS project a particular stress is put upon the PAPR problem and some interesting methods of PAPR reduction are being elaborated. At the receiver side one has to expect nonlinear distortions. Thus, best solution for high PAPR and nonlinearities reduction, in terms of cost and performance, should be elaborated and included in transmitter chain of front-end transmitter. Moreover, the memory effect of HPA cannot be omitted in the case of wide-band systems [18]. The output of the amplifier depends on the actual and previous incoming data. Very often only the low frequency components of signal have significant influence on the memory effect of the HPA.

Some important parameters of the HPA are considered in the design process. These are: the frequency range of work, the gain, the offset voltage (it should be very close to zero, i.e. 100 μV), the offset voltage drift (expressed in μV/°C, input offset voltage changes over temperature, and it could be around ±2μV/°C) and quiescent current (the current that flows in an electrical circuit when no load is present; it should be as low as possible, typical much less than 1 mA). Furthermore, the slew rate (the maximum rate of changes of signal at the amplifier output, defined as $SR = \max\left(\left|\frac{dV_{out}(t)}{dt}\right|\right)$, it is typically around 1–20 V/μs for precision operation amplifier and could be even 5000 V/μs for high-speed amplifiers) and the common-mode rejection ratio (CMRR – a measure of an amplifier ability to reject interference from a common-mode signal; it is usually more than 90dB, and is an important parameter for differential, instrumentation and programmable gain amplifiers) have to be taken into account. Finally, the 1/f noise, Noise Figure (NF) and Total Harmonic Distortion (THD) are to be examined.

Our flexible front-end design also requires that the receiver is matched to the antenna feeder. The flowing currents (with the same amplitude and different directions) in balanced transmission lines induce the symmetric currents in the antenna. The same dependency occurs in the opposite direction, i.e. at the transmitter. When the line is unbalanced, the induced currents have different amplitudes in both directions. So in general, the unbalanced transmission line has to be matched to the balanced antenna. Matching is realized by the balun stage (**bal**anced/**un**balanced).

3.3. LOCAL OSCILLATORS AND MIXERS

Local oscillators, mixers, phase shift circuits (PSC) and voltage controlled oscillators (VCO) are very important elements in the front-end chain. In the design of the URANUS multi-standard receiver, the integration and the parametrization are two of the key aspects, and thus, the application of the programmable voltage controlled oscillator (PVCO) is suggested. Such a local oscillator should be programmable in whole usable bandwidth. In fact, many of actually offered VCOs have the spectrum range around 400 MHz for different frequency regions, but also some products with wide output frequency range (2.5 Ghz) can be found. Additional parameters, like jitter, time to stable output frequency, tuning voltage range (usually the range 0–20 V comprises the typical tuning voltage range), duty cycle at the output (i.e. 50%), phase noise (usually around −100 dBc/Hz), P1dB Compression Point (the point on P_{in} vs. P_{out} graph where an increase power input causes the gain to drop from the linear gain by one dB, typically around 10–13 dBm) etc., have been also considered in the design process.

The LO output signals are created with the aid of, for example, the multi-path phase shift circuits dedicated to separate standards. The 90° phase offsets are produced by frequency dividers (two cross-clocked D-latches) or RC polyphase filter [6].

The last element of this stage is a mixer. The most popular solution of a mixer realization is the Gilbert cell. Gilbert cell is a cross-coupled differential amplifier. The gain value is controlled by changing the emitter bias current. Some details of Gilbert cells can be found in [6], [14]. Fig. 7 shows the solution of a reconfigurable mixer with matching proposed in [14]. Matching to the multi-system antenna block (the block which consists of different antennas with LNAs for separate systems or tunable antenna) is realized using the method of switching transistors, capacitors and inductors. While chosing the mixer, some parameters should be examined – e.g. the operating frequency ranges (RF, IF and LO frequency range). Here, the various solutions are offered: starting from RF in the range of 10–1500 MHz, IF 10–1500 MHz and LO DC-800 MHz to RF in the range of 0.5–18 GHz, IF 0.5–18 GHz and LO DC-0.3 GHz. Moreover, compression point and isolation RF-IF, RF-LO and LO-IF (around 20–30 dB) play an important role.

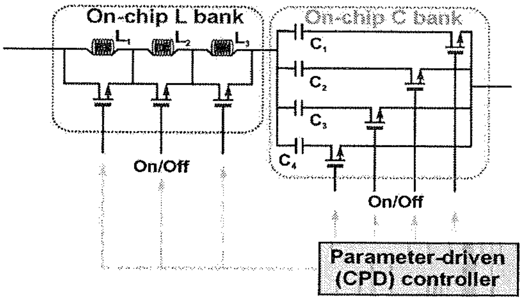

Fig. 7. Flexible matching input block in the URANUS front-end

3.4. A/D AND D/A CONVERTERS

Analog-to-digital and digital-to-analog converters seem to be the most critical elements in the proposed flexible front end architecture. An approach with fully digitalized IF/RF part puts extremely high requirements on the A/D and D/A converters. The converters should have very wide bandwidth, high resolution and dynamic range. Although the usage of $\Delta\Sigma$-converters before the LNA and the band-pass filter (that comply with these requirements) at the receiver is feasible, power consumption of these devices is not acceptable. Therefore the digitalization stage should rather be placed in another (earlier) location in the receiving chain. In such case many other

A/D structures could be applied in flexible front-ends. They have been investigated, designed and tested, e.g. pipeline or cyclic sigma-delta converters [19]. The structure and parameters of an A/D converter depend on the chosen receiver architecture.

The most popular A/D converter structure is the above mentioned $\Delta\Sigma$-converter. In our consideration in the choice of the architectures which can act as multi-standard A/D converter for URANUS front-end receiver we have taken a few solution into account. The authors have identified their potential to be applied in the designed front-end. The simplest, yet area-wasting and expensive solution is to multiply the number of separate A/D converter dedicated to different standards. The use of switched-capacitor (SC) technology in A/D converter designing process has gained a lot of attention in many research laboratories [2], [13], [20]. The SC A/D converter has the inherent ability of good matching to analog and digital filter parameters which is required in the cascaded realizations of converters. The continuous time (CT) sigma-delta modulators allow to use the loop filter as an anti-aliasing filter. For this reason, CT modulators gain the popularity over their counterparts – discrete-time (DT) modulators. Moreover, the problem of high oversampling of high-resolution sigma-delta converters can be easily solved by the use of cascaded modulators in which the oversampling ratio is 8 or 16. The design of high dynamics, 10 MHz bandwidth cascaded $\Delta\Sigma$-modulators with good noise-canceller filter is presented in [22]. Finally, an interesting idea of a reconfigurable analog-to-digital converter is described in [19]. The proposed structure can work in pipeline or sigma-delta mode, and has the advantages of these particular topologies. Reconfigurability is realized in three stages – reconfiguration of architecture, change of parameters and adjustment of frequency bandwidth. This architectural solution seems to be the best suited for our design.

Let us note, that some electronic producers offer the converters with the resolution ranging form less than 8 bits to 24 bits. But when the resolution increases the maximum throughput-rate decreases (i.e. for 8 bit resolution A/D converter the maximal throughput-rate is around 100 MSPS, when for 24 bit resolution converter it is around 1 kSPS; SPS stands for samples per second).

On the transmitter site D/A converters are used, which are realized also by the means of $\Delta\Sigma$-modulators because of their good trade off between high-resolution and power consumption. Similar to A/D converters, the CT converters gain the popularity over the DT modulators [23, 24] and we suggest them for our case also.

Beside the obvious parameters of A/D and D/A converters, like resolution, throughput-rate, gain error, effective number of bits (ENOB – a measure of the resolution with a sine wave input, and expressed as $ENOB = (SINAD_{dB} - 1.76)/6.02$, where SINAD is Signal to Noise And Distortion power ratio, usually around 80–90 dB), some additional parameters should be taken into account, i.e. Total Harmonic Distortion (THD, around −90 dB), input signal amplitude range and Spurious-Free Dynamic Range (SFDR is the difference between the rms amplitude of the input signal and the peak spurious signal; in other words it is also the dynamic range of converter before the spurious

stigated,
structure
re.
verter. In
lard A/D
account.
ont-end.
mber of
apacitor
attention
inherent
ed in the
odulators
tors gain
over, the
be easily
8 or 16.
ith good
figurable
work in
ologies.
hange of
n seems

esolution
he maxi-
maximal
s around

o by the
tion and
pularity

through-
tion with
INAD is
dditional
, around
SFDR is
spurious
spurious

---

peaks of noise starts interfering the original signal; typical values of SFDR are within the range 70–95 dB).

4. COMPUTER SIMULATIONS AND EXPERIMENTS

Although a variety of multi-standard, multi-mode and multi-band flexible front-ends exists, they are usually dedicated to a specific set of standards (e.g. GSM with WCDMA [9], GPS with UMTS [12, 13]) they are supposed to support. The main conclusion is that the generic flexible front – end supporting more than 2–3 standards has not been developed until now. It has to be mentioned that the multi-standard and multi-band front-end has an impact on the signal in the baseband which in turn depends on a chosen front-end topology. Once the topology is chosen, the influence of it on baseband signal should be considered. One of the most important phenomena that occur in every multi-band receiver front-end, which can influence negatively the baseband signal are the intermodulation and cross-modulation effects, which result from nonlinearities of active elements. Table 1 shows the frequency bands of possible standards of wireless systems that should be received correctly by the URANUS terminal.

Table 1

The frequencies of possible wireless systems supported by the URANUS platform

System	Central frequency
WCDMA – UMTS	Tx: 1920 – 1980 MHz, fc = 1950 MHz (FDD) Rx: 2110 – 2170 MHz, fc = 2140 MHz (FDD) Tx: 1900 – 1920 MHz, fc = 1910 MHz (TDD) Rx: 2010 – 2025 MHz, fc = 2012.5 MHz (TDD)
GSM, DCS, PSC	Tx: 935 – 960 MHz, 1805 – 1880 MHz, 1850 – 1910 MHz Rx: 890 – 915 MHz, 1710 – 1780 MHz, 1930 – 1990 MHz
802.11a	5,15 – 5,35 GHz, 5,725 – 5,825 GHz
802.11b	2,4 GHz
802.11n	2,4 or 5 GHz
DVB-T/H	VHF (30–300 MHz) UHF (300 MHz – 3 GHz)
802.16a,e	2,3 GHz, 2,5–2,7 GHz, 3,4–3,6 GHz (licenced) ISM 2,4 GHz; U-NII 5,725–5,850 GHz
Bluetooth	2,45 GHz (2,4–2,4835 GHz)
ZigBee	2,4 GHz; 868–870 MHz (EU) 902–928 (USA)

In order to verify the impact of the inter- and cross-modulation products on the received URANUS signal, computer simulations have been performed. Eight transmission radio frequencies have been chosen as shown in Fig. 8, where the results of such simulation are presented.

In this figure lines with the highest amplitude are the fundamental frequencies, the lines with smaller amplitude are the second-, third- and fifth-order intermodulation products respectively. Only the positions of the intermodulation products on the frequency axis are shown in Fig. 8, and no conclusion about their amplitudes |A(f)| can be drawn, because the values of amplitudes of intermodulation products depend on the power, the frequency value of the fundamental (desired) signals and the device characteristic (see the Rapp model of HPA in sec. 3.2).

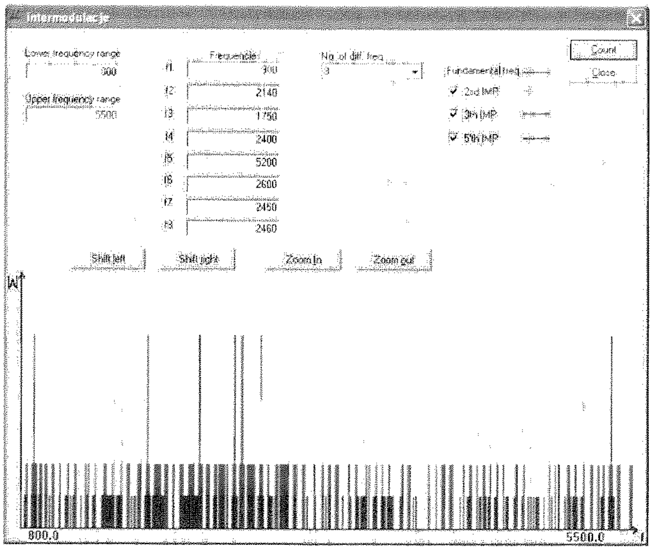

Intermodulacje

Lower frequency range: 800

Upper frequency range: 5500

Frequencies:
f1: 900
f2: 2140
f3: 1750
f4: 2400
f5: 5200
f6: 2600
f7: 2450
f8: 2460

No. of diff. freq: 8

Fundamental freq.
☑ 2nd IMP
☑ 3th IMP
☑ 5th IMP

Fig. 8. The intermodulation phenomena in multi-standard receiver

It is shown that although only eight different frequencies in a multicarrier signal were considered a large number of intermodulation products arose. The positions f_x of IMD products on the frequency axis can be expressed as follow: $f_x = f_a \pm f_b$ for second order IMD products and $f_x = 2f_a \pm f_b$ and $f_x = 2f_b \pm f_a$ for third order IMD product (if only two fundamental f_a and f_b frequencies are taken into account). The IMD products of higher orders could be defined in a similar way. The intermodulation products corrupt the signal in the baseband. It is especially important when mulitcarrier systems are considered because the presence of intermodulation products increase the noise floor and the Noise Figure (NF) at the same time (see Fig. 9). The increase of NF level reduces the receiver sensitivity, and puts higher requirements on the several elements in the front-end chain.

To investigate the influence of intermodulation products on the Noise Figure in receiver chain extensive experiments have been carried. The experiments aim at showing the increase of Noise Figure in the power amplifier, when it works in non linear range of its characteristic, and the input signal is the summation of two signals of equal power but of different frequencies. These two signals have been generated by the RF Signal Generators (R&S SMIQ02B and R&S SMH845.4002.52), then summed in the power divider (R&S RVZ800.6612.52) and amplified by the power amplifier (whose bandwidth 5 kHz÷400 MHz). The Y3-33 power amplifier has been intentionally selected to observe the effect of NF increase. The intermodulation products have been observed on the spectrum analyzer (R&S FSH3). The measurement equipment setup is presented in Figure 10.

Fig. 9. The effect of intermodulation in the multi-carrier GMCR receivers; from the left: "small" multi-carrier and typical multi-carrier system

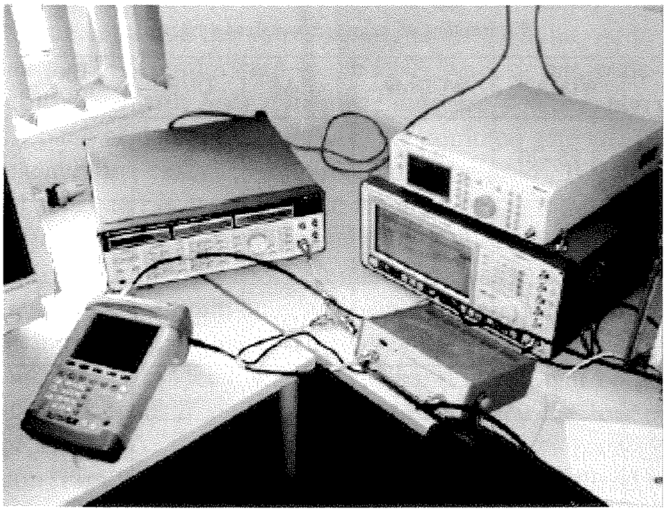

Fig. 10. The equipment used for the Noise Figure measurements

The results from the experiment show, that the Noise Figure of the power amplifier can increase up to 1 dB. This high value of the Noise Figure is caused by the fact that the power amplifier operates in the non-linear range of its characteristic. The results of this experiment prove that the intermodulation products have significant impact on the NF value in non-linear devices.

5. FLEXIBLE FRONT-END FOR THE MULTI-STANDARD TERMINAL. DISCUSSION ON THE PROPOSED SOLUTION

Let us note, that one of the recommendations for the URANUS terminal design is to investigate efficient HW/SW architectures which can be shared and combined with each other for implementing the transceiver in a modular structure. Thus, it is needed to reduce the coverage of Printed Circuit Boards PCB (e.g. by using the SoC or SiP technology) and to minimize the power consumption of used elements (minimization of power is particularly important in case of a multi-standard front-end which entail the use of power-hungry elements like $\Delta\Sigma$-modulators or LNA). Therefore, for the URANUS terminal front-end, zero-IF topology has been chosen. Direct conversion structure eases the integration of elements in the front-end chain and decreases the expenditure of energy because of the lack of an additional local oscillator (IF LO), image reject filter and additional chanellization filters. By the same reason the footprint of the front-end will also decrease.

In Table 2 some characteristic parameters of systems possibly supported by the URANUS platform are summarized.

Table 2

Parameters of selected wireless systems

Parameter	WiMAX	WCDMA	GSM	DVB	Blue-tooth	802.11a/b
Signal Bandwidth [MHz]	1.25–20	3.84	0.2	8	1	20/22
Maximum input power [dBm]	−20	−25	−15	−1	−14	−10
Reference sensitivity [dBm]	−92	−110	−100	−98	−83	−65/−83
NF [dB]	2	3	3	3	5	14,8/7.5
Required resolution in A/D converter [bits]	7–10	6–8	12–14	10–14	13	10–14/6–8

Analyzing these characteristics and the information placed in Table 1 the following conclusions regarding the front-end suggested for the URANUS terminal should be drawn:

a) the range of RF frequencies is between 900 MHz to 6 GHz, so very wide-band elements (including LNAs) are required,
b) the URANUS terminal has to receive signals whose power is between −110 dBm and −1 dBm; thus, the dynamic range of the transmission RF signal will be ~109 dB
c) A/D converter used in the URANUS receiver front-end has to work with variable resolutions (to decrease the power consumption) – from 6 to 14 bits,
d) the smallest Noise Figure (2 dB) should be ensured, in order to receive signals of any of the standards listed in Table 2 at any time.

As an example, let us consider three existing wireless system standards: GSM, UMTS and WiMAX. Analyzing previous tables it is easy to see that in this case the dynamic range is decreased from 109 dB to 92 dB. However, the other aspects like the frequency ranges and the variable A/D or D/A converters resolutions remain unchanged. On the basis of this conclusion the zero-IF front-end with three separate receiving paths is still recomended.

The RF signal is collected by the multi-band antenna but it is also possible to use three separate antennas. In fact, WiMAX can operate in one of three different bands – located around 2.4, 3.7 and 5.8 GHz, so three separate antennas would be needed in order to support these standards. Due to such situation four or five antennas are required to cover all frequency bands of interest (GSM, UMTS and WiMAX). The proposal of one multi-band antenna seems to be better because of lower costs and the footprint reduction. After the signal is collected by the receiving antenna – it is filtered in a bank of the filters (the Surface Acoustic Wave filters or the LC filters). There should be a switch between the antenna and the above mentioned filter bank. After this filter bank the received signal goes straightforward to the LNA bank or one wide-band amplifier. The wide-band amplifiers with high dynamic range are power hungry, therefore the best solution is the bank of narrow band LNAs (the common gate and the common gate with inductive degeneration cascaded amplifier could be used). It should be mentioned that the number of separate LNA and band pass filters can be minimized by using some multi-band filters and LNA (for example, one filter and one LNA for frequency bands about 2.4 and 3.7 GHz). Moreover these elements can work in parallel what is always advantageous when a flexible multi-standard front-end is considered [26]. The chosen LNA should have appropriate NF especially, when the wide-band LNA is selected. By preceding the LNA by LC ladder filter the wideband match can be achieved and the NF level remains unchanged. If multi-band LNA is chosen the lowest NF has to be achieved (2dB for WiMAX).

The conversion from the RF band to the baseband can be realized by the programmable LO. In order to eliminate or to minimize the phase shift error when converting the signal to the in-phase and quadrature components, specialized frequency divider or polyphase filter should be used. The mixer could be realized with the aid of Gilbert cells. After mixer and typical low-pass filters the analog-to-digital converter is to be placed. This A/D converter could be CT ΔΣ-modulators because of their high dynamic range.

5.1. CPD ORIENTED CONTROL OF THE FLEXIBLE FRONT-END ELEMENTS

Based on the considerations presented above the following parameter set of the URANUS Canonical Parametric Description (see Section 1) is suggested to control the operation of the flexible front-end elements:

- the antenna parameter – the bandwidth of the antenna (in the case of reconfigurable antenna) or selection of one of the used antennas. (When the wide-band antenna is used this parameter could be set to "default");
- the switch parameter – defining connections between selected antenna and the appropriate decoding path/band pass filter, or defining a switch (decoding path). Usually the switch has strictly defined input frequency bandwidth that does not cover the whole frequency band for all existing and future systems. In such a case there should be a bank of switches;
- the filters parameter – defining the appropriate decoding (coding) path by selecting one filter (in the case of a filter bank) or defining the band of a filter (in the case of a tunable filter);
- the amplifiers (LNA, HPA) parameter – defining the gain parameter, or choosing appropriate amplifier when the bank of amplifiers is used;
- the mixer parameter – frequency band (usually the mixer has a sufficient frequency band to cover the frequencies for some systems, but for the ideal case the separate mixers should be used),
- the VCO parameter – the value of voltage required to generate the appropriate frequency or to choose one VCO from the VCO set (in the case when all systems should be decodable);
- the A/D and D/A converter parameter – defining the appropriate resolution to achieve possibly high reduction of power consumption.

6. CONCLUSIONS

Let us summarize some future trends concerning flexible front-end components and design. The evolution of the flexible RF front-end design has the following noticeable directions:

- frequency ranges of wireless systems are becoming higher, so novel microwave technologies like RF-MEMS (*Radio Frequency Micro-ElectroMechanical Systems*) are subjects of intensive research;
- produced chips are expected to have the MMIC (*Monolithic Microwave Integrated Circuit*) or HIC (*Hybrid IC*) form [21];

- application of SiGe transistors, Heterojunction Bipolar Transistors (HBT) and microstrip transmission lines is seriously considerated;
- the integration of all transceiver elements (called packaging), including front-end elements is a visible trend, so the SoC or SiP with thin-film technology are taken into account in contemporary research [25].

Various topologies of the flexible front-end architectures have been presented in this paper. The advantages and drawbacks of each of them have been discussed. Despite the long time, the heterodyne topology was suggested as a solution for multi-standard, multi-band realizations, the necessity of high integration of passive and active elements in a transmitting and receiving chain caused that the zero-IF architecture focused the attention of many researchers worldwide. The studies and tests on the direct-conversion front-end led to elaboration of many concepts that alleviate and suppress the effect of the undesired phenomena which distort the signal in typical zero-IF receiver front-end (i.e. DC offset, I/Q mismatch etc.). Under these circumstances the homodyne receiver seems to be the best topology for the URANUS terminal.

Critical front-end elements, their parameters and tests that should be the part of the design process have been presented. Their impact on the multi-standard terminal (such as the URANUS transceiver) baseband signal distortions have been discussed, and some ways to omit or reduce them have been suggested. Moreover, subsequent stages and components of the URANUS receiver and the transmitter front – end have been discussed, as wall as their CPD parameter-driven control.

7. REFERENCES

1. www.ist-uranus.org
2. G. Gielen, E. Goris: *Reconfigurable front-end architectures and A/D converters for flexible wireless transceivers for 4 G radios*, IEEE 7th CAS Symposium on Emerging Technologies: Circuits and Systems for 4G Mobile Wireless Communications, June 2005.
3. http://bwrc.eecs.berkeley.edu/Research/MCMA/
4. R.R.-B. Sheen, O.T.-C. Chen: *A CMOS PLL-Based Frequency Synthesizer for Wireless Communication Systems at 0.9, 1.8, 1.9 and 2.4 GHz*, ISCAS, Vol. 4, May 2001, pp. 722-725.
5. B. Razavi: *Design Considerations for Direct-Conversion Receivers*, IEEE Transactions on Circuits and Systems – II: Analog and Digital Signal Processing, Vol. 44, No. 6, June 1997, pp. 428-435.
6. M. Hotti, J. Kaukovouri, J. Ryynänen, K. Kivekäs, J. Jussila, K. Halonen: *A Direct Conversion RF Front-End for 2-GHz WCDMA and 5.8-GHz WLAN Applications*, IEEE Radio Frequency Integrated Circuits Symposium, June 2003, pp. 45-48.
7. X. Li, M. Ismail: *A Single-Chip CMOS Front-End Receiver Architecture for Multi-Standard Wireless Applications:*, ISCAS, Sydney, Australia, May 2001, Vol. 4, pp. 374-377.
8. D. San, J. Xu: *Zero-IF topology*, Electronic Letters, Vol. 36, No. 12, 8th June 2000, pp. 1009-1010.
9. S. Spiegel, I.I.G. Kovacs: *An Efficient Integration of GPS and WCDMA Radio Front-Ends*, IEEE Transactions of Microwave Theory and Tech., Vol. 52, No. 4, April 2004, pp. 1125-1131.
10. Z. Shi, R. Rofougaran: *A Single-chip and Multi-mode 2,4/5GHz RF Transceiver for IEEE 802.11 Wireless LAN*, ICMMT, Aug. 2002, pp. 229-238.

11. A. Springer, L. Maurer, R. Weigel: *RF System Concepts for Highly Integrated RFICs for W-CDMA Mobile Radio Terminals*, IEEE Transactions on Microwave Theory and Techniques, Vol. 50, No.1, Jan. 2002, pp.254-267.
12. M. Wang, R.-B. Sheen, O.T.-C. Chen, T. Y. J. Tsen: *A Dual-Band RF Front-End for WCDMA and GPS Applications*, ISCAS, May 2002, pp. 113-116.
13. T. Burger, Q. Huang: *A 13.5-mW 185-Msample/s $\Delta\Sigma$ Modulator for UMTS/GSM Dual-Standard IF Reception*, IEEE Journal of Solid-State Circuits, Vol. 36, No. 12., Dec. 2001, pp. 1868-1878.
14. C. Kim, T. Jang, H. Yoo: *Design of Multi-standard (IEEE 802.11a/b/g and WCDMA) RF Front-end Using Reconfigurable Mixer*, Digest of Technical Papers. ICCE IEEE, June 2005, pp. 413-414.
15. J. Aberle, S.-H. Oh, D. Auckland, S. Rogers: *Reconfigurable Antennas for Portable Wireless Devices*, IEEE Antennas and Propagation Magazine, Vol. 45, No. 6, December 2003, pp. 148-154.
16. C.-H. Lee, S. Chakraborty, A. Sutono, S. Yoo, D. Heo, J. Laskar: *Broadband Highly Integrated LTCC Front-end Module for IEEE 802.11a WLAN Applicaiotns*, IEEE MTT-S Digest, 2002, pp. 1145-1148.
17. G. Wevers: *A High IIP3 Low Noise Amplifier for 1900 MHz Applications Using the SiGe BFP620 Transistor*, Applied Microwave & Wireless, Jan. 2000, pp. 64-80.
18. H. Zhi-yong, G. Jian-hua, G. Shu-jian, W. Gang: *An Improved Look-Up Table Predistortion Techniques for HPA With Memory Effects in OFDM Systems*, IEEE Transactions on Broadcasting, vol. 52, No. 1, March 2006, pp. 87-91.
19. K. Gulati, H. Lee: *A Low-Power Reconfigurable Analog-to-Digital Converter*, IEEE Journal of Solid-State Circuits, Vol. 36, No. 12, Dec. 2001, pp. 1900-1911.
20. M. Laddomada, F. Daneshgaran, M. Mondin, R.M. Hickling: *A PC-Based Software Receiver Using a Novel Front-End Technology*, IEEE Communications Magazine, Aug. 2001, pp. 136-145.
21. S. Mirabbasi, K. Martin: *Classical and Modern Receiver Architecture*, IEEE Communications Magazine, Vol. 38, Nov. 2000, pp. 132-139.
22. L.J. Breems, R. Rutten, G. Wetzker: *A Cascaded Continuous-Time $\Delta\Sigma$ Modulator With 67-dB Dynamic Range in 10-MHz Bandwidth*, IEEE Journal of Solid-State Circuits, Vol. 39, No. 12, Dec. 2004, pp. 2152-2160.
23. M. Ortmanns, F. Gerfers, Y. Manoli: *A Continuous-Time Modulator With Reduced Sensitivity to Clock Jitter Through SCR Feedback*, IEEE Transactions on Circuits and Systems, vol. 52, No. 5, May 2005, pp. 875-884.
24. K.T. Tiew, Y. Chen: *DAC Compensation for Continuous-Time Delta-Sigma Modulators*, ISCAS, vol. 4, May 2005, pp. 3680-3683.
25. http://www.imec.be
26. H. Hashemi, A. Hajimiri: *Concurrent Multiband Low-Noise Amplifiers – Theory, Design and Applications*, IEEE Transactions on Microwave Theory and Techniques, vol. 50, No. 1, January 2002.

ELECTRONICS AND TELECOMMUNICATIONS QUARTERLY, 2007, 53, no 2, pp. 127-141

Fourier Analysis of Motor Unit Action Potentials

ANDRZEJ DOBROWOLSKI[1], KAZIMIERZ TOMCZYKIEWICZ[2], PIOTR KOMUR[1]

[1] *Military University of Technology, Faculty of Electronics*
2 Kaliskiego St., 00-908 Warsaw, Poland
ADobrowolski@wat.edu.pl; PKomur@wat.edu.pl
[2] *Military Institute of Health Service, Department of Neurology*
128 Szaserow St., 00-909 Warsaw, Poland
kaziura@wim.mil.pl

Received 2006.12.11
Authorized 2007.03.27

Electromyography (*EMG*) is a functional examination that plays a fundamental role in the diagnosis of neuromuscular disorders. The method allows for distinction between records of a healthy muscle and a changed muscle as well as for determination of whether pathological changes are of primary myopathic or neuropathic character.

The statistical processing of electromyographic signal examination performed in the time domain ensures mostly correct classification of pathology; however, because of an ambiguity of most temporal parameter definitions, a diagnosis can include a significant error that strongly depends on the neurologist's experience. Then, selected temporal parameters are determined for each run, and their mean values are calculated. In the final stage, these mean values are compared with a standard and, including additional clinical information, a diagnosis is given. An inconvenience of this procedure is high time consumption that arises from, among other things, the necessity of determination of many parameters. Additionally, an ambiguity in determination of basic temporal parameters can cause doubts when parameters found by the physician are compared with standard parameters determined in other research centers.

In this paper, we present a definition for single-point spectral discriminant that directly enables a unique diagnosis to be made. An essential advantage of the suggested discriminant is a precise and algorithmically realized definition that enables an objective comparison of examination results obtained by physicians with different experiences or working in different research centers. Therefore, the definition fulfills a fundamental criterion for the parameter used for preparation of a standard. A suggestion of the standard for selected muscle based on a population of 70 healthy cases is presented in the Results section.

Keywords: quantitative electromyography (QEMG), motor unit action potential (MUAP, MUP), FFT spectrum

1. INTRODUCTION

Electromyography allows for:

- distinction between records of healthy and changed muscles;
- determination whether pathological changes are of primary myopathic or neuropathic character;
- determination of pathological process localization or whether the process has a generalized character;
- estimation of process dynamics;
- differentiation between paresis of central origin and peripheral or psychogenic ones.

Electromyography is often complemented with *electroneurography* (*ENG*) i.e. testing of conductivity in sensory and motor nerve fibers.

Muscular fibers have diameters from 10 to 100 μm and lengths from 1 mm up to a dozen or so centimeters. A group of muscular fibers innervated by a single *motor neuron* creates so-called *motor unit* (*MU*), comprising:

- the cell of the anterior horn of the spinal cord or motor nucleus of the cranial nerve together with a nerve axon,
- innervated by this cell muscular fibers,
- end-plates creating connections between nerve terminals and muscular fibers.

Muscular fiber contraction may be considered as a biochemical process strictly related to electrical stimula-tion of the membrane, i.e. action potential of a muscular fiber. Electrical stimulation can be explained on the base of ion theory in which cell stimulation can be reduced to the change of membrane permeability for so-dium and potassium ions. Resting potential is a result of electrochemical gradient of ions spacing and differ-ent membrane permeabilities for individual ions. It is formed mainly by sodium, potassium, and chloride ions. Electrochemical gradient is maintained due to permanent activity of sodium-potassium pump which is responsible for active ion transport.

A pulse propagating in a motor nerve releases acetylocholine in the end-plate which transfers the stimulation into muscular fiber. During stimulation there occurs a rapid transient conversion of the mem-brane potential from negative to positive one, so-called a *depolarization*. Return to initial state is called a *repolarization*. This process is called an *action potential*, and it is accompanied by a flow of current created in result of permeability changes for sodium and potassium ions. The action potential starts in the vicinity of end-plate and propagates along the fiber with a velocity of 1.5–6 m/s (depending of a fiber type) simulta-neously incorporating membrane of transverse tubule. Depolarization of these structures releases rapidly calcium ions from nerve terminals to cytoplasm, which results in muscular fiber contraction.

Changes in individual elements of a motor unit are the reason for neuromuscular disorders. *Myopathies*, i.e., muscle diseases, and *neuropathies*, i.e., nerve diseases, are recognized. Disease changes can also include a muscle-nerve junction and then undergo electrophysiological examination. A clinical pic-ture of myopathy shows a presence of, among others, characteristic electromyographic changes, i.e., *myopathic pattern*, and in the case of neuropathy – *neuropathic pattern*.

The EMG examination consists of the insertion of a needle electrode into a muscle and a registration of muscle potentials at rest and during low and maximum effort. During examination, the electrode is repeatedly shifted in order to evaluate different muscle regions. Registered potentials are called *motor unit action potentials* (*MUAPs, MUPs*). MUAP presents a curve which shows a depolarization and repolarization of muscular fiber and curve character gives an information on correct or incorrect electrical activity of a motor unit. Muscle tissue is normally electrically silent at rest. When a loose muscle is pricked on a needle electrode only momentary spontaneous activity as a muscle membrane excessive excitation is correct. A presence of a prolonged spontaneous activity in a rest is pathology.

During muscle contraction, a minor or major number of motor units are activated, depending on muscle strength. Single motor unit potentials can be observed at weak muscle contraction, while at more intense or maximum contractions individual potentials overlap each other, creating a full *interference pattern*, which is an effect of summation of different motor unit potentials over time and space.

A diagnosis usually is preceded by a statistical analysis of a MUAP shape [1-3] and in particular MUAP amplitude and duration – so-called *quantitative electromyography* (*QEMG*). In order to ensure a sta-tistical analysis, reliability measurements of at least 20 different potentials are needed, and waveforms with peak-to-peak amplitude values lower than 50 μV are not taken into account. A criterion for selection of these potentials is that, in the same record, potentials with identical shape should appear at least five times.

Recently, in order to increase a diagnostic value of QEMG measurements, many tools and techniques – such as higher-order statistics [4], artificial neural networks [5–8], spectral and wavelet analyses [9–11], digital filtration [12], and modeling techniques [13] – have been used. The main advantage of the spectral analysis presented in the paper is a lack of necessity for precise determination of MUAP beginning and end as well as other parameters defined in the time domain except the amplitude.

2. NORMAL AND PATHOLOGICAL ELECTROMYOGRAMS

Temporal parameters of normal motor unit action potential were taken from literature (standard) [14], and our own results are presented in Table 1. Parameter definitions are shown in Fig. 1. Correct values of MUAP amplitudes vary from hundreds of microvolts up to a few millivolts while durations – between several and a dozen or so milliseconds. A number of phases in normal conditions is less than 4. However, it is accepted a quantity of 3–15% of polyphase potentials in which number of phases exceeds 4.

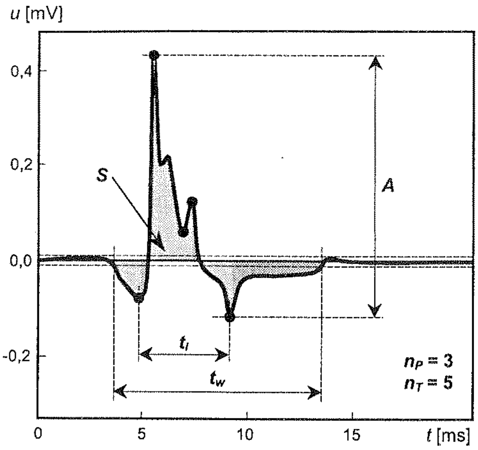

Fig. 1. A picture for parameters of motor unit action potential during weak muscular contraction.

- The potential ***amplitude A*** is defined as a peak-to-peak value.
- The MUAP ***duration*** t_w is measured from the first course deflection from a baseline to the point in which the final course phase reaches the baseline again with a determined tolerance for the amplitude (in per-centages or absolute tolerance, usually 20 μV).
- The ***spike duration*** t_i is the time between the firs and last negative peaks of the MUP.
- The ***thickness*** t_e (area/amplitude ratio) is a duration of a rectangular pulse with identical area and ampli-tude as the examined course.
- The ***area S*** is defined as an area under course module within the duration.
- The ***number of phases*** n_P is defined as number of potential deflections from the baseline.
- ***Turns*** are defined as points of potential direction changes, i.e. course extremes, while ***number of turns*** n_T (points) is determined from a number of successive turns for which difference value exceeds specified threshold value, usually 50 μV or 100 μV – to exclude peaks generated by disturbances.

Table 1

MUAP Temporal Parameters (Mean Values ± Standard Deviations) of Deltoid Muscle

Source	Amplitude A [μV]	Duration t_w [ms]	Spike duration t_i [ms]	Thickness t_e [ms]	Area S [μV·ms]	Number of Phases
Standard [14]	550±110	10.4±1.3	4.18±0.75	1.56±0.22	858±210*	2.98± 0.28
Authors' results	518±80	10.7±0.8	4.62±0.55	1.50±0.21	734±117	3.26±0.23

* Standard deviations of area were estimated on the assumption that amplitude and thickness are independent:

$$\sigma_S = \sqrt{\left(\frac{\partial S}{\partial A}\sigma_A\right)^2 + \left(\frac{\partial S}{\partial t_e}\sigma_{t_e}\right)^2} = \sqrt{(t_e\sigma_A)^2 + (A\sigma_{t_e})^2}$$

During analysis of the results, one should have in mind that in the ±σ interval around the mean value can be found in only 68% cases, while the ±2σ interval includes 95.4% cases, i.e., almost the entire population. The main diagnostic problem that quite often appears in temporal analysis consists of a partial overlapping of ±2σ intervals in normal and pathological cases.

In the author's *MUAP Analyzer* program mean value μ_x is determined in a classic way, while standard deviation σ_x is calculated using a formula limiting round-off error [15]:

$$\sigma_x = \sqrt{\frac{1}{N-1}\left[\sum_{i=1}^{N} x_i^2 - \frac{1}{N}\left(\sum_{i=1}^{N} x_i\right)^2\right]} = \sqrt{\frac{1}{N-1}\left(\sum_{i=1}^{N} x_i^2 - N\mu_x^2\right)} \qquad (1)$$

A procedure using dependence (1) is computationally more effective than procedures directly based on standard deviation definition and more precise. In that case, according to definition formula, the two large but close values should be subtracted which generates big round-off error.

Extension of a mean duration, increase of an amplitude and polyphase potentials number, enlargemenet of motor unit area, and weakening of an interference pattern indicate neuropathic changes. On the other hand shortening of a mean duration, decrease of area and amplitude, and enlargement of polyphasing is observed in muscles diseases. In a process of reinnervation after nerve damage polyphase potentials with low amplitude and short duration can appear first. In neuropathic changes a weakening of interference pattern occurs, as well as decrease of turns number and a ratio of voltage between successive turns to mean amplitude are observed. However, in processes with myopathic changes turns number is increased and a ratio of voltage between successive turns to mean amplitude is enlarged.

Summarizing, a neuropathic pattern is characterized by:

- EMG activity at rest;
- Elongated duration and high MUAP amplitudes;
- Increased polyphasing;
- Weakened interference pattern.

A myopathic pattern is characterized by:

- Short duration and low MUAP amplitude;
- Increased polyphasing;
- Enriched interference pattern – so-called *pathological interference*.

3. CHARACTERISTIC FOR SIGNAL HANDLING SYSTEM

The *Viking IV D* system developed by *Nicolet BioMedical Inc.* was applied for EMG signal handling. The basic technical parameters of *Viking IV D* system are as follows:

- Programmable gain: from 200 000 V/V to 20 V/V regulated in 13 steps according to 4-2-1 rule (sensi-tivity: from 1 μV/div up to 10 mV/div regulated in 13 steps according to 1-2-5 rule);

- Input impedance: > 1 GΩ;
- Common mode rejection ratio: > 100 dB;
- Input noise voltage in 2 Hz – 10 kHz band: < 0.7 μV;
- A/D converter resolution: 12 bit;
- Conversion time of A/D converter: 1 μs;
- Full rated conversion range of A/D converter: ±1 V;
- Total analog error for A/D converter is less than the *Least Significant Bit* (< 1 LSB);
- Resampling frequency (post decimation): 20 kHz;
- Series length: 2000 samples (100 ms).

Usually during registration of motor unit potentials, depending on diagnosed case, sensitivities from 50 μV/div do 1 mV/div are applied which gives real amplitude resolution at the level of:

$$LSB = \frac{U_{FS}}{2^n} = \frac{U_{FS}}{2^{12}} \Rightarrow \begin{cases} LSB_{\min} = \dfrac{0,5\text{mV}}{4096} = 0.12\mu\text{V} \\ LSB_{\max} = \dfrac{10\text{mV}}{4096} = 2.44\mu\text{V} \end{cases} \tag{2}$$

where U_{FS} is the full rated conversion range (including initial gain), while n is the number of bits of an output word of A/D converter.

In the *Viking IV D* system real sampling frequency is 40 kHz. For display and storage sampling is decimated to 20 kHz. The decimation routine is a "smart decimation" to maintain the peaks, troughs and morphology of the waveform. As an anti-aliasing hardware filter a second-order Butterworth low-pass filter is applied.

A frequency characteristic of the measurement system including anti-aliasing filtration and initial digital processing is shown in Fig. 2;

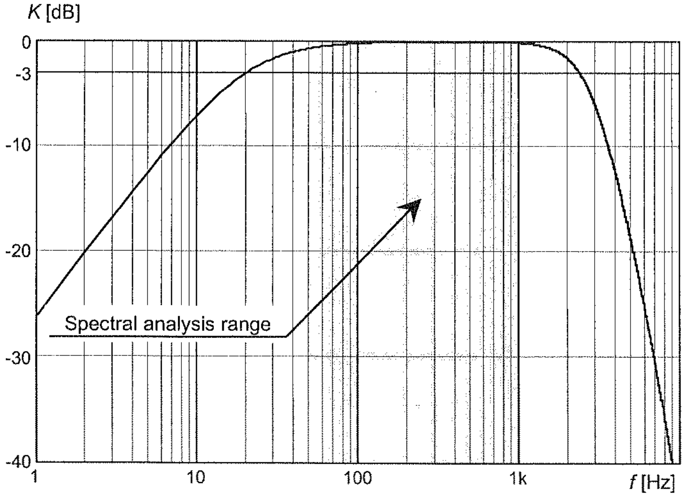

Fig. 2. Frequency characteristic of the measurement system

Bec
samples)
popular
of the cl
the frequ
because
Four

A di
product c
$\delta(t)$ train

Final

Since
that unifo
frequency

Beca
equals sa
Assu
for sampl
be found:

4. FOURIER SPECTRAL ANALYSIS

Because of relatively small vectors of temporal samples (from about 200 to 400 samples) and variable – in the preliminary stage of research – length of these sequences, popular algorithms for *fast Fourier transform* (*FFT*) have been abandoned in support of the classic definition, which enables one to obtain arbitrary transform granularity in the frequency domain. For discussed cases, this appeared to be a very valuable feature because of a narrow interval of the spectrum range being tested.

Fourier transform of a continuous signal $u_C(t)$ is defined by the dependence:

$$U_C(f) = \int_{-\infty}^{\infty} u_C(t) e^{-j2\pi f t} \mathrm{d}t \tag{3}$$

A discrete signal received as a result of a uniform sampling can be written as a product of original analog signal $u_C(t)$ and sampling function $\sigma(t)$ being a Dirac pulse $\delta(t)$ train:

$$\begin{aligned} u(t) = u_C(t)\,\sigma(t) &= \sum_{n=-\infty}^{\infty} u_C(t)\,\delta(t - nT_S) = \\ &= \sum_{n=-\infty}^{\infty} u_C(nT_S)\,\delta(t - nT_S) \end{aligned} \tag{4}$$

Finally, the Fourier transform of the analyzed discrete signal takes a form:

$$\begin{aligned} U(f) &= \int_{-\infty}^{\infty} \sum_{n=-\infty}^{\infty} u_C(nT_S)\,\delta(t - nT_S) \mathrm{e}^{-j2\pi f nT_S} \mathrm{d}t = \\ &= \sum_{n=-\infty}^{\infty} u_C(nT_S)\,\mathrm{e}^{-j2\pi f nT_S} = \sum_{n=-\infty}^{\infty} u(nT_S)\,\mathrm{e}^{-j2\pi f nT_S} \end{aligned} \tag{5}$$

Since in the exponent the t quantity is replaced by the nT_S product one can state that uniformly sampled signal spectrum is periodic with a period equal to sampling frequency $f_S = 1/T_S = 20$ kHz, because:

$$\mathrm{e}^{-j2\pi f nT_S} = \mathrm{e}^{-j(2\pi f nT_S + 2\pi k n)} = \mathrm{e}^{-j2\pi n T_S (f + k f_S)} \tag{6}$$

Because of this, a maximum frequency for which spectral analysis is reasonable equals sampling frequency.

Assuming that the transform will be calculated α times more for frequencies than for samples in the time domain that create a signal, a so-called *analysis frequency* can be found:

$$m\Delta f = m\frac{f_S}{\alpha N} \tag{7}$$

where m is the serial number of a bin in the frequency domain, i.e., output sample index of the transform, while N is the total sample number of the input series. Index n varies from zero to $N-1$ while index m varies from zero to $\alpha N-1$.

Dependence (7) includes a certain modification of classic dependence in which parameter α is not present, i.e. $\alpha = 1$. Implementation of a value $\alpha > 1$ enables arbitrary concentration of the transform to be made without necessity of zeroes padding, which in turn is necessary for fast Fourier transform algorithms. Moreover – contrary to FFT algorithms – the presented approach gives a possibility for observation of arbitrary band sector via free selection of the m index, i.e., the band of interest is determined as: $m_{\min}\Delta f \div m_{\max}\Delta f$.

Substituting successive frequencies of the analysis, we digitize a transform obtaining:

$$U(m\Delta f) = \sum_{n=-\infty}^{\infty} u(nT_S)\,\mathrm{e}^{-\mathrm{j}2\pi m\frac{f_S}{\alpha N}nT_S} = \sum_{n=-\infty}^{\infty} u(nT_S)\,\mathrm{e}^{-\mathrm{j}2\pi\frac{mn}{\alpha N}} \tag{8}$$

Neglecting – as evident – spacings in frequency and time (Δf and T_S), taking into consideration that a number of elements of temporal series is known in advance, and reducing summation to particular limits a final form of a *discrete Fourier transform* (*DFT*) for the $u(n)$ series can be found:

$$U(m) = \sum_{n=0}^{N-1} u(n)\,\mathrm{e}^{-\mathrm{j}2\pi\frac{mn}{\alpha N}} = \sum_{n=0}^{N-1} u(n)\,\mathrm{e}^{-\mathrm{j}2\pi mn\frac{\Delta f}{f_S}} \tag{9}$$

Using symmetry theorem which for our case is described by:

$$U(m) = U^{*}(\alpha N - m) \tag{10}$$

it is easy to notice that only first $m_N = \alpha N/2$ terms of frequency series is independent. It is sufficient to calcu-late components up to Nyquist frequency:

$$f_N = m_N\Delta f = \frac{\alpha N}{2}\cdot\frac{f_S}{\alpha N} = \frac{f_S}{2} = \frac{20\text{kHz}}{2} = 10\text{kHz} \tag{11}$$

A comment should be made because transform amplitudes that are N-fold summated reach values much higher than expected. In particular, when a real signal including harmonic component with an amplitude A_{sig} and such frequency f_{sig}, that a range of N input samples includes an integer number of this signal periods, is transformed, then amplitude of a bin corresponding to frequency f_{sig} is equal:

$$U(i) = A_{sig}\frac{N}{2},\ i = \frac{f_{sig}}{\Delta f} \tag{12}$$

If in a signal being transformed a constant component of A_{DC} value is present, a bin with zero frequency appears in a spectrum. Its amplitude can be expressed as:

$$U(0) = A_{DC}N \tag{13}$$

Consequently, from dependencies (12) and (13), a modified definition for DFT can be derived:

$$\begin{cases} U'(0) = \dfrac{1}{N}U(0) \\ U'(m) = \dfrac{2}{N}U(m), \quad \text{for} \quad m = 1, ..., \alpha N - 1 \end{cases} \tag{14}$$

As a result, DFT bin amplitudes correspond to amplitudes of adequate component sinusoids and zero bin amplitude equal to constant component for transformed waveform.

5. EXPERIMENTAL PROTOCOL

The EMG signal from an examined motor unit, during a weak contraction, measured by the use of concentric needle of 0.45 mm diameter produced by *Spes Medica s.r.l.*, was amplified by a low noise measurement amplifier with a controllable gain and then – after anti-aliasing filtration – undergoes analog-to-digital conversion (all using the standard *Viking IV D* system).

A diagnosed spectrum of a motor unit potential $U(m\Delta f)$ is determined using concentrated DFT on the base of a section of a signal with constant duration. Because – in view of particular way of measurement triggering – the conventional *trigger point* is situated in the *Viking IV D* system at 40 ms ($n_{tp} = 800$) and usually MUAP durations do not significantly exceed 15 ms, the authors decided to carry out spectral analysis of the 20 ms temporal section (401 samples) placed between $n_{\min} = 600$ i $n_{\max} = 1000$ (30 ms–50 ms). Since an observation of many various MUAP waveforms shows that important diagnostic information is placed in the 50 Hz–1 kHz band, then final dependence implemented in diagnostic program takes the form:

$$\begin{gathered} U'(m\Delta f)_{[\mathrm{dB}\mu\mathrm{V}]} = 20\log\left|\frac{2\cdot 10^6}{n_{\max}-n_{\min}+1}\sum_{n=n_{\min}}^{n_{\max}} u(n)\,\mathrm{e}^{-\mathrm{j}2\pi mn\frac{\Delta f}{fs}}\right| \\ \text{for} \quad m_{\min} \leqslant m \leqslant m_{\max} \\ \text{and} \quad m_{\min} = \frac{50\mathrm{Hz}}{\Delta f}, \quad m_{\max} = \frac{1\mathrm{kHz}}{\Delta f} \end{gathered} \tag{15}$$

The authors decided to apply the logarithmic function because of its larger discrimination abilities than a linear function. A transform is calculated with a granularity of $\Delta f = 10$ Hz. An upper limit for a range in which a spectrum is calculated, $f_{\max} = 1$ kHz, was taken experimentally from the fact that, for higher frequencies, spectrum level approaches noise and interference level. A lower limit, $f_{\min} = 50$ Hz, results from accepted observation time (20 ms). The time range equal 20 ms, and the frequency range from 50 Hz to 1 kHz should be treated as parameters of the suggested standard.

An average amplitude spectrum that gives essential diagnostic information is defined as an arithmetic mean for spectra of individual MUAPs $U'_k\ (m\Delta f)$:

$$U_{av}\,(m\Delta f) = \frac{1}{K}\sum_{k=1}^{K} U'_k\,(m\Delta f) \tag{16}$$

A discriminant δ, which makes classification of a diagnosed case into normal case group or to myopathic or neuropathic ones possible, can be determined as a mean level of an average spectrum according to the following dependence:

$$\delta = \frac{1}{m_{\max} - m_{\min} + 1}\sum_{m=m_{\min}}^{m_{\max}} U_{av}\,(m\Delta f) \tag{17}$$

6. RESULTS

In the preliminary stage of research, the tests have been carried out on a group consisting of 16 persons including 7 women and 9 men – between the ages of 16 and 78 years. In this group, 6 persons were classified by neurologist as healthy, myopathy was found among 5 persons, while neuropathy was found in 5 members. For each case there were 20 or more MUAP waveforms originating from a deltoid muscle.

In Figs. 3–6 averaged amplitude spectra of motor units action potentials and their mean values δ are presented for all above mentioned cases.

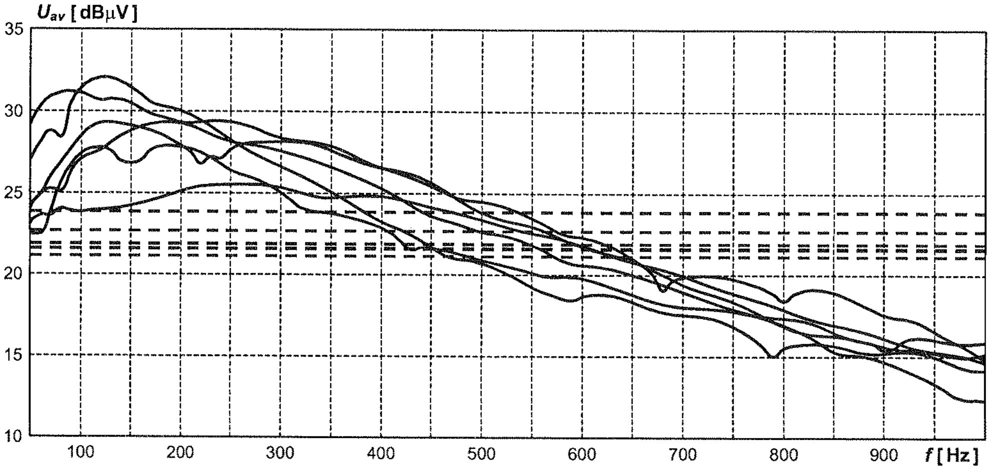

Fig. 3. Averaged amplitude spectra for MUAP signals from healthy deltoid muscles (dashed lines represent the values of δ)

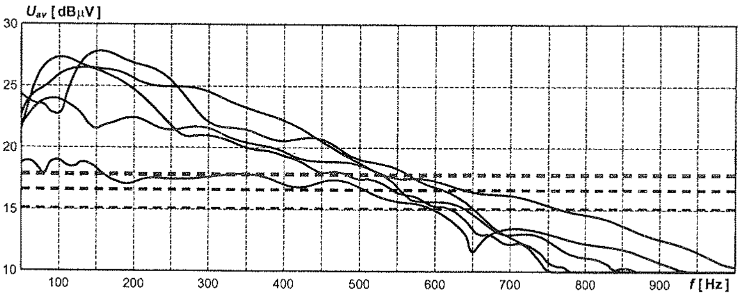

Fig. 4. Averaged amplitude spectra for MUAP signals from myopathic deltoid muscles (dashed lines represent the values of δ)

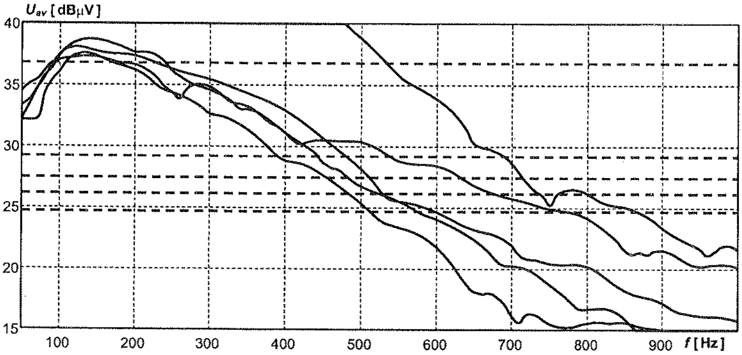

Fig. 5. Averaged amplitude spectra for MUAP signals from neuropathic deltoid muscles (dashed lines represent the values of δ)

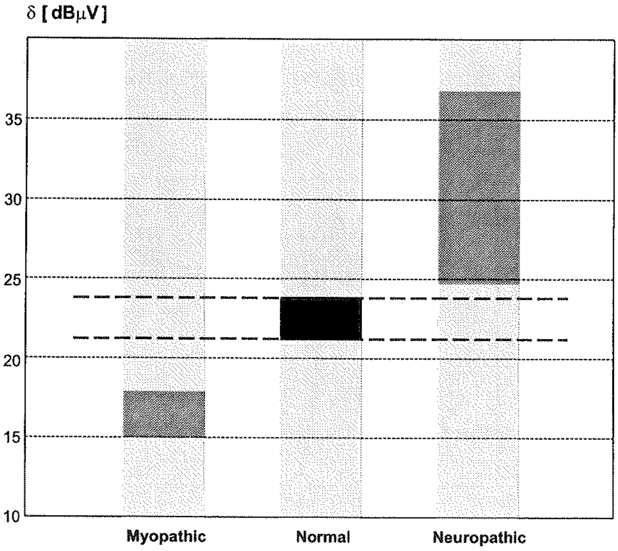

Fig. 6. A set of discriminant δ for all discussed cases

In the second stage of research, the tests have been carried out on a group consisting of 100 persons – including 53 women and 47 men – between the ages of 14 and 78 years. In this group, 70 persons – with a mean age of 37 – were classified by neurologist as healthy, myopathy was found among 10 persons, while neuropathy was found in 20 members. For each case, like previously, there were 20 or more MUAP wave-forms originating from a deltoid muscle. As a result of spectrum analyses, we get the histogram of discriminant δ shown in Fig. 7. This histogram represents a Gaussian distribution, which has been positively verified by chi-squared test with significance level at 0.01. It authorizes us to prepare the standard for a healthy deltoid muscle. From data obtained in the healthy group, we estimate **21.79 dBμV** and **1.13 dBμV** as a mean value and standard deviation of discriminant δ, respectively.

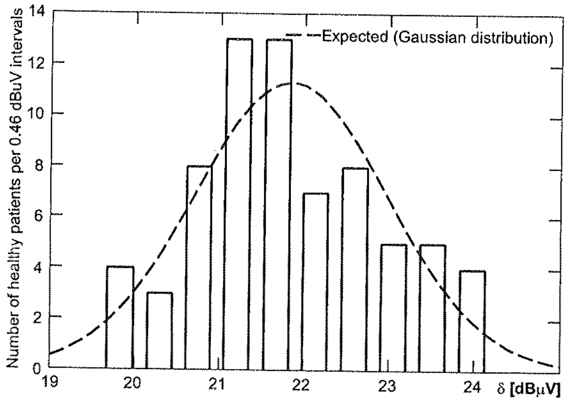

Fig. 7. Histogram of discriminant δ for healthy deltoid muscles

Calculated probability density functions together with disease cases are shown in Fig. 8.

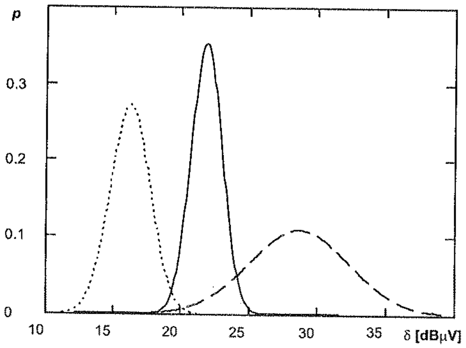

Fig. 8. Probability density functions p of discriminant δ for healthy (solid line), myopathic (dot line), and neuropathic (dashed line) deltoid muscles

For comparison, probability density functions of amplitude and duration for our normal, myopathic and neuropathic cases are shown in Fig. 9 and 10, respectively.

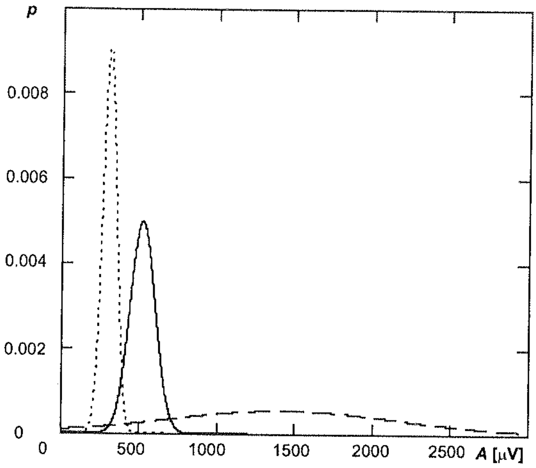

Fig. 9. Probability density functions p of amplitude A for healthy (solid line), myopathic (dot line), and neuropathic (dashed line) deltoid muscles

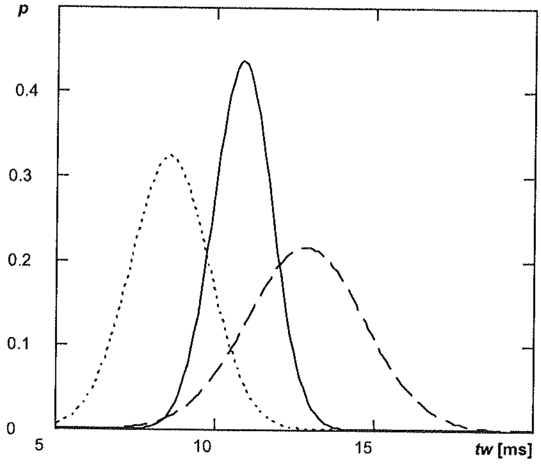

Fig. 10. Probability density functions p of duration t_w for healthy (solid line), myopathic (dot line), and neuropathic (dashed line) deltoid muscles

7. DISCUSSION

The aim of this research was formation of a precise and objective discriminant to distinguish among normal, myopathic, and neuropathic cases. The results presented in Fig. 8, 9, and 10 show that suggested discriminant δ and amplitude of temporal waveform are suitable for discrimination. In order to estimate a quality of both features we applied a proper quality factor. The quality factor defined by the equation:

$$\begin{cases} \gamma_{Mio} = \dfrac{\left|\delta_{Normal(mean)} - \delta_{Mio(mean)}\right|}{2\sigma_{Normal} + 2\sigma_{Mio}} \\ \gamma_{Neuro} = \dfrac{\left|\delta_{Normal(mean)} - \delta_{Neuro(mean)}\right|}{2\sigma_{Normal} + 2\sigma_{Neuro}} \end{cases} \tag{18}$$

for myopathic cases is 1.087 and for neuropathic cases is 0.714. The quality factor (18) applied to amplitude is 0.882 for myopathic cases and 0.547 for neuropathic cases. Regarding other MUAP temporal parameters, their discrimination possibilities are distinctly lower, for example, in case of duration, the quality factor is only 0.533 and 0.362, respectively.

Discriminant δ shows 27% superiority on average; furthermore, its possibilities can be greater. Choice of proper frequency band – different for myopathic and neuropathic cases – will make further increase of the quality factor possible. The presented results allow for a statement that spectral approach can significantly simplify a diagnosis process and make a diagnosis based on QEMG analysis more precise. The aim of next studies is a definition of standards which could allow a unique classification of myopathic, neuropathic and normal cases for a large group of muscles based on a more numerous population. Currently, the authors are working on implementation of suggested procedures into diagnostic software that could be compatible with the *Viking IV D* system.

8. ACKNOWLEDGEMENT

The authors wish to thank Mr Michael Christie from *VIASYS Healthcare Inc.* for his courtesy and help in working out the plug-in to the *Viking IV D* system database and explanations of technical details of this system.

9. REFERENCES

1. E. Zalewska, I. Hausmanowa-Petrusewicz: *Evaluation of MUAP shape irregularity – a new concept of quantification*, IEEE TBME, vol. 42(6), 1995, pp. 616-620.
2. E. Stalberg, S. D. Nandedkar, D. B. Sanders, B. Falck: *Quantitative motor unit potential analysis*, J. Clinical Neurophysiology, vol. 13(5), 1996, pp. 401-422.

---

3. E. Z
classi
pp. 13
4. S. S
statist
vol. 5
5. C. I.
positic
6. C. S.
Diagn
7. C. I.
tion o
8. N. F.
Syster
9. C. S.
Medic
10. P. W
fea-tu
dicine
11. C. S.
TBME
12. I. Ro
las-
needle
13. E. Z
irregu
14. Ch. B
of mot
pp. 84
15. S. W.
Publis

3. E. Zalewska, I. Hausmanowa-Petrusewicz: *Effectiveness of motor unit potentials classification us-ing various parameters and indexes*, J. Clinical Neurophysiology, vol. 111(8), 2000, pp. 1380-1387.
4. S. Shahid, J. Walker, G. M. Lyons, C. A. Byrne, A.V. Nene: *Application of higher order statistics techniques to EMG signals to characterize the motor unit action potential*, IEEE TBME, vol. 52(7), 2005, pp. 1195-1209.
5. C. I. Christodoulou, C. S. Pattichis: *A new technique for the classification and decomposition of EMG signals*, Proc. in IEEE Int. Conf. on Neural Networks, vol. 5, 1995, pp. 2303-2308.
6. C. S. Pattichis, C. N. Schizas, L. T. Middleton: *Neural Network Models in EMG Diagnosis*, IEEE TBME, vol. 42(5), 1995, pp. 486-496.
7. C. I. Christodoulou, C. S. Pattichis: *Unsupervised pattern recognition for the classification of EMG signals*, IEEE TBME, vol. 46(2), 1999, pp. 169-178.
8. N. F. Güler, S. Koçer: *Classification of EMG signals using PCA and FFT*, Journal of Medical Systems, vol. 29 (3), 2005, pp. 241-250.
9. C. S. Pattichis, A. G. Elia: *Autoregressive and cepstral analyses of motor unit action potentials*, Medical Engineering & Physics, vol. 21, 1999, pp. 405-419.
10. P. Wellig, G. S. Moschytz, T. Läubli: *Decomposition of EMG signals using time-frequency fea-tures*, Proceedings of the 20th Annual International Conference of the IEEE Engineering in Medicine and Biology Society, vol. 20(3), 1998, pp.1497-1500.
11. C. S. Pattichis, M. S. Pattichis: *Time-scale analysis of motor unit action potentials*, IEEE TBME, vol. 46(11), 1999, pp. 1320-1329.
12. I. Rodríguez-Carreno, A. Malanda-Trigueros, L. Gila-Useros, J. Navallas-Irujo, J. Rodríguez-Falces: *Filter design for cancellation of baseline-fluctuation in needle EMG recordings*, Computer methods and programs in biomedicine, vol. 81(1), 2006, pp. 79-93.
13. E. Zalewska, I. Hausmanowa-Petrusewicz, E. Stalberg: *Modeling studies on irregular motor unit potentials*, J. Clinical Neurophysiology, vol. 115(3), 2004, pp. 543-556.
14. Ch. Bischoff, E. Stalberg, B. Falck, K. Edebol Eeg-Olofsson: *Reference values of motor unit action potentials obtained with multi-MUAP analysis*, Muscle & Nerve, vol. 17(8), 1994, pp. 842-851.
15. S. W. Smith: *The scientist and engineer's guide to digital signal processing*, California Technical Publishing, San Diego, 1999.

S

I
a new
are di
A nev

Keyw

One of
in the meta
current flo
sed by a c
necessary t
into a solic
The pu
internal an
voltage or

ELECTRONICS AND TELECOMMUNICATIONS QUARTERLY, 2007, 53, no 2, pp. 143–154

Some further description for a current flow trough an amorphous solid. A case of an imperfect contact.

BRONISŁAW ŚWISTACZ

The Wrocław University of Technology,
Institute of Electrical Engineering Fundamentals,
Wybrzeże St. Wyspiańskiego 27, 50-370 Wrocław, Poland
bronislaw.swistacz@pwr.wroc.pl

Received 2007.04.23
Authorized 2007.05.31

Including a secondary electron emission for the cathode in a double injection problem, a new mathematical model is presented. In a planar capacitor system the carrier mobilities are discontinuous. The metal-solid-metal system can act as an n-n or p-n blocking diode. A new boundary condition for the "V" type current-voltage characteristic is determined.

Keywords: space charge transport, carrier injection, solid, trapping levels

1. INTRODUCTION

One of the purposes of space charge theory is to find the electrical field distribution in the metal-solid-metal system [1–3]. Using allowed electron transition concept, the current flow between the two electrodes can be determined. This property is expressed by a current-voltage characteristic. Generally, in order to find this function, it is necessary to give the boundary conditions describing carrier injection from the metal into a solid. In this paper, that concept will be continued.

The purpose of this work is to develop a space-charge problem and to find new internal and boundary conditions corresponding to the electric field distribution of a voltage or current stabiliser.

2. THE MATHEMATICAL MODEL

In this paper, we will consider a solid in which the trapping levels will be grouped into the four permissible energy levels [4–8]. With this assumption, the so-called effective parameters such as the frequency parameters c_{21} and c_{t12} as well as the recombination parameters c_{12} and c_{t21} will be used. For the trapped electrons, the concentrations of traps in the first and second trapping level will be represented by N_{t1} and N_{t2}, respectively. Analogously, for the trapped holes, the concentrations of traps in the first and second trapping level will be equal to P_{t1} and P_{t2}, respectively. The system of atoms will be treated as an unlimited reservoir of traps, that is $P_{t1} >> p_{t1}$; $P_{t2} >> p_{t2}$; $N_{t1} >> n_{t1}$ and $N_{t2} >> n_{t2}$. The metal-solid-metal system will be represented by a planar capacitor system with the anode $x = 0$ and the cathode $x = L$. Also, L denotes the distance between the electrodes. Moreover, we will assume that the diffusion current is negligible [9, 10]. For a solid, we will assume that the polarisation effect is characterised by the dielectric constant ε. Additionally, the mobilities μ_n and μ_p of free electrons and holes (respectively) are independent of the electric field intensity E. For the $x = L$ contact, we will consider a special case of electron emission from the cathode into a solid. Here, for the bulk plane and for the metal plane, we will assume that the contact acts as a system of points placed in a vacuum. For such a contact structure, a secondary electron emission occurs [11–13]. This property will be represented by a vacuum capacitor with the contact voltage V_2 and a distance parameter denoted by $L - d$. In our considerations, for the planar capacitor system, the basic equations such as the Gauss equation; the continuity equation; the generation-recombination equations and the field integral will be used. On this basis, the space charge transport through the bulk is described by

$$\frac{\varepsilon}{q}\frac{\partial E(x,t)}{\partial x} = p(x,t) + p_{t1}(x,t) + p_{t2}(x,t) - (n(x,t) + n_{t1}(x,t) + n_{t2}(x,t)) \tag{1}$$

$$\begin{gathered}\frac{\partial}{\partial x}\left\{\left[\mu_n n(x,t) + \mu_p p(x,t) + \mu_{t1} n_{t1}(x,t) + \mu_{t2} n_{t2}(x,t)\right] E(x,t)\right\} + \frac{\partial p(x,t)}{\partial t} + \frac{\partial p_{t1}(x,t)}{\partial t} \\ + \frac{\partial p_{t2}(x,t)}{\partial t} - \frac{\partial n(x,t)}{\partial t} - \frac{\partial n_{t1}(x,t)}{\partial t} - \frac{\partial n_{t2}(x,t)}{\partial t} = 0\end{gathered} \tag{2}$$

$$\frac{\partial n(x,t)}{\partial t} = \nu_{t1} P_{t1} + \nu_{n1} n_{t1}(x,t) - c_n N_{t1} n(x,t) - C_t n(x,t) p_{t1}(x,t) + \frac{\partial}{\partial x}\left[\mu_n n(x,t) E(x,t)\right] \tag{3}$$

$$\frac{\partial p_{t1}(x,t)}{\partial t} = \nu_{t1} P_{t1} + c_{t21} P_{t1} p_{t2}(x,t) - c_{t12} P_{t2} p_{t1}(x,t) - C_t n(x,t) p_{t1}(x,t) \tag{4}$$

$$\frac{\partial p_{t2}(x,t)}{\partial t} = c_{t12} P_{t2} p_{t1}(x,t) - c_{t21} P_{t1} p_{t2}(x,t) - \nu_{t2} p_{t2}(x,t) + c_{t2} P_{t2} p(x,t) \tag{5}$$

$$\frac{\partial n_{t1}(x,t)}{\partial t} = c_{21}N_{t1}n_{t2}(x,t) - \nu_{n1}n_{t1}(x,t) - c_{12}N_{t2}n_{t1}(x,t) + c_nN_{t1}n(x,t) + \\ + \frac{\partial}{\partial x}\left[\mu_{t1}n_{t1}(x,t)E(x,t)\right] \tag{6}$$

$$\frac{\partial n_{t2}(x,t)}{\partial t} = \nu_{p2}N_{t2} + c_{12}N_{t2}n_{t1}(x,t) - c_{21}N_{t1}n_{t2}(x,t) - C_pp(x,t)n_{t2}(x,t) \\ + \frac{\partial}{\partial x}\left[\mu_{t2}n_{t2}(x,t)E(x,t)\right] \tag{7}$$

with the voltage condition for a solid

$$\int_0^d E(x,t)dx = V_1 \tag{8}$$

And also, the electron transport between the electrode and a solid is as follows

$$\varepsilon_0\frac{\partial E_0(x,t)}{\partial x} = -qn_0(x,t) \tag{9}$$

$$\frac{\partial}{\partial x}\left[n_0(x,t)\vartheta(x,t)\right] = \frac{\partial n_0(x,t)}{\partial t} \tag{10}$$

$$-2q\int_L^x E_0(x,t)dx = m\vartheta^2(x,t) - m\vartheta^2(L,t) \tag{11}$$

$$\int_d^L E_0(x,t)dx = V_2 \tag{12}$$

Here, $q = 1.602 \cdot 10^{-19}C$, $\varepsilon_0 = 8.85 \cdot 10^{-12}F/m$; E_0 is the electric field intensity in a vacuum; m is the electron mass; x is the distance from the electrode, t is the time, ϑ is the velocity of an electron, n; n_0 and p are the free hole and electron concentrations, respectively, n_{t1}; n_{t2}; p_{t1}; p_{t2} are the concentrations of the trapped holes and electrons, respectively, μ_{t1} and μ_{t2} are the mobilities of trapped electrons, ν_{p2}; ν_{n1}; ν_{t1}; ν_{t2} denote the frequency parameters, c_n; C_p; C_t; c_{t2} denote the recombination parameters. The applied voltage V between the electrodes of a planar capacitor is

$$V = V_1 + V_2 \text{ and } V = const. > 0 \tag{13}$$

With the above equations (1)–(13) we shall define the stationary state and we shall find different current-voltage characteristics.

3. THE STATIONARY STATE

Using condition $(\partial/\partial t) = 0$ in (1)–(12), the space charge transport through the planar capacitor system can be characterised by the electric field distributions $E(x)$ and $E_0(x)$. From (1)–(12) it follows that the stationary state is determined by the following equations

$$\frac{\varepsilon}{q}\frac{dE(x)}{dx} = p(x) + p_{t1}(x) + p_{t2}(x) - (n(x) + n_{t1}(x) + n_{t2}(x)) \tag{1a}$$

$$J = qE(x)\left[\mu_n n(x) + \mu_p p(x) + \mu_{t1} n_{t1}(x) + \mu_{t2} n_{t2}(x)\right]; \quad J = const. \tag{2a}$$

$$\nu_{t1}P_{t1} + \nu_{n1}n_{t1}(x) - c_n N_{t1} n(x) - C_t n(x) p_{t1}(x) + \frac{d}{dx}\left[\mu_n n(x) E(x)\right] = 0 \tag{3a}$$

$$\nu_{t1}P_{t1} + c_{t21}P_{t1}p_{t2}(x) - c_{t12}P_{t2}p_{t1}(x) - C_t n(x) p_{t1}(x) = 0 \tag{4a}$$

$$c_{t12}P_{t2}p_{t1}(x) - c_{t21}P_{t1}p_{t2}(x) - \nu_{t2}p_{t2}(x) + c_{t2}P_{t2}p(x) = 0 \tag{5a}$$

$$c_{21}N_{t1}n_{t2}(x) - \nu_{n1}n_{t1}(x) - c_{12}N_{t2}n_{t1}(x) + c_n N_{t1} n(x) + \frac{d}{dx}\left[\mu_{t1} n_{t1}(x) E(x)\right] = 0 \tag{6a}$$

$$\nu_{p2}N_{t2} + c_{12}N_{t2}n_{t1}(x) - c_{21}N_{t1}n_{t2}(x) - C_p p(x) n_{t2}(x) + \frac{d}{dx}\left[\mu_{t2} n_{t2}(x) E(x)\right] = 0 \tag{7a}$$

$$\int_0^d E(x)dx = V_1 \tag{8a}$$

$$\varepsilon_0 \frac{d\,E_0(x)}{dx} = -q n_0(x) \tag{9a}$$

$$J = q n_0(x) \vartheta(x) \tag{10a}$$

$$-2q \int_L^x E_0(x)dx = m\vartheta^2(x) - m\vartheta^2(L) \tag{11a}$$

$$\int_d^L E_0(x)dx = V_2 \tag{12a}$$

Here
be chara
order to
mechani
bulk [14
very sma
trapped
electrons

μ_n =

Under th
is of the

where

Using a r

The gene

where

and C is
can be wr

rough the
tions $E(x)$
ed by the

(1a)

(2a)

(3a)

(4a)

(5a)

$= 0$ (6a)

$= 0$ (7a)

(8a)

(9a)

(10a)

(11a)

(12a)

Here, J is the current density. The space charge transport through the system will be characterised by a current-voltage function in the form $J = J(V)$ or $V = V(J)$. In order to find these functions, we have to define the boundary conditions describing the mechanisms of carrier injection from the anode $x = 0$ and the cathode $x = L$ into the bulk [14]. In what follows, we will assume that the mean free path of the electron is very small and that the additional portion of the kinetic energy, which is given to the trapped electron by en external electric field, is too small. For the trapped holes and electrons, we additionally introduce into our analysis the following assumption

$$\mu_n = \mu_{t1} = \mu_{t2} = 0; \quad C_t = 0; \quad \tau_{t1}^{-1} = c_{t12}P_{t2} = c_{t21}P_{t1}; \quad \tau_1^{-1} = c_{21}N_{t1} = c_{12}N_{t2}$$

Under these conditions, the equation for the electric field distribution $E(x)$ in a solid is of the following form [15]

$$\frac{\varepsilon\mu_p E}{J}\frac{dE}{dx} = a_0 - a_1\frac{E}{J} - a_2\frac{E^2}{J^2} \tag{14}$$

where

$$a_0 = 1 + \frac{2c_{t2}P_{t2}}{\nu_{t2}}; \quad a_1 = \left(\frac{1}{c_nN_{t1}} + \frac{\tau_1\nu_{n1}}{c_nN_{t1}} + \tau_1 - \tau_{t1} - \frac{2}{\nu_{t2}}\right)\cdot q\mu_p\nu_{t1}P_{t1};$$
$$a_2 = \left(2 + \frac{\nu_{n1}}{c_nN_{t1}}\right)\frac{q^2\mu_p^2}{C_p}\left(\nu_{p2}N_{t2} + \nu_{t1}P_{t1}\right) \tag{15}$$

Using a new variable $z = E/J$, (14) becomes

$$\varepsilon\mu_p Jz\frac{dz}{dx} = a_0 - a_1z - a_2z^2; \quad z = E/J \tag{16}$$

The general integral of (16) is

$$|z - z_1|^A\,|z - z_2|^B = C\cdot\exp\left(-\frac{a_2x}{\varepsilon\mu_pJ}\right) \tag{17}$$

where

$$z_1 = \frac{1}{2a_2}\left(-a_1 + \left(a_1^2 + 4a_0a_2\right)^{\frac{1}{2}}\right); \quad z_2 = \frac{-1}{2a_2}\left(a_1 + \left(a_1^2 + 4a_0a_2\right)^{\frac{1}{2}}\right);$$
$$A = \frac{z_1}{z_1 - z_2}; \quad B = \frac{z_2}{z_2 - z_1} \tag{18}$$

and C is a constant of integration. The most general form of a function $V_1 = V_1(J)$ can be written as

$$V_1 = J\int_0^d z\,dx = J\int_{z(0)}^{z(d)} z\left(\frac{dx}{dz}\right)dz = \varepsilon\mu_p J^2 \int_{z(0)}^{z(d)} \frac{z^2}{a_0 - a_1 z - a_2 z^2}dz \tag{19}$$

Combining (19), we have

$$V_1 = \frac{\varepsilon\mu_p J^2}{a_2}(z(0) - z(d)) + \frac{\varepsilon\mu_p J^2}{a_2^2}\int_{z(0)}^{z(d)} \frac{a_1 z - a_0}{(z - z_1)(z - z_2)}dz \tag{20}$$

Next, combining (20) and (17), we can find another equivalent form of (20), that is

$$V_1 = \frac{\varepsilon\mu_p J}{a_2}[E(0) - E(d)] - \left(a_1 - \frac{a_0}{z_2}\right)\frac{Jd}{a_2} - \frac{\varepsilon\mu_p a_0 J^2}{z_2 a_2^2}\cdot\ln\left|\frac{E(0) - Jz_1}{E(d) - Jz_1}\right|; \quad z_2 < 0 \tag{21}$$

Now, according to (9a)–(12a), we can find the electric field distribution $E_0(x)$

$$E_0(x) = \left(\frac{6mJ^2}{q\varepsilon_0^2}(L - x) + E_0^3(L)\right)^{\frac{1}{3}} \quad \text{and} \quad E_0(\vartheta = 0) = 0 \tag{22}$$

for which the integral (12a) results in

$$V_2 = \frac{q\varepsilon_0^2}{8mJ^2}\left\{\left[E_0^3(L) + \frac{6mJ^2}{q\varepsilon_0^2}(L - d)\right]^{\frac{4}{3}} - E_0^4(L)\right\} \tag{23}$$

Thus, the current-voltage characteristic $V = V(J)$ has the following parametric form [16, 17]

$$V = V_1[J, E(0)] + V_2[J, E_0(L)] \quad \text{and} \quad J = f_0[E(0)]; \quad J = f_L[E_0(L)] \tag{24}$$

Here, the boundary functions $f_0[E(0)]$ and $f_L[E_0(0)]$ describe the mechanisms of carrier injection from the electrodes into the interior of the system. In what follows, we will consider some cases of the current flow through the system. As the first case, we will take into consideration the following internal conditions

$$E(d) = 0; \quad A = B = \frac{1}{2}; \quad z_1 = -z_2 \tag{25}$$

under of which, we get a boundary function

$$E(0) = Jz_1\sqrt{1 + \exp\left(\frac{2J_g}{J}\right)}; \quad J_g = \frac{a_2 d}{\varepsilon\mu_p} \tag{25a}$$

describing the hole injection from the anode into the bulk. In the particular case, there is

$$\text{if } \frac{J_g}{J} > 4 \text{ then } E(0) = Jz_1\exp\left(\frac{J_g}{J}\right) \text{ and } V_1 = \frac{\varepsilon\mu_p z_1}{a_2}J^2\exp\left(\frac{J_g}{J}\right) \tag{25b}$$

Next according to (23) and (24), as an example, for the linear boundary function $J = \sigma_L E_0(L)$, where σ_L is the boundary parameter, (24) is of the form

$$V = \frac{z_1 d}{J_g}J^2\exp\left(\frac{J_g}{J}\right) + \frac{q\varepsilon_0^2J^2}{8m\sigma_L^4}\left\{\left[1+\frac{6m(L-d)\sigma_L^3}{q\varepsilon_0^2J}\right]^{\frac{4}{3}}-1\right\} \tag{26}$$

Additionally, if there is $\frac{1}{4}J_g << \frac{6m(L-d)\sigma_L^3}{q\varepsilon_0^2}$ (a case of high level of electron emission from the cathode into a vacuum) then (26) is reduced to

$$V = \frac{z_1dJ^2}{J_g}\exp\left(\frac{J_g}{J}\right) + \beta J^{\frac{2}{3}} \quad \text{and} \quad \beta = \frac{3}{4}\left(\frac{6m}{q\varepsilon_0^2}\right)^{\frac{1}{3}}(L-d)^{\frac{4}{3}} \tag{26a}$$

Another case occurs for $J >> 2J_g$, that is $E(0) = Jz_1\sqrt{2}$. Here, (26) can be replaced by

$$V = \beta_2J^2 - \beta_1J \tag{27}$$

where

$$\beta_2 = \frac{z_1d}{J_g}\left(\sqrt{2}+\ln(\sqrt{2}-1)\right); \quad \beta_1 = z_1d - \frac{L-d}{\sigma_L} \tag{27a}$$

In (27), there can be $\beta_1 \geqslant 0$ (a case of a voltage source) or $\beta_1 < 0$ (a case of a current stabiliser). Now, let us consider a case of the high level of hole injection from the anode into the bulk, that is

$$E(0) << Jz_1; \quad A = B = \frac{1}{2}; \quad z_1 = -z_2 \tag{28}$$

Using a new parameter $w = \frac{E(d)}{Jz_1}$ for (21), we have

$$V_1 = \frac{\varepsilon\mu_pJ}{a_2}[E(0)-E(d)] - \left(a_1 - \frac{a_0}{z_2}\right)\frac{dJ}{a_2} - \frac{\varepsilon\mu_pa_0J^2}{z_2a_2^2}\left(w+\frac{w^2}{2}+\frac{w^3}{3}+\ldots\right)$$
$$\text{for } w<1 \text{ and } w = \sqrt{1-\exp\left(\frac{-2J_g}{J}\right)} \tag{28a}$$

Next, for $J >> 2J_g$ and $E(0) = 0$ (a case of a pn junction), limiting the power series to the third power, (28a) becomes

$$V_1 = \frac{\varepsilon\mu_p a_0 J^2}{z_1 a_2^2}\cdot\frac{w^3}{3} \quad \text{and} \quad w = \sqrt{\frac{2J_g}{J}} \tag{28ab}$$

Next, for (23), using the quadratic boundary function $J = a_L E_0^2(L)$ (here $a_L > 0$ is the boundary parameter), a function (24) takes the following form

$$V = \alpha J^{\frac{1}{2}} + \frac{q\varepsilon_0^2}{8ma_L^2}\left\{\left[1 + \frac{6ma_L^{\frac{3}{2}}J^{\frac{1}{2}}}{q\varepsilon_0^2}(L-d)\right]^{\frac{4}{3}} - 1\right\}; \quad \alpha = \frac{1}{3}\left(\frac{8a_0 d^3}{\varepsilon\mu_p}\right)^{\frac{1}{2}} \tag{29}$$

When the cathode injects an infinite amount of electrons, (29) takes the simplier form

$$V = \alpha J^{\frac{1}{2}} + \beta J^{\frac{2}{3}}; \quad \beta = \frac{3}{4}\left(\frac{6m}{q\varepsilon_0^2}\right)^{\frac{1}{3}}(L-d)^{\frac{4}{3}} \tag{29a}$$

Also, in a solid a negative space charge can be distributed when

$$E(d) >> \left|z_{1,2}J\right| \quad \text{and} \quad E(0) >> \left|z_{1,2}J\right| \quad \text{and} \quad E_0(x = L) = 0 \tag{30}$$

From (17) we get

$$E(d) = E(0)\cdot\exp(-J_g/J) \quad \text{and} \quad J_g = \frac{a_2 d}{\varepsilon\mu_p} \tag{30a}$$

Under these conditions, according to (21)–(23), a function (24) becomes

$$V = \frac{JdE(0)}{J_g}\left(1 - \exp\left(-J_g/J\right)\right) + \beta J^{\frac{2}{3}} - \gamma J; \quad \gamma = \frac{a_1 d}{a_2} \tag{31}$$

For example, when the boundary function $J = f_0[E(0)]$ is quadratic in the form $J = \alpha_0^2 E^2(0)$, the current voltage – characteristic (31) is of the following form

$$V = \frac{d}{\alpha_0 J_g}J^{\frac{3}{2}}\left(1 - \exp(-J_g/J)\right) + \beta J^{\frac{2}{3}} - \gamma J \tag{31a}$$

Here $\alpha_0 > 0$ is the boundary parameter. If $J_g/J > 4$, then (31a) can be replaced by

$$V = \frac{d}{\alpha_0 J_g}J^{\frac{3}{2}} + \beta J^{\frac{2}{3}} - \gamma J \tag{31aa}$$

Another example, when the boundary function is linear $J = \sigma_0 E(0)$, where $\sigma_0 > 0$ denotes the boundary conductivity parameter, a function (31) has the following form

$$V = \frac{d}{\sigma_0 J_g}J^2\left(1 - \exp\left(-J_g/J\right)\right) + \beta J^{\frac{2}{3}} - \gamma J \tag{31b}$$

For $J_g/J > 4$, instead of (31b), there is

$$V = \frac{d}{\sigma_0 J_g} J^2 + \beta J^{\frac{2}{3}} - \gamma J \tag{31ba}$$

Now, still, in order to find the other case of the current flow, let us return to (17)-(18). Here, we ascertain that the electric field can be uniform

$$E(x) \equiv z_1 J \ \text{ and } \ V_1 = z_1 d J \tag{32}$$

Next, referring to (23) and (24), for example, using the linear boundary function $J = \sigma_L E_0(L)$ or the quadratic boundary function $J = a_L E_0^2(L)$ for the cathode, we obtain (respectively)

$$V = z_1 d J + \frac{q\varepsilon_0^2 J^2}{8m\sigma_L^4}\left\{\left[1 + \frac{6m(L-d)\sigma_L^3}{q\varepsilon_0^2 J}\right]^{\frac{4}{3}} - 1\right\} \tag{32a}$$

or

$$V = z_1 d J + \frac{q\varepsilon_0^2}{8ma_L^2}\left\{\left[1 + \frac{6ma_L^{\frac{3}{2}} J^{\frac{1}{2}}}{q\varepsilon_0^2}(L-d)\right]^{\frac{4}{3}} - 1\right\} \tag{32b}$$

where σ_L and a_L are the boundary parameters. Generally, for (23), when the electron emission from the cathode into a vacuum is described by $1 >> \frac{6mJ^2(L-d)}{q\varepsilon_0^2 E_0^3(L)}$ (this is acceptable for the low level of electron injection), and under conditions of (32), there is

$$V = z_1 d J + (L-d) f_L^{-1}(J) \tag{32c}$$

Here $f_L^{-1}(J)$ denotes the inverse function of the boundary function $f_L[E_0(L)]$ describing the electron emission from the metal into the vacuum. For example, in the case of linear or quadratic boundary function and of the Fowler-Nordheim function, a formula (32c) exists. The inverse case occurs when the cathode injects an infinite amount of electrons $1 << \frac{6mJ^2(L-d)}{q\varepsilon_0^2 E_0^3(L)}$ (this is acceptable for the Poole or Schottky boundary function, and also, there can be $E_0(L) = 0$). Now, (32c) is replaced by a function

$$V = z_1 d J + \beta J^{\frac{2}{3}} \tag{32d}$$

and β is expressed by (26a).

4. DISCUSSION and CONCLUSIONS

In the above we have analysed the current flow between the two electrodes $x = 0$ and $x = L$ when the hole mobility $\mu_p = \mu_p(x)$ and the electron mobility $\mu_n = \mu_n(x)$ are discontinuous for $x = d$ and $0 \leqslant d \leqslant L$. With this assumption, the plane $x = d$ can be characterised by a surface charge density q_s in the form

$$q_S = \varepsilon_0 E_0(d) - \varepsilon E(d) \ \text{ and } \ q_S = q_S(J) \tag{33}$$

under of these conditions, the metal-solid-metal system can act as a p-n or an n-n junction or an Schottky barrier (32)–(32d). In the case of an n-n blocking diode, which is determined by (25), the surface charge density is equal to $q_S = \varepsilon_0 E_0(d)$. Moreover, from (26)–(27a) it follows that a function (24) has the minimum (which can be denoted by V_{th}) and there is

$$V(J = 0+) = V(J = \infty) = \infty \tag{34}$$

Thus, the function (24) defines the "V" type curve with the negative differential resistance. This property denotes that there exists a set of the applied voltage $0 < V < V_{th}$ (a case of the voltage source) for which the current density does not determine. Here, a formula (25a), which corresponds to the given internal processes of the bulk, presents a new mechanism describing carrier injection from the metal into the bulk. The existence of the threshold voltage V_{th} can explain the switching effect for a solid [6–8, 17, 18]. Using the mechanism (25a), we ascertain that the voltage $V = V(J)$ or the current $J = J(V)$ can be stabilised. Also, for an n-n blocking diode described by (30)–(31ba), the similar property is observed. In the case of a p-n junction, the voltage $V = V(J)$ is presented by (28)–(29a), the system can act as the voltage stabiliser. Moreover, the negative differential resistance is not observed.

Now, let us compare our methodology with other ones. A regional approximation method has been presented by Lampert [6]. Here, for a p-n junction (and others), using the boundary condition $E(0) = E(L) = 0$ and quasi-neutrality assumption, the electric field intensity distribution is strongly monotonic at the electrode regions as well as this function is quasi-uniform in the bulk. On this basis, Lampert showed that the current – voltage characteristic can be shaped as $J \propto V^4$ or the "S" type curve. Investigating the current flow through the metal-imperfect insulator- metal system, the similar concept has been used by Kao [10]. He showed that the system could act as Schottky barrier. Also, using a quadratic boundary function, Kao showed that the negative differential resistance could occur. Generally, quasi – neutrality assumption is not quite mathematically clear. This condition denotes that the electric field divergence is almost equal to zero. In other words, with this assumption, the total concentration of carriers is given. In our space charge problem, this function is determined by the mechanisms of carrier injection from the two electrodes into the bulk.

5. SUMMARY

In this work we have assumed that the allowed electron transitions between the lower and the higher energy levels are stimulated only by the electric – magnetic force interactions between adjacent atoms and by incident photons. In a solid, the additional trapping levels (for positive and negative charge carriers) can be caused by impurities or by pollutants [18]. On this basis we have determined some physical interpretations. As a singular case of electric conduction in a solid, we have analysed an electric field distribution corresponding to the low level of hole injection from the anode into the bulk. Under these conditions a negative space charge with the density $q_v = \varepsilon \frac{dE}{dx} < 0$ can be distributed in the bulk, while we have assumed that the holes are mobile with the mobility μ_p. In consequence, with this assumption, we have to give the boundary condition describing the mechanism of hole injection from the anode into the bulk. From (1)–(8) it follows that this particular integral of (14) is physically acceptable when an initial space charge is negative (which must be given in order to determine the transient state), that is $q_v(x,0) = \varepsilon \frac{\partial E(x,0)}{\partial x} < 0$. Practically, using an electron radiation or an implantation method, this condition can be realised. For example, in a solid, which is implanted by the O_8^{16} and N_7^{14} atoms at the $x = d$ solid/vacuum contact, the electrons can be absorbed by these impurities (or pollutants) from the $x = d$ plane. Next, such the injected electrons can be absorbed by internal phonons (rotators and oscillators). Under these conditions an initial negative space charge can be formed in the anode-solid/vacuum-cathode system. For a solid, we can show that the negative space charge is distributed when the recombination parameter C_p satisfies the following condition [15]

$$\tau_1^{-2} \ll \frac{1}{18} \nu_{p2} N_{t2} C_p \quad \text{or} \quad \tau_1^{-2} \ll \frac{1}{18} \nu_{t1} P_{t1} C_p \tag{35}$$

From (35) it follows that the free positive space charge is neutralised by the trapped electrons (which are localised in the second trapping level) when the concentration of traps N_{t2} and the recombination parameter C_p are sufficiently great (the left formula). Also, from (35) it follows that the negative space charge is induced when the hole generation in a solid is not too strong. In other words, a negative space charge in the bulk can occur when the atomic number Z_2 corresponding to the second trapping level (for the trapped electrons) is less than the atomic number Z_v corresponding to the valence level [16], that is

$$Z_2 \ll 3 \cdot Z_v; \qquad \tau_1^{-1} \simeq 0.02 \cdot \nu_{p2} \tag{35a}$$

$$Z_2 \ll 2 \cdot Z_v; \qquad \tau_1^{-1} \simeq 0.028 \cdot \nu_{p2} \tag{35b}$$

$$Z_2 \ll 1.5 \cdot Z_v; \quad \tau_1^{-1} \simeq 0.04 \cdot \nu_{p2} \tag{35c}$$

For example, if there is $Z_2 = 6; 7; 8$, then conditions (35a)–(35c) are acceptable for the material such as ZnO, CdS, GaAs, ZnS, ZnTe, Se^{79}_{34}, $BaTiO_3$, J^{127}_{58} and others. With (35a)–(35c) the negative resistance, which is expressed by (34), can occur. According to the different experiments [6–8, 17], the current-voltage characteristics, which are expressed by (24), are observed.

6. REFERENCES

1. G. Cimatti: *Existence of Weak Solutions for the Space-Charge Problem.* IMA. J. Appl. Math., vol. 44, 1990, pp. 185-195.
2. C.J. Budd, A. Friedman, B. Mcleod, A.A. Wheeler: *The Space Charge Problem.* SIAM. J. Appl. Math., vol. 50, 1990, pp. 191-198.
3. T. Bhattacharya: *A note on the space charge problem.* IMA. J. Appl. Math., vol. 48, 1992, pp. 117-124.
4. K.C. Kao: *New theory of electrical discharge and breakdown in low-mobility condensed insulators.* J. Appl. Phys., vol. 55, 1984, pp. 752-755.
5. R. Patsch: *Space-Charge Phenomena in Polyethylene at High Electric Fields.* J. Phys. D.: Appl. Phys., vol. 23, 1990, pp. 1497-1505.
6. M.A. Lampert, P. Mark: *Current injection in solids.* Academic Press, New York, 1970.
7. J. Simon, J.-J. Andre: *Molecular Semiconductors. Photoelectrical Properties and Solar Cells.* Berlin, Springer, 1985.
8. A. Ziel: *Solid state physical electronis.* New Jersey, USA, 1976.
9. R.B. Schilling, H. Schachter: *Neglecting Diffusion in Space-Charge-Limited Currents.* J. Appl. Phys., vol. 38, 1967, pp. 841-844.
10. K.C. Kao: *Double injection in solids with non-ohmic contacts: II. Solids with defects.* J. Phys. D.: Appl. Phys., vol. 17, 1984, pp. 1449-1467.
11. O. Hachenberg, W. Brauer: *Secondary Electron Emission from Solids, Advances in Electronics and Electron Physics*, New York, Academic Press, vol. 11, 1959, pp. 413-499.
12. B. Mazurek, J.D. Cross: *Fast cathode processes in vacuum discharge development.* J. Appl. Phys., vol. 63, 1988, pp. 4899-4904.
13. P.A. Budd, B. Javidi, J.W. Robinson: *Secondary Electron Emission from a Charged Dielectric.* IEEE Trans. Electr. Insul. vol. EI-20, 1985, pp. 485-491.
14. H. Matsuura, H. Okushi: *Schottky barrier junctions of hydrogenated amorphous silicon-germanium alloys.* J. Appl. Phys., vol. 62, 1987, pp. 2871-2879.
15. B. Świstacz: *A current flow problem for amorphous solids. A case of weak and mean electric fields.* Arch. Electr. Eng. vol. LI II, No. 2, Warsaw, 2004, pp. 121-130.
16. B. Świstacz: *Bipolar space-charge problem for semiconductors and insulators.* J. Phys.: Condens. Matter, vol. 7, 1995, pp. 2563-2585.
17. B. Świstacz: *Carrier generation and the switching phenomenon. Further theoretical description.* J. Phys.: Condens. Matter, vol. 7, 1995, pp. 10037-10048.
18. A.G. Milnes: *Deep Impurities in Semiconductors.* John Wiley and Sons, New York – London – Sydney – Toronto, 1973.

for the
s. With
cording
ich are

l. Math.,

n. SIAM.

48, 1992,

sulators.

D.: Appl.

70.
lar Cells.

Currents.

Phys. D.:

in Elec-

J. Appl.

rged Die-

licon-ger-

n electric

Condens.

scription.

London –

ELECTRONICS AND TELECOMMUNICATIONS QUARTERLY, 2007, 53, no 2, pp. 155–176

The increase of DFT and DCT computation rate and accuracy with the use of parallel operations

WŁODZIMIERZ POGRIBNY, MARCIN DRECHNY

University of Technology and Life Sciences
Faculty of Telecommunications and Electrical Engineering
Al. Prof. S. Kaliskiego 7, 85-796 Bydgoszcz
pohry@utp.edu.pl, mardrech@utp.edu.pl

Received 2006.12.28
Authorized 2007.04.24

DFT (Discrete Fourier Transform) and its derivative DCT (Discrete Cosine Transform) are the transforms most often used in DSP (Digital Signal Processing), especially in data communications for signal compression [1, 2, 3, 4]. DFT and DCT algorithms have been modified and their rate and accuracy optimized for many years [3, 4]. Most of them are calculated in multibit PCM (Pulse Code Modulation) format. The differential DPCM (Differential Pulse Code Modulation) format, used in this work can be an alternative for PCM format applied in DFT and DCT. It ensures higher accuracy of computation with code word length shorter than PCM code word. When we modify DPCM format (Section 3) in such a way that the quantization steps are set of the numbers with a base 2 and exponent belonging to a natural numbers set, the multiplication operation rate, as one of the most often used operation in DSP, increases. It is possible because multiplication operations can be replaced with fast shift bit logical operations. The parallel combination of some MDPCM (Modified Differential Pulse Code Modulations) codes creates SDPCM (Synthesized Differential Pulse Code Modulation) code (Section 3), which has high computational accuracy, equal to the DPCM accuracy, however it does not require multiplications.

In most cases, parallel computations lead to their rate increase in comparison to computation rate of sequentially operations. These calculations, apart from using appropriate and accurate algorithms require applying the systems which enable the effective work of the parallel methods. Thus, for this purpose the programmable FPGA devices (Fields Programmable Gates Array) have been the most commonly used recently. Their main advantages are high speed of operations, the possibility of programming every computational structure and their low price.

In this work, apart from fast parallel DFT and DCT algorithms, we presented the structures of processing DFT and DCT systems (specialized processors) working in parallel way. The processing systems presented in Section 5 allow fast and accurate calculations without time-consuming multiplications. With reference to the article [5] presenting fast

differential DCT algorithms, in this work the authors proposed another way of increasing the rate and accuracy of DCT computations, which consists in the modifications of a part of DCT spectrum (Section 4).

The aim of this paper is working out the methods for increasing of DFT and DCT computation rate and accuracy with the use of parallel operations and differential MDPCM and SDPCM formats.

Keywords: DFT, DCT, DPCM, parallel computations

1. INTRODUCTION

DFT and DCT algorithms have been improved for many years because their classical versions did not come up to continuously increased expectations of fast signal processing. Therefore, many fast algorithms have been worked out, mainly in multibit PCM format, often destined for specific tasks. To such algorithms belong: algorithms with the assumed number of input values, algorithms minimizing number of multiplications and algorithms doing calculations only for integer input values [3, 4]. Such solutions considerably increase the calculation rate but do not always make possible calculations to be done in real time. The working out of FFT (Fast Fourier Transform) algorithms enabled fast and accurate calculations in real time but their restriction is that they require time-consuming multiplication operations.

DFT and DCT algorithms are usually based on computations done in multibit PCM format. The usage of this format ensures high accuracy of calculations and wide processing band. However, multibit PCM often makes signal processing in the real time impossible, mainly because of the time-consuming multiplications. As it was presented in work [5] on the DCT example, there is the possibility of the effective use of the differential modulations to signal processing which ensure the same accuracy as PCM format but for a shorter code word length.

The differential code that guarantees high computational accuracy is DPCM code. However, during signal processing in DPCM format, similarly as with the application of PCM format, multiplication operations are used. One of the methods to eliminate entirely the multiplication operations is to use the proper code based only on the logical shift operations. The modified DPCM format (MDPCM) ensures such operation in which quantization steps belong to the set of the base 2 and exponent belonging to a natural numbers set [5]. In this way, multiplying multibit number in PCM format in fixed point code by quantization step in MDPCM format, we can make fast logical shift operations by a number of bits determined by the module of MDPCM step. The similar way to decrease the number of multiplications operations was used in digital filtering in work [6].

As the studies in [5] show, the usage of MDPCM in DCT is advisable only for 3 and 4-bit code word length, because for DCT of a signal of longer code word length we obtain higher SNR (Signal to Noise Ratio) value using DPCM format. In order to create DPCM code, which ensures high computational accuracy and fast calculations,

---

we must
format g
The
priate p
program
compete
structure
The
– highe
– more
their
– calcu
The
zeroing
the incre
The
DCT co
MDPCM

2.

The

where, X

of sampl

means th
code. Th
presented

$X(m) =$

Algo
the same

we must synthesize it by joining some MDPCM code. Synthetic DPCM (SDPCM) format guarantee fast parallel calculations.

The usage of SDPCM format for fast DFT or DCT requires working out appropriate parallel structures of specialized processors which can be realized on FPGA programmable fields. In practice, in the field of digital signal processing these devices compete with specialized DSP processors [7, 8]. The differential specialized processors structures presented in work [5] are not appropriate for this purpose.

The main advantages of DCT in comparison to DFT are [3, 9]:

- higher accuracy, taking into consideration the influence of boundary effects,
- more concentrated components at the low frequencies of the spectrum what ensures their further compression,
- calculations done only in real numbers domain.

The spectrum properties of DCT make possible its modification which consists in zeroing parts of its components. It results in the decreased number of operations and the increase of SNR value.

The aim of this article is working out the methods of increasing of DFT and DCT computation rate and accuracy with the use of parallel operations and differential MDPCM and SDPCM formats.

2. FAST DFT AND DCT ALGORITHMS IN SDPCM-PCM FORMAT

2.1. CLASSICAL DFT AND DCT ALGORITHMS

The basic DFT algorithm in PCM-PCM format is presented as follows:

$$X(m) = \sum_{n=0}^{N-1} x(n) \cdot W_N^{-nm} \tag{1}$$

where, $X(m) - m^{th}$ DFT spectrum term, $x(n) - n^{th}$ sample in PCM format, N – number of samples of input signal, $W_N = \exp\left(j\frac{2\pi}{N}\right)$ and $\forall m, n = \overline{0, N-1}$. PCM-PCM format means that sample $x(n)$ and factor W_N^{-nm} on which the operations are done, are in PCM code. The derivative of DFT is DCT. Its classical algorithm in PCM-PCM format is presented below:

$$X(m) = k_m \sum_{n=0}^{N-1} x(n) \cdot \cos\left(\frac{\pi \cdot m \cdot (2 \cdot n + 1)}{2 \cdot N}\right), \quad k_m = \begin{cases} \dfrac{\sqrt{2}}{N}, & \text{for} \quad m = 0 \\ \dfrac{2}{N}, & \text{for} \quad m = \overline{1,\ N-1} \end{cases} \tag{2}$$

Algorithms (1) and (2) require nearly N^2 multibit multiplication operations and the same number of summations. The number of operations presented above does not include the calculation of W_N^{-nm} and $\cos\left(\frac{\pi \cdot m \cdot (2 \cdot n + 1)}{2 \cdot N}\right)$ factor and, in case of DCT, multiplication of the sum by factor k_m. In order to use the differential modulations, proper converting of the (1) and (2) algorithm is required the similar way as it was done in [5].

2.2. DFT AND DCT ALGORITHMS IN DM-PCM FORMATS

In order to use the DM steps in DFT and DCT algorithms we must properly convert the expressions (1) and (2). Firstly, we define the increasing differences which are depicted as:

$$\nabla x_n = x_n - x_{n-1} \tag{3}$$

where ∇x_n – increasing difference in ∇PCM format, x_n – n^{th} sample of the signal in PCM format, x_{n-1} – $(n-1)^{th}$ sample of the signal in PCM format.

The reconstruction of the signal by the precondition $\forall x_n = 0$ when $n < 0$ is as follows:

$$x_n = \sum_{i=0}^{n} \nabla x_i = x_0 + \sum_{i=0}^{n} \nabla x_i \tag{4}$$

By substituting the expression (4) to the expression (1) we obtain the DFT transform in differential formats in the following form:

$$X(m) = \sum_{n=0}^{N-1} \sum_{r=0}^{n} \nabla x_r W_N^{-nm} \tag{5}$$

When we write out the sums we obtain the following expression:

$$X(m) = \sum_{n=0}^{N-1} \sum_{r=0}^{n} \nabla x_r W_N^{-nm} = \underbrace{\nabla x_0 W_N^{-0m}}_{n=0} + \underbrace{\nabla x_0 W_N^{-1m} + \nabla x_1 W_N^{-1m}}_{n=1} +$$

$$+ \underbrace{\nabla x_0 W_N^{-2m} + \nabla x_1 W_N^{-2m} + \nabla x_2 W_N^{-2m}}_{n=2} + \ldots +$$

$$+ \underbrace{\nabla x_0 W_N^{-(N-1)m} + \nabla x_1 W_N^{-(N-1)m} + \ldots + \nabla x_{N-1} W_N^{-(N-1)m}}_{n=N-1} =$$

Next, we group the products with the increases having the same numbers:

$$= \underbrace{\nabla x_0 W_N^{-0m} + \nabla x_0 W_N^{-1m} + \ldots + \nabla x_0 W_N^{-(N-1)m}}_{r=0} +$$

$$+ \underbrace{\nabla x_1 W_N^{--1m} + \nabla x_1 W_N^{-2m} + \ldots + \nabla x_1 W_N^{-(N-1)m}}_{r=1} +$$

$$+ \underbrace{\nabla x_2 W_N^{-2m} + \nabla x_2 W_N^{-3m} + \ldots + \nabla x_2 W_N^{-(N-1)m}}_{r=2} + \ldots + \underbrace{\nabla x_{N-1} W_N^{-(N-1)m}}_{r=N-1}$$

By creating proper sums we obtain the following fast differential DFT algorithm:

$$X(m) = \sum_{r=0}^{N-1} \nabla x_r \sum_{n=r}^{N-1} W_N^{-nm} \tag{6}$$

In the same way we create the fast differential DCT algorithm by substituting the expression (4) to the expression (2) which is as follows:

$$X(m) = k_m \sum_{r=0}^{N-1} \nabla x_r \sum_{n=r}^{N-1} \cos\left(\frac{\pi m(2n+1)}{2N}\right) \tag{7}$$

Replacing the differences for the DM steps ($s_r^{(x)}$) we obtain DFT and DCT algorithm in DM-PCM format. The fast DFT algorithm in DM-PCM format is presented as:

$$X(m) = \sum_{r=0}^{N-1} s_r^{(x)} \sum_{n=r}^{N-1} W_N^{-nm} \tag{8}$$

In the same way we obtain fast DCT algorithm in DM-PCM format:

$$X(m) = k_m \sum_{r=0}^{N-1} s_r^{(x)} \sum_{n=r}^{N-1} \cos\left(\frac{\pi m(2n+1)}{2N}\right) \tag{9}$$

The sums of W_N^{-nm} and $\cos\left(\frac{\pi m(2n+1)}{2N}\right)$ terms can be earlier calculated and stored in the memory. In this case the number of multiplications and additions is equal N^2.

2.3. DFT AND DCT ALGORITHMS IN SDPCM-PCM FORMATS

The application of SDPCM format in algorithms allows using quantization steps which belong to a full series of integer numbers. This is the main difference in comparison to algorithms using MDPCM format in which the quantization steps are from the set of the numbers with a base 2 and exponent belonging to a natural numbers set.

SDPCM code is a parallel connection of a few MDPCM codes. As a result of such connection the DFT and DCT processing is realized on individual MDPCM codes. The components obtained after DFT or DCT for every MDPCM code are added.

The DFT algorithm in SDPCM-PCM format is presented below:

$$X(m)=\sum_{b=1}^{e}\sum_{r=0}^{N-1} s_{r,b}^{(MDPCM\#b)}\sum_{n=r}^{N-1} W_N^{-nm} \tag{10}$$

were: $s_{r,b}^{(MDPCM\#b)}$ – r^{th} quantization step of MDPCM#b code, e – number of MDPCM codes used to create the SDPCM code.

The fast DCT algorithm using SDPCM format is presented as follows:

$$X(m)=k_m\sum_{b=1}^{e}\sum_{r=0}^{N-1} s_{r,b}^{(MDPCM\#b)}\sum_{n=r}^{N-1}\cos\left(\frac{\pi m(2n+1)}{2N}\right) \tag{11}$$

In expressions (10) and (11) all multiplication operations were eliminated (what was ensured by MDPCM code) by replacing them with fast shift operations, on the assumption that the sums $\sum W_N^{-nm}$ in case of DFT and $\sum \cos\left(\frac{\pi m(2n+1)}{2N}\right)$ in case of DCT had been previously calculated and stored in the memory of the specialized processor. It is noticeable that shift and addition operations are done in a parallel manner and algorithms (10) and (11) can be considered as independent DFT or DCT in MDPCM-PCM format. Therefore, the number of shift and addition operations done in each parallel algorithm for MDPCM code equals N^2.

3. SYNTHETIC DPCM

3.1. CREATION OF THE SDPCM CODE

In this work, in order to increase the calculations rate of DSP algorithms the authors used the MDPCM format in which all quantization steps were chosen from the set of numbers $\{0, \pm 1, \pm 2, \pm 4, \pm 8, \ldots\}$. The numbers have base 2 and the exponents belong to the natural numbers set. Such steps make possible to eliminate time-consuming multiplications and replace them with logical shift operations. Similar conception of reducing number of multiplications was used for digital filtering presented in work [6].

The derivative of MDPCM format is SDPCM format which consist in formation of every DPCM step by summing the corresponding MDPCM steps. Each MDPCM code [5] has quantization steps only from the set of numbers which are the power of number two. Thus, this format does not contain all quantization steps of uniform distribution. Therefore, by joining some of MDPCM encoders it is possible to synthesize DPCM code with all quantization steps. This allows to replace the multiplication operations with fast shift operations. An example of creating some SDPCM codes from MDPCM codes is shown in table 1.

Table 1

Formation of 5-bit Synthesized DPCM code from three MDPCM codes (only positive values)

Synthesized DPCM steps	MDPCM #1 3-bit code word	MDPCM #2 3-bit code word	MDPCM #3 2-bit code word
0	0	0	0
1	1	0	0
2	2	0	0
3	−1	4	0
4	0	4	0
5	1	4	0
6	2	4	0
7	−1	8	0
8	0	8	0
9	1	8	0
10	2	8	0
11	1	2	8
12	4	8	0
13	1	4	8
14	2	4	8
15	−1	8	8

As depicted in table 1, to create 5-bit DPCM code there were used two 3-bit MDPCM codes and one 2-bit MDPCM code. The quantization steps of MDPCM coders were chosen from the sets of the steps: MDPCM#1 $\{0, \pm1, \pm2, \pm4\}$, MDPCM#2 $\{0, \pm1, \pm2, \pm4\}$, MDPCM#3 $\{0, \pm8\}$. For example, to create step 9 of DPCM we must sum up three steps of MDPCM coders: MDPCM#1 = 1, MDPCM#2 = 8 and MDPCM#3 = 0 what equals 1+8+0=9 in DPCM code.

The method presented above is universal because it allows to form each DPCM code from both different number of the MDPCM codes and different sets of steps of the corresponding coders.

If we want to create synthetic DPCM also for 6, 7 or 8-bit DPCM we can apply MDPCM codes from table 2.

Table 2 shows only some of many ways of creating SDPCM format for 5, 6, 7 and 8-bits.

Table 2

Sets of quantization steps for 5, 6, 7 and 8-bit SDPCM

Number of bits of SDPCM coder	MDPCM #1	MDPCM #2	MDPCM #3	MDPCM #4
	Sets of quantization steps (Number of bits MDPCM coder)			
5	0,±1,±2,±4 (3)	0,1,±8 (2)	0,1,±16 (2)	X
6	0,±1,±2,±4 (3)	0,±1, ±8,±16 (3)	0,1,±32 (2)	X
7	0,±1,±2,±4 (3)	0,±1, ±8,±16 (3)	0,±32,±64 (3)	0,1 (1)
8	0,±1,±2,±4 (3)	0,±1, ±8,±16 (3)	0, ±1, ±16,±32 (3)	0, ±1, ±64,±128 (3)

3.2. OPERATIONS FOR PCM, MDPCM AND SDPCM CODES

In order to describe the chosen operations for MDPCM and SDPCM codes we need to present the notation of PCM, MDPCM and SDPCM codes that are used in this work. In order to simplify the description of the quantization steps we used a sign-module positional code:

– for a sample in PCM format:

$$h_k = \operatorname{sgn} h_k \varepsilon_{h_k} |h_k| \tag{12}$$

– for a step in differential format:

$$s_n^{(x)} = \operatorname{sgn} s_n^{(x)} \varepsilon_{s_n^{(x)}} \left| s_n^{(x)} \right| \tag{13}$$

where: h_k – k^{th} sample in PCM format, sgnh_k – its sign, $|h_k|$ – its module, $s_n^{(x)}$ – n^{th} step of quantization of MDPCM or SDPCM coder, $\operatorname{sgn} s_n^{(x)}$ – its sign, $\left|s_n^{(x)}\right|$ – its module, ε – multiplier of every sample or quantization steps which has nonzero values. In this work only the simplest variant is considered, that is, when $\varepsilon_{h_k} = \varepsilon_{s_n^{(x)}} = \varepsilon$.

For the simplicity of mathematical operations the signs of samples or steps belong to the set of $\{-1, 1\}$. In binary notation the signs correspond to the set $\{0, 1\}$. The transformation from positional code to binary notation for PCM is following:

$$B_{s,h_k} = \frac{\operatorname{sgn} h_k + 1}{2}, \forall B \in \{0, 1\} \tag{14}$$

The same transformation can be done for MDPCM and SDPCM quantization steps.

3.2.1. Operations for PCM codes

The PCM code is always used for DFT or DCT of signals in differential formats. When the signal is presented in differential format the W_N^{-nm} or $\cos\left(\frac{\pi\cdot m\cdot(2\cdot n+1)}{2\cdot N}\right)$ factors (expression 8, 9, 10 and 11) are presented in multibit PCM code.

The module of PCM sample h_k in fixed-point notation illustrated in expression (5) is defined as:

$$|h_k| = \sum_{a=-q}^{n} B_{h_k,a}\cdot 2^a \tag{15}$$

where $B_{h_k,a}$ – the sign bit of sample h_k. The module of the same sample h_k in binary notation is:

$$|h_k| = B_{h_k,n}\ldots B_{h_k,-q} \tag{16}$$

One of the most often used operations in DSP is multiplication operation. Therefore, below in expression (17) we present the multiplication of sample h_k and i_j in PCM codes:

$$h_k\cdot i_j = \varepsilon^2\cdot\left(2\left(\overline{B_{s,h_k}\oplus B_{s,i_j}}\right)-1\right)\sum_{a=-q}^{n} B_{h_k,a}\cdot 2^a\cdot\sum_{p=-g}^{m} B_{i_j,p}\cdot 2^p \tag{17}$$

where h_k – k^{th} sample of signal h in PCM format, i_j – j^{th} sample of signal i in PCM format, B_{s,h_k} – the sign bit of the sample h_k, B_{s,i_j} – the sign bit of the sample i_j. The multiplication operation presented in expression (17) consists of $m+n+g+q+4$ addition microoperations and $m+n+g+q+7$ multiplication microoperations.

3.2.2. Operations for MDPCM code

The MDPCM step in its positional code is represented in the following way:

$$s_r^{(MDPCM)} = \varepsilon\cdot\operatorname{sgn} s_r^{(MDPCM)}\cdot\left|s_r^{(MDPCM)}\right| = \varepsilon\cdot\operatorname{sgn} s_r^{(MDPCM)}\cdot 2^{c_r} \tag{18}$$

where: $s_r^{(MDPCM)}$ – r^{th} step of MDPCM coder, c_r – natural number. The exponent c_r determines the position of logical "1". The important thing is to set the way of coder work, that is, if it works as a midtread or widrise quantizer. That means the quantization steps are chosen from the set of $\{\pm1,\pm2,\pm4,\ldots\}$ for the midrise coder and from the set of $\{0,\pm1,\pm2,\pm4,\ldots\}$ for the midtread coder. The MDPCM quantization step in the binary code notation is shown below:

$$B^{(x)}_{s,s_r^{(MDPCM)}}\ \overbrace{B_{s_r^{(MDPCM)},c_r}\underbrace{0\ldots0}_{c_r-1}}^{c_r} \tag{19}$$

where $B^{(x)}_{s,s_r^{(MDPCM)}}$ means the bit of the sign of the quantization step, $B_{s_r^{(MDPCM)},c_r}$ means the bit of logical “1”.
The multiplication operation of MDPCM step and PCM sample in fixed-point number representation is

$$s_r^{(MDPCM)} \cdot h_k = \varepsilon^2 \left(2\left(\overline{B^{(x)}_{s,s_r^{(MDPCM)}} \oplus B_{s,h_k}}\right) - 1\right) \cdot \sum_{a=-q}^{n} B_{h_k,a} 2^{a+c_r} \tag{20}$$

The operation presented above is a shift operation done on the PCM sample h_k. The number of the shifts in (20) is defined by c_r factor. Expression (20) requires $q+n+3$ adding microoperations, $q+n+5$ multiplication microoperations and c_r-1 shift microoperations.

The product (20) in bit notation is presented as follows:

$$h_l = s_r^{(MDPCM)} \cdot h_k \Rightarrow \overbrace{B_{s,h_l} B_{h_{k,n}} \ldots B_{h_k,-q} \underbrace{0\ldots0}_{c_r-1}}^{q+n+c_r+1} \tag{21}$$

As we can see, the shift operation inserts c_r-1 zero values in the less significant bits. Multiplying two MDPCM steps leads to the shift operations analogically like in (20) is shown below:

$$s_{r,1}^{(MDPCM\#1)} \cdot s_{r,2}^{(MDPCM\#2)} = \varepsilon^2 \left(2\left(\overline{B^{(x)}_{s,s_{r,1}^{(MDPCM\#1)}} \oplus B^{(x)}_{s,s_{r,2}^{(MDPCM\#2)}}}\right) - 1\right) \cdot 2^{c_{r,1}+c_{r,2}} \tag{22}$$

The number of the shifts in (22) is defined by $c_{r,2}$ factor. Expression (22) requires 2 adding microoperations, 5 multiplication microoperations and $c_{r,2}-1$ shift microoperations.

As we can see, the number of microoperations during multiplying MDPCM step by PCM sample or by MDPCM step is considerably smaller than the number of microoperations done while multiplying two PCM samples.

3.2.3. Operations for SDPCM code

The SDPCM code is created from a few MDPCM codes. The example of creation of SDPCM step from some MDPCMs is presented below:

$$s_r^{(SDPCM)} = \varepsilon \cdot \sum_{b=1}^{e} s_{r,b}^{(MDPCM\#b)} = \varepsilon \cdot \sum_{b=1}^{e} \operatorname{sgn} s_{r,b}^{(MDPCM\#b)} \cdot 2^{c_{r,b}} \tag{23}$$

where: $s_r^{(SDPCM)}$ – r^{th} step of the SDPCM coder and e – number of MDPCM codes used to create SDPCM code.

The multiplication operation between the SDPCM step and the PCM sample in fixed-point number representation is:

$$s_r^{(SDPCM)} \cdot h_k = \varepsilon^2 \sum_{b=1}^{e} \left(\left(2 \left(\overline{B^{(x)}_{s,s_r^{(MDPCM\#b)},c_r,b} \oplus B_{s,h_k}} \right) - 1 \right) \cdot \sum_{a=-q}^{n} B_{h_k,a} 2^{a+c_{r,b}} \right) \tag{24}$$

The realisation of the presented above product requires $e \cdot (q + n + 3)$ adding microoperations, $e \cdot (q + n + 3) + 2$ multiplication microoperations and $(c_{r,b} - 1) \cdot e$ shift microoperations.

The multiplication operation between two SDPCM steps $s_{r_1}^{(MDPCM\#b)}$ and $s_{r_2}^{(MDPCM\#d)}$ is following:

$$s_{r_1}^{(MDPCM\#b)} \cdot s_{r_2}^{(MDPCM\#d)} = \varepsilon^2 \left(\sum_{b=1}^{e} \sum_{d=1}^{f} \left(2 \left(\overline{B^{(x)}_{s,s_{r_1}^{(MDPCM\#b)}} \oplus B^{(y)}_{s,s_{r_2}^{(MDPCM\#d)}}} \right) - 1 \right) \cdot \left(2^{c_{r_1,b}+c_{r_2,d}} \right) \right) \tag{25}$$

The expression (25) requires $e \cdot f \cdot 2$ adding microoperations, $(e \cdot f \cdot 2) + 2$ multiplication microoperations and $(c_{r,b} - 1) \cdot e \cdot f$ shift microoperations.

Similarly to the multiplication operation that uses the MDPCM format, the multiplication of two SDPCM steps or the SDPCM steps by PCM sample is realized by the shift operations. However, in case of applying SDPCM format, the shift operations are done simultaneously and parallel, what considerably decreases the calculation time.

4. DCT SPECTRUM MODIFICATIONS

4.1. THE METHODS OF INCREASING THE ACCURACY OF SIGNALS RECONSTRUCTION AFTER THEIR SPECTRUM COMPRESSION

The spectra of signals processed in differential formats presented in work [5] are characterized by the great irregularity and also by the fact that their main power is concentrated at the beginning of frequency axis. The high frequency components have a decidedly lower power and therefore some of them can be modified.

4.1.1. The spectrum modification beginning from the upper signal frequency

Using the DCT property which makes the signal reconstruction possible with its little quality loss after the deformation of its spectrum upper components [7, 10], the modification based on zeroing (that is replacing the DCT components with the zero value) parts of the DCT components was done. The zeroing is begun from the component that determines the upper frequency of the signal f_u. The end of the zeroing range is the last DCT component of the processed signal spectrum. In this way the frequency terms with frequency higher than 3400 Hz have been eliminated. This method of spectrum modification is the simplest and it is described as follows:

$$\forall X(m) = 0, \quad \text{if } m > u \tag{26}$$

where: u – the index of upper frequency, in this example defined as 3400 Hz.

Such modification enables to increase the calculation rate, because if we assume the zeroing of some part of the frequency components, we can omit that part during DCT components calculations.

4.1.2. *Spectrum modification with the application of the levels of the spectrum components*

Spectrum modification which begins from the upper frequency is a simple method and leads to a smaller number of calculations to be done (what causes that the calculation rate increases) and the increase of the SNR. The similar effect can be obtained by modifying the signal spectrum, in which the first zeroed component does not have to be at the signal upper frequency. In some cases better SNR can be obtained by spectrum modification beginning from frequency lower than upper signal frequency.

The idea of that method is based on looking for values in the DCT component series which modules are below the assumed limit value δ. In this method we begin the spectrum modification from the assumption of the number of the following frequency terms and the assumption of the level value of upper component. Beginning from the first DCT component, we look for the first group of the earlier assumed number of the following components with module levels lower than δ. The first zeroed element is the last element from the found group of components whereas the last zeroed element is the last DCT spectrum component of the processed signal.

Another variant of this method is the application of the fuzzy extreme analysis [11] to zeroing DCT components. That algorithm consists in finding the set of the extremes of the processed signal comparing to the assumed fuzzy limit. Next, on the basis of the analysis of the fuzzy extreme set $\left\{X_r^{(e)}\right\}$, the beginning of the zeroing is being looked for, which is the last extreme in this set or the beginning is the extreme with the longest distance to the previous extreme, assuming that this distance is longer than the earlier assumed boundary value. This method is presented by the expression:

$$\forall X^{(e)}, X_{\exists}\delta\left(\left(\bigwedge_{r=i+1}^{i+n}(|X_r| \leqslant \delta)\right) \mapsto \left(\forall X_k = 0, \quad k = \overline{i+n, \quad N}\right)\right) \tag{27}$$

where: $\left\{X_r^{(e)}\right\}$ – are extremes of DCT spectrum, δ – assumed limit value, k – number of frequency component, r – number of extreme.

In the above methods the δ value is assumed, which should be carefully chosen, because too high δ value can degrade the quality of the processed signal.

4.2. EXAMPLES OF THE ACCURACY INCREASE OF THE DIFFERENTIAL DCT ALGORITHMS ON THE BASIS OF DCT SPECTRUM MODIFICATION

The worked out and presented in Section 4 methods of DCT spectrum modifications using partial zeroing its components were examined with the application of tests signals such as pink noise and voice. These test signals were described in work [5] and have also the same parameters. The SNR value was calculated in the same way as it is shown in work [5].

4.2.1. An example of the modification of the pink noise spectrum

The diagram form, presented below illustrates the results of the studies of partial spectrum modification of pink noise with the use of the first method, in which the zeroing begins from the DCT component defined as signal upper frequency. In this case upper frequency is 3400 Hz. The figures 1 and 2 show the comparison of the SNR values computed during DCT processing of pink noise for three signals representations, four the code words length and two sampling rates with the use of zeroing and without it.

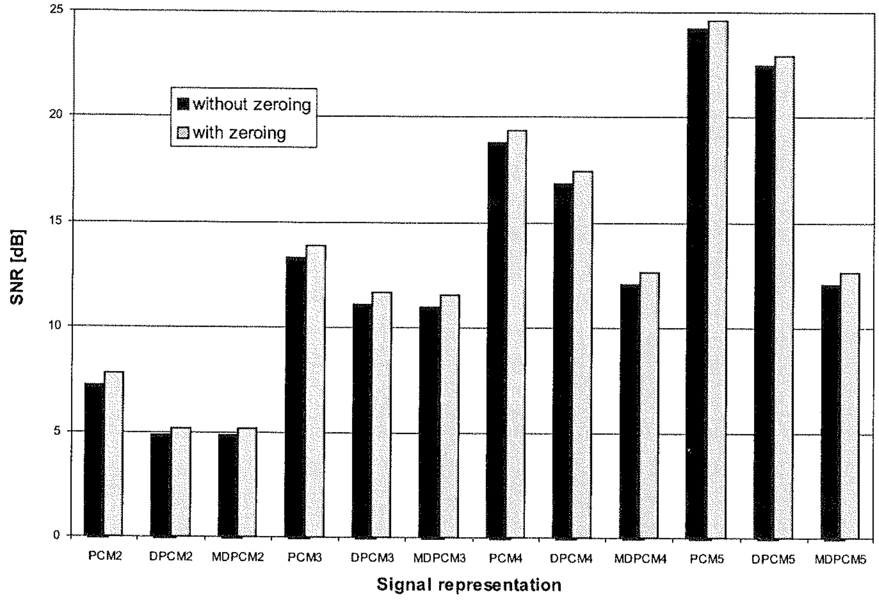

Fig. 1. The comparison of the pink noise SNRs processed in PCM and differential formats with zeroing of a part of DCT components and without zeroing them for sampling rate 8000 Hz

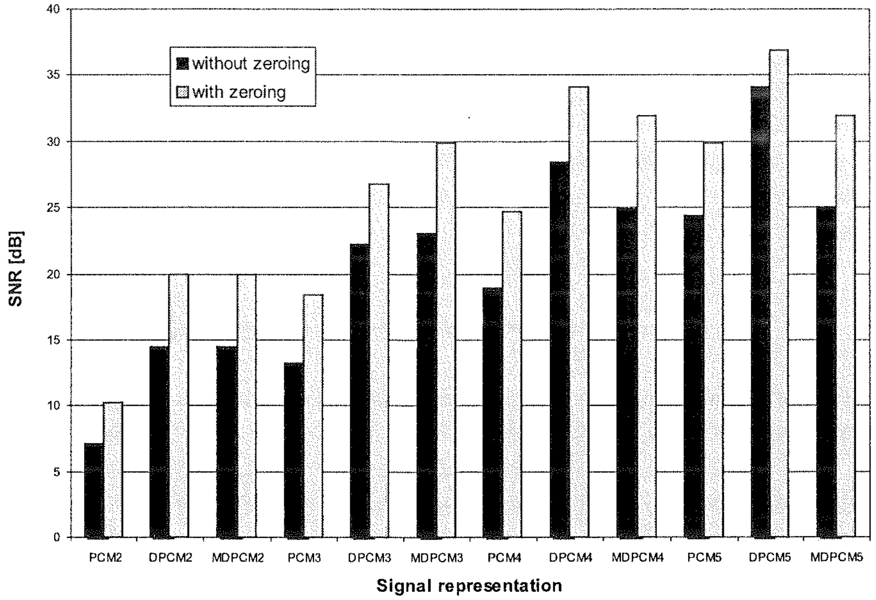

Fig. 2. The comparison of the pink noise SNRs processed in PCM and differential formats with zeroing of a part of DCT components and without zeroing for sampling rate 44100 Hz

If we compare the above figures we can see that in each studied case the SNR increased when the zeroing operation began from the signal upper frequency of pink noises. The increase of SNR during zeroing of a part of DCT components in comparison to SNR obtained without zeroing, is higher when the sampling rate is higher. The highest increase of SNR we obtained for 5-bit MDPCM format with sampling rate 44100 Hz and it amounts to 6.96 dB.

4.2.2. Example of the speech signal spectrum modification

Similarly to the studied pink noise, we also used the zeroing of a part of speech signals DCT components beginning from signal upper frequency 3400 Hz. The figures 3 and 4 present the comparison of average SNR values obtained during DCT signals coded in PCM and differential formats for four code word lengths and two sampling frequencies with the use of zeroing and without it.

Having studied the differential DCT with zeroing the part of speech spectrum with the use of the first method we can notice, that the conclusions are similar to those which were formulated during zeroing of the pink noise spectrum. The SNR values, obtained for each studied speech signal, increased (also their average SNR values as shown in figure 3 and 4) after the modification of a part of their DCT components.

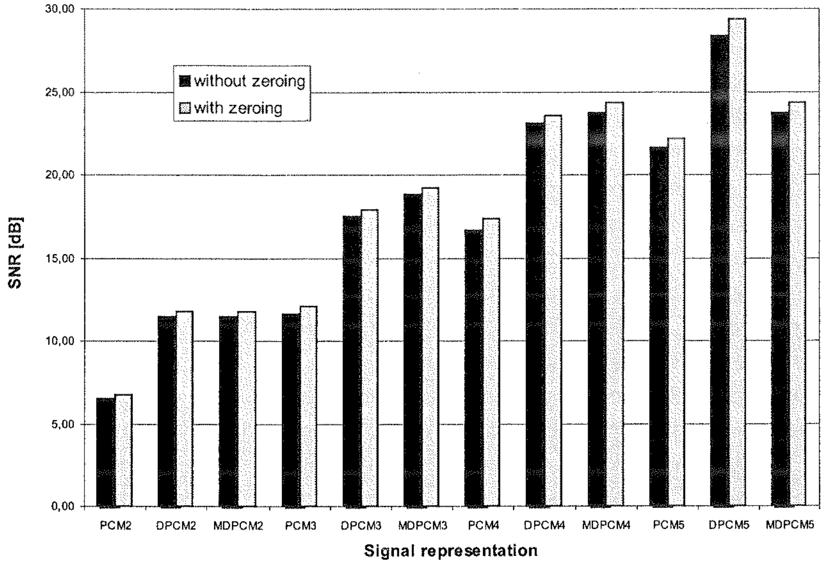

Fig. 3. The comparison of the mean SNR of speech signals processed in PCM and differential formats with zeroing of a part of DCT components and without zeroing for sampling frequency 8000 Hz

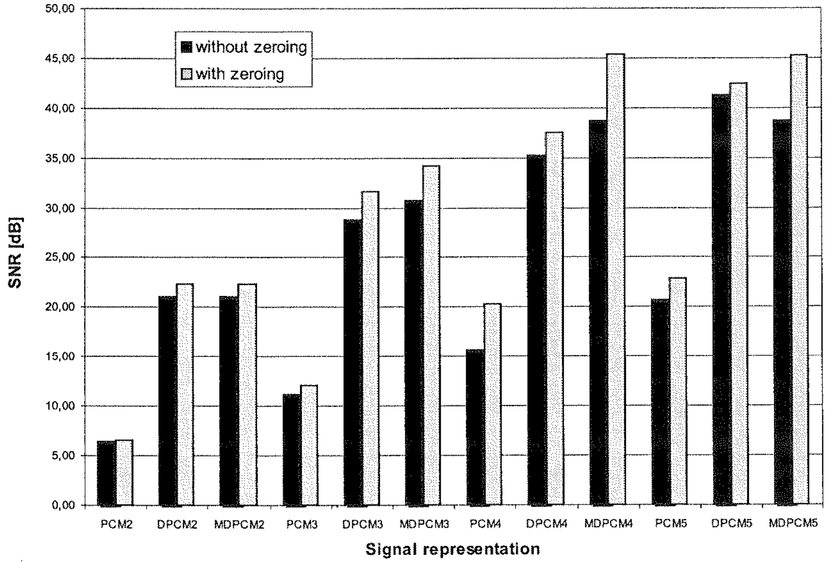

Fig. 4. The comparison of the mean SNR of speech signals processed in PCM and differential formats with zeroing of a part of DCT components and without zeroing for sampling frequency 44100 Hz

Higher increase of the averaged SNR values is connected with higher sampling rate. The highest increase of the SNR value is obtained for MDPCM format and it amounts to 6.98 dB.

The results of the studies presented above confirm that using the first zeroing method for pink noise and speech in no case decreases the SNR values. The most important is that the biggest increase of SNR value was obtained for DPCM and MDPCM formats which are the basic formats used in this work for fast differential algorithms of DFT and DCT. This method is simply to implement in programs and systems and can be used in real time computations. If we also take into consideration that the part of DCT components during DCT or IDCT (Inverse Discrete Cosine Transform) computations can be omitted, the accuracy and calculation rate of algorithms presented in work [5] can considerably be increased.

The second method of zeroing requires setting the limit values and the length of the analyzed series which makes it more complex in comparison to the first method of zeroing. The main problem that occurs during simulations with the use of the second method is a choice of boundary values and length of the analyzed series of DCT components. In case of their wrong choice, the SNR value considerably worsens. The results of DCT the spectrum modification of the Polish words "*dom*" and "*szary*" with the application of two methods of zeroing for sampling rate 8000 Hz are presented in table 3.

Table 3

The comparison of SNR values of the Polish words "dom" and "szary" processed in differential formats with two methods of zeroing of part of DCT components

Signal representation	Word "dom"			Word "szary"		
	Without zeroing	Zeroing Ist method	Zeroing IInd method	Without zeroing	Zeroing Ist method	Zeroing IInd method
	SNR [dB]			SNR [dB]		
DPCM2	10.88	11.19	12.97	7.69	7.88	7.88
MDPCM2	10.88	11.19	12.97	7.69	7.88	7.88
DPCM3	18.01	18.45	19.82	12.57	12.84	12.84
MDPCM3	19.41	19.93	21.24	13.69	13.98	13.96
DPCM4	24.31	24.86	24.84	17.45	17.82	17.82
MDPCM4	23.33	23.78	26.42	17.94	18.64	18.57
DPCM5	30.04	30.60	30.56	22.36	22.70	22.81
MDPCM5	23.30	23.77	23.86	18.08	18.80	18.69

Table 3 shows that in the comparison to the first method, the second method of zeroing with optimally chosen parameters of zeroing (values of the limits and length of the studied series of components) can increase the SNR value. The results presented in table 3 confirm that for word "*dom*" the use of the second method of zeroing, caused the increase of the SNR value at about 2.64 dB comparing with the first method of zeroing. In case of the word "*szary*", the application of the second method of zeroing did not cause a significant change of SNR value and is comparable to the values obtained with the first method of zeroing. The most important thing is that, similarly to the first method, the second method in none studied case deteriorated the quality of the signal in comparison to the DCT results done without zeroing. The second method of zeroing can also be applied to computation in the real time.

5. STRUCTURES OF THE SPECIALIZED DFT AND DCT PROCESSORS WITH PARALLEL OPERATIONS

The structure of specialized processor presented in work [5] makes fast DCT processing possible. However, the restriction of this method, as it was mentioned earlier, is that the quantization steps belonging to the set of the numbers with a base 2 and exponent belonging to a natural numbers set, do not assure the continuity in that series. As the studies of the speech signals show [5], the usage of the MDPCM code word is limited only to 4-bits because in case of more than 4-bits, DPCM format is more accurate. The structure of the specialized DCT processor built on the basis of SDPCM code and algorithm (4) which the general form is presented in figure 5 does not possess such restriction.

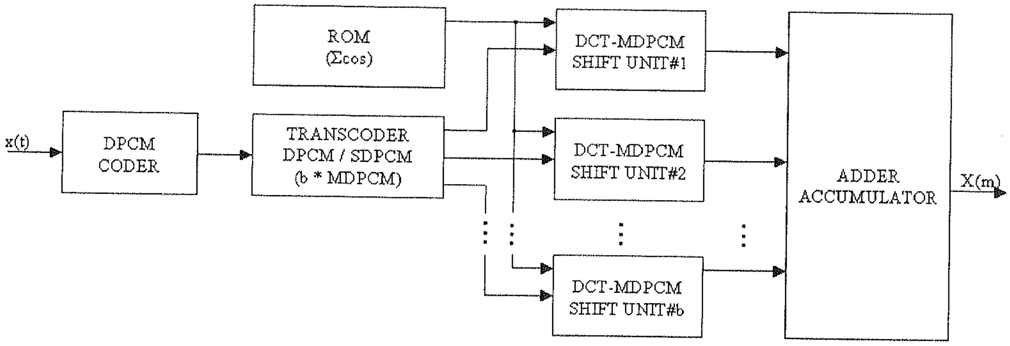

Fig. 5. General block diagram of specialized DCT processor with the use of SDPCM format

This structure has *b* shift units, which numbers depend on the numbers of MDPCM codes used for creating the SDPCM steps. Every SHIFT UNIT has the same structure as in the work [5]. All shift units are connected with ROM (Read Only Memory) from which the previously calculated sums of cosine terms in multibit PCM format are transmitted. The SHIFT UNITS are also connected with TRANSCODER which defines the MDPCM steps. After synchronous parallel shift, all intermediate results are added and accumulated (ADDER-ACCUMULATOR).

The structure of specialized DFT processor in SDPCM format is the expansion of the structure from the figure 5 by the shift units which define the imaginary components part of the transform. The figure 6 presents the general block diagram of specialized DFT processor in SDPCM format.

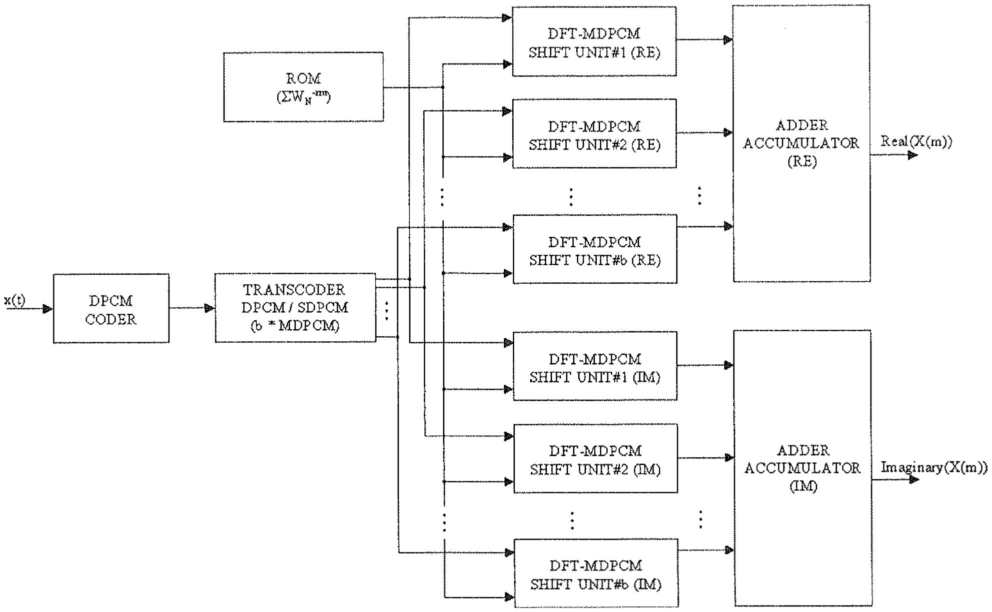

Fig. 6. General block diagram of specialized DFT processor with the use of SDPCM format

The structure presented in figure 6 includes $2 \cdot b$ shift units evenly divided into the real (RE) computing part and imaginary (IM) computing part. The ROM stores the earlier computed sum of the terms W_N^{-rm}. The TRANSCODER defines the MDPCM quantization steps, which assume the shift of sums of terms W_N^{-rm} stored in fixed-point numbers in multibit PCM code. After the parallel shift, all intermediate results are added and accumulated (ADDER-ACCUMULATOR) separately for real part (RE) and imaginary part (IM) of the DFT result.

6. STUDIES OF THE CALCULATION RATE OF DFT AND DCT SPECIALIZED PROCESSORS STRUCTURES

Presented in section 5 structures of differential specialized DFT and DCT processors include two operations done most often during signal processing, that is: multiplication and summation. As this work concentrates on the use of the shift operation replacing multiplication operation, we compare only the calculation rate of these two operations with the application of differential DFT and DCT processing. The calculation rate simulations were done with the use of the program packet ISE WebPack

8.1.02i of the firm XILINX. To the simulations in this program the FPGA Virtex-4 LX XC4VLX25 device was chosen.

The studies focused on working out the structures of the multiplication and shift of two code words, one with the length 8, 16 and 32-bits in PCM format type sign-module or two's complement notation (U2) and the other, low bit code word with the length 2, 3, 4 or 5-bits represented in MDPCM format type sign-module or U2. Next, the synthesis was done with the use of the module Synthesize – XST of the packet ISE WebPack the value of Maximum Combinational Path Delay was read from the report named Synthesis Report. This value corresponds to maximal determined path delay in combination system and it is presented in nanoseconds for particular realization of this system. This parameter was assumed as the time of one operation to be done in the studied system. Because this time equaled multiplication time, we omitted this solution in the table with the results of simulations.

Regarding the type of the FPGA device optimized for logic application solutions [12, 13], the authors decided to apply, apart from the program "shift statement SLL", the shift bit simulation by means of the code words composing. In order to compare and emphasize the advantages that result from replacing a classical multiplication operation with a shift one, the results of the studies were presented in percent gain time. The "gain time" term means the percent decrease of the calculation time by replacing multiplication with shift operation, what is presented in table 4.

Table 4 demonstrates the code words marked as c_x and c_y. The word c_x relates to the quantisation steps presented in MDPCM type sign-module format whereas the word c_y means the multibit type sign-module of PCM samples. The results presented in table 4 were realized for three types of realization shift unit. The first realization marked "SHIFT without SLL" describes the simulation results of the shift operation by means of proper code words. The length of the input code word in this realization is different from the length of the output code word. The second way ("SHIFT with SLL") consists in using shift SLL statement which in VHDL (Very High Speed Integrated Circuits Hardware Description Language) is used to describe shift operation in XC4VLX25 device. The last method ("SHIFT $c_x = c_x$") is a modification of the first method with the assumption that the input code word c_x equals output code word c_z.

The percent gain of the calculation time in table 4 is determined by the realization of single shift operation. The realization of many such operations, particularly if they are done in a parallel way, considerably decreases the time of the calculations, what is connected with the reduction of the whole processing time.

The results presented in table 4 confirm the earlier assumption that the application of the shift unit instead of multiplication unit shortens the calculation time even by about 34%. The increasing calculation rate can be observed for each studied case. The gain of the computation time decreases when the length of the shift code word decreases. This property is connected with optimization FPGA devices to the multibit multiplication operations.

Table 4

The percent gain of computational time by replacing multiplication operations with shift operation for different code word length

Length of the code word c_x [number of bits]	Length of the code word c_y [number of bits]	Type of operation	Gain of the calculation time [%]
2	8	SHIFT without SLL	32.98
		SHIFT with SLL	33.28
		SHIFT $c_x = c_z$	33.28
2	16	SHIFT without SLL	32.45
		SHIFT with SLL	32.47
		SHIFT $c_x = c_z$	32.47
2	32	SHIFT without SLL	34.14
		SHIFT with SLL	34.17
		SHIFT $c_x = c_z$	34.17
3	8	SHIFT without SLL	28.64
		SHIFT with SLL	28.95
		SHIFT $c_x = c_z$	28.53
3	16	SHIFT without SLL	23.57
		SHIFT with SLL	23.72
		SHIFT $c_x = c_z$	23.63
3	32	SHIFT without SLL	29.04
		SHIFT with SLL	29.07
		SHIFT $c_x = c_z$	28.99
4	8	SHIFT without SLL	31.39
		SHIFT with SLL	25.47
		SHIFT $c_x = c_z$	24.96
4	16	SHIFT without SLL	27.56
		SHIFT with SLL	20.32
		SHIFT $c_x = c_z$	19.79
4	32	SHIFT without SLL	30.87
		SHIFT with SLL	23.00
		SHIFT $c_x = c_z$	22.51
5	8	SHIFT without SLL	21.07
		SHIFT with SLL	15.81
		SHIFT $c_x = c_z$	17.28
5	16	SHIFT without SLL	10.47
		SHIFT with SLL	12.29
		SHIFT $c_x = c_z$	9.72
5	32	SHIFT without SLL	25.19
		SHIFT with SLL	23.97
		SHIFT $c_x = c_z$	21.66

Work [5] shows that the same or higher SNR value with the application of PCM code we obtain by using MDPCM code that has smaller number of bits. If we use this property, the gain of the calculation time, while applying shift operation, increases even up to 42% .

Analyzing the results of the studies presented in table 4, we can see that different structures of the shift units in different degree increase the percent gain of the calculation time. Therefore, the results presented in table 4 can be increased by the application of other FPGA devices and also by the application of different way of the shifts with the use of various programs in VHDL language which are not presented in this article. We should also take into consideration that the usage of the same source codes that describe the shift units in other FPGA devices, in particular other firms, can lead to obtain other results.

7. CONCLUSION

In this work the authors presented some methods of increasing the accuracy and the computation rate of the DFT and DCT algorithms. One of these methods was the application of the SDPCM format in the above algorithms. The SDPCM code is created from parallel combination of a few MDPCM codes, whereas the MDPCM code is created from the modification of the DPCM format in which the quantization steps are chosen from the set of the power of 2 with exponents belonging to a natural numbers set. Such approach makes possible to replace the time-consuming multiplication operations with fast shift ones.

The other way of increasing the accuracy and the computation rate of DCT is the modification of a part of the DCT spectrum components. The results of DCT spectrum modification presented in this work show that in each studied case the application of the method based on zeroing the DCT components can considerably increase the SNR value (the higher increase of the SNR is for higher sampling rate) in comparison to DCT done without spectrum modification.

In order to use the new DFT and DCT algorithms in SDPCM format the structures of the specialized processors were worked out. The structures work without multiplications operations and may be applied in programmable devices such as FPGA. By the use of FPGA simulating program it was proved that the calculation rate considerably increases while replacing multiplication operations with the shift operations.

Presented in the article DFT and DCT algorithms, structures of specialized processors and methods of the DCT spectrum modification enable the fast and accurate calculations to be done in the real time and they are expedient to be used in FPGA devices.

8. ACKNOWLEDGMENTS

This work has been realized by the support of Polish Ministry of Science and Higher Education, under the project No. N517 016 31/2578.

9. REFERENCES

1. D. Hankerson, G.A. Harris, P.D. Johnson: *Introduction to Information Theory and Data Compression*, CRC Press, Boca Raton, 2nd edition, 2003.
2. D. Salomon: *Data Compression. The Complete Reference*, Springer-Verlag, New York, 3rd edition, 2004.
3. K.R. Rao, P. Yip: *Discrete Cosine Transform – algorithms, advantages, applications*. San Diego, Academic Press, 1990.
4. R.N. Bracewell: *The Fourier Transforms and its Applications*, McGraw Hill, Singapore 2000.
5. W. Pogribny, M. Drechny: *Różnicowa DCT w zagadnieniach przetwarzania sygnałów*, Kwartalnik Elektroniki i Telekomunikacji, tom 52 zeszyt 4, ss. 797-813.
6. P.J. Grewen, W.F.G. Mecklenbräuker, N.A.M. Verhoeckx, F.A.M. Snijders, H.A. van Essen: *A New Type of Digital Filter for Data Transmission*. IEEE Transaction on Communications, vol. 23, issue 2, February 1975, pp. 222-234.
7. T.P. Zieliński: *Cyfrowe przetwarzanie sygnałów, od teorii do zastosowań*, WKiŁ, 2005.
8. U. Meyer-Bayese: *Digital Signal Processing with Field Programmable Gate Arrays*, Springer-Verlag, 2001.
9. N. Ahmed, T. Natarajan, K.R. Rao: *Discrete Cosine Transform*. IEEE Transaction on Computers, vol. 23, January 1974, pp. 90-93.
10. W.B. Pennebaker, J.L. Mitchell: *JPEG Still Image Data Compression Standard*, Van Nostrand Reinhold, New York, 1993.
11. W. Pogribny, I. Zelinski: *Differential coding and processing of images*, Proceedings of SPIE: Diagnostic Imaging, Technologies and Applications, vol. 3827, Bellingham, Washington, 1999, pp. 155-163.
12. http://www.xilinx.com/bvdocs/userguides/ug070.pdf – 27.11.2006.
13. http://www.xilinx.com/products/silicon_solutions/fpgas/virtex/virtex4/overview/index.htm – 27.11.2006.

ELECTRONICS AND TELECOMMUNICATIONS QUARTERLY, 2007, 53, no 2, pp. 177–191

Directly Modulated Lasers in Chromatic Dispersion Limited 10 Gb/s Links

PRZEMYSŁAW KREHLIK

AGH University of Science and Technology
Mickiewicza 30 Ave., 30-059 Krakow
e-mail:krehlik@agh.edu.pl

Received 2006.10.26
Authorized 2006.12.13

In the paper the usefulness of directly modulated lasers in 10 Gb/s links suffering significant chromatic dispersion is investigated. The influence of laser chirp characteristics on transmission system performance is analysed and optimal laser driving conditions, significantly reducing destructive impact of the chirp, are pointed out. The results of the work are experimentally verified.

Keywords: directly modulated lasers, laser chirp, dispersion penalty

1. INTRODUCTION

10 Gb/s fiber links are widely used in long-haul transport networks. The development of high-capacity Metropolitan Area Networks (MANs) that are less demanding in terms of transmission distance, but strongly cost-sensitive, attracts the designers attention to high-speed, directly modulated transmitters.

Directly modulated lasers (DMLs) exhibit significant frequency chirp that interacts with fiber chromatic dispersion, causing the distortions of the signal travelling along the fiber. Impact of this effect increases approximately with square of bit rate [1], so being of less importance in sub-Gb/s region, become one of main system limitations in 10 Gb/s links. The significance of laser chirp is most pronounced in systems exploiting standard single-mode fiber (SSMF) in 1.55 μm window. The relatively high, positive dispersion of the fiber causes broadening of chirped pulses, what induces inter-symbol interferences (ISI), limiting transmission distance.

Although the chirp problem may be overcome by external laser modulation (using Mach Zhender or electroabsorption modulator), the use of DML is attractive for various reasons; DML is substantially cheaper, it need much smaller modulating current and offers higher fiber-coupled power. Additionally, the commercially available DMLs cover all 16 CWDM channels, which enables cost effective gradual upgrading of the existing networks.

In this paper the impact of laser chirp characteristics on the chirp-dispersion induced signal distortions will be investigated. Optimal laser driving conditions, depending on its chirp characteristics, will be pointed out. Also the distance limitations for 10 Gb/s transmitters equipped with nowadays commercially available multi-quantum well distributed feedback (MQW-DFB) lasers will be specified.

2. LASER CHIRP CHARACTERIZATION

Direct intensity modulation leads to some variation of carrier concentration in the laser active region, which affects the refractive index and so the frequency of generated optical signal. Thus the laser intensity modulation results in frequency chirp. The chirp is usually described by the following equation [2]:

$$\Delta \nu(t) = \frac{\alpha}{4\pi}\left(\frac{1}{P(t)}\frac{dP(t)}{dt} + K_\nu P(t)\right), \tag{1}$$

where $\Delta\nu(t)$ is instantaneous frequency deviation, α is so called line enhancement factor, K_ν is the adiabatic chirp coefficient, and $P(t)$ is the laser output power. The first term in above equation, proportional to derivative of output power is called the transient chirp, and the second one, directly proportional to the power, is the adiabatic chirp. It should be mentioned that Eq. 1 was derived for the single-mode Fabry-Perot (FP) lasers, but it is also widely used as useful approximation for DFB ones [3–8].

Table 1

Chirp parameters of some MQW DFB lasers

laser no.	type, vendor	α	K_ν [Hz/W]
1	PT3563, Photon	2.7	$8.0*10^{12}$
2	PT3563, Photon	2.4	$7.9*10^{12}$
3	C15D, Lasermate	3.15	$4.8*10^{12}$
4	DFBLD-15-05, AOC	9.1	$10.5*10^{12}$
5	NLK-1551-SSC, NEL	2.7	$2.0*10^{12}$
6	unknown	5.6	$1.5*10^{12}$
7	unknown	2.2	$28.7*10^{12}$

Transient chirp is proportional to output power derivative related to instantaneous power value. Thus, in fact, it is determined by the power waveform shape, regardless of its magnitude. Additionally it may be noticed that adding some constant value (the waveform pedestal), what is the case of typical above-threshold laser bias, reduces the transient chirp. In contrast, adiabatic chirp is proportional to absolute power value and so is more pronounced in lasers operating with higher output powers.

In Tab. 1 measured chirp parameters of some commercially available high-speed MQW DFB lasers are collected. First four devices (two of the same type) are measured by author (see Ref. [7]), three others are taken from [4, 8].

3. TRANSMISSION SYSTEM MODELLING

The transmission system model, used to investigate the chirp-dispersion influence on transmitted signal distortions and resulting link performance deterioration, will be briefly described in current section. The model components are depicted in Fig. 1.

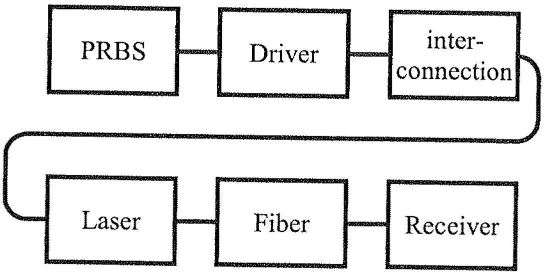

Fig. 1. Transmission system model

The data sequence is generated by pseudo-random bit sequence generator (PRBS). In laser driver model the bias and modulation currents are combined, and output current waveform with typical rise/fall time of 30 ps is produced. The shapes of current slopes are behaviourally modelled by the hyperbolic tangent function. Standard NRZ signalling is assumed.

Next, the driver-laser interconnection is modelled. It should be realized that for the ultra-fast modulation, as 10 Gb/s, any parasitic capacitances and inductances of driver package, PCB connection and laser assembly, together with matching and damping resistors involved in the circuitry, cause the low-pass filtration of the current reaching laser chip. Because the actual transfer function of the interconnection can not be separately measured, the fourth-order low-pass transfer function was taken as its model. For the driver-laser setup used in author's experiments, the Besssel transfer function with 7 GHz cut-off frequency leads to good agreement between simulated and measured laser output waveforms.

The laser dynamics is modelled by standard rate equations [6]. Two sets of parameters were used. The first one, taken after [9], describes 10 Gb/s rated MQW-DFB device (D1861A by Agere). The second one was obtained by the author for the slower, 2.5 Gb/s rated laser (PT3563 by Photon). It should be mentioned that the PT3563 laser, although rated for 2.5 Gb/s, can also be modulated at 10 Gb/s rate, but produces the output signal with longer and more asymmetric rise and fall slopes, lower relaxation oscillation frequency, etc. Thus, having two different models, the potential interaction of this features with laser chirp and fiber dispersion may be observed. Additionally, in some simulations presented below the laser dynamic model will be omitted in the manner that laser output optical power is simply proportional to driving current. This situation will be called as "idealized laser dynamics".

The laser chirping is modelled by the Eq. 1. The output power and chirp are combined in the form of complex envelope of optical field at laser output [10]:

$$E(t) = \sqrt{P(t)}\exp[j\phi(t)], \tag{2}$$

where $P(t)$ is laser output power and $\phi(t)$ is integral of laser frequency deviation:

$$\phi(t) = 2\pi\int_0^t \Delta\nu(t)dt. \tag{3}$$

The impulse response of dispersive medium, describing evolution of the signal complex envelope [10], is taken as dispersive fiber model:

$$h(t) = \sqrt{j\frac{c}{zD\lambda^2}}\exp(-j\frac{\pi c}{zD\lambda^2}t^2), \tag{4}$$

where z is the fiber length, and D is dispersion coefficient, defined as $d(1/v_g)/d\lambda$, λ is wavelength of optical signal and c is velocity of light in vacuum. (In above equation terms concerned with fiber attenuation and delay are neglected, as they do not influence the signal shape and are out of interest herein.)

The output signal complex envelope is the convolution of input envelope with fiber impulse response. Finally, the output power is square of output envelope absolute value.

The receiver is modelled as so called "reference receiver", described by the fourth-order low-pass Bessel transfer function with 7.5 GHz cut-off frequency. Such frequency characteristic is specified by standardization bodies, implemented in measurement equipment and (more or less precisely) in commercially available receiver modules.

4. CHIRPED SIGNAL DISTORTIONS – ILLUSTRATIVE EXAMPLES

For the simple illustration of chirp induced signal distortions some examples are presented in Fig. 2. Upper traces show the evolution of chirped 100 ps pulse, that may be regarded as ...00100... sequence in 10 Gb/s data stream, and lower ones show the corresponding eye patterns. Laser chirp parameters $\alpha = 3$, $K_\nu = 30*10^{12}$ Hz/W was taken, and 15 km of standard fiber with dispersion coefficient of 17 ps/nm*km was assumed. Fig. 2(a) shows the signal at the laser output. Not to be involved into any second-order effects concerned with particular laser dynamic model, the idealized dynamics was taken this time. In Fig. 2b the signal at fiber output is presented, in the case when only transient chirp component was taken in laser chirp modelling. The explanation of the distorted pulse shape may be as follows: The rising edge of the input pulse undergoes the positive frequency shift (blue shift) and thus propagates in the fiber with higher group velocity than the central part of the pulse. The falling edge undergoes negative frequency shift (red shift), so propagates slower. This cause the pulse broadening, or even time separation of the energy forming the input pulse slopes from that forming its central part, what becomes visible in Fig. 2(b).

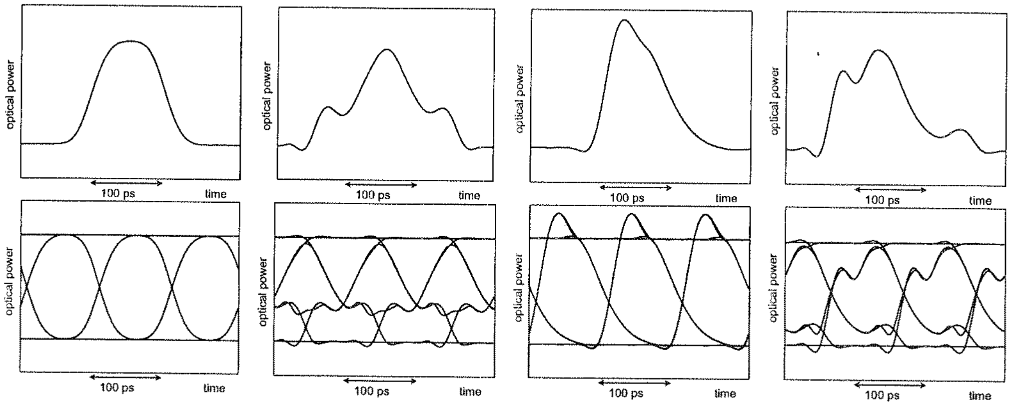

(a) (b) (c) (d)

Fig. 2. Illustration of chirp induced signal distortions: (a) undistorted, (b) affected by transient chirp, (c) by adiabatic chirp, (d) by both chirp components

Adiabatic chirp taken alone (see Fig. 2(c)) leads to increase of group velocity of subsequent pieces of signal rising edge. Thus the output pulse rises faster than input, and even some overshoot may occur. Analogously subsequent pieces of falling edge travels slower than previous ones, so output falling edge is extended.

Fig. 2(d) illustrates the combined effect of transient and adiabatic chirp. The output pulse shape is quite complicated, with its actual appearance strongly dependent on input pulse shape, the relation between the transient and adiabatic chirp components, and fiber dispersion.

5. IMPACT OF LASER CHIRP ON TRANSMISSION PERFORMANCE

In current section the impact of laser chirp parameters and driving conditions on transmission system performance will be analysed. The dispersion induced power penalty will be taken as quantitative measure of signal degradation.

To calculate the power penalty, the receiver output signal should be sampled in (or around) the middle of symbol duration, as in real transmission system. However, the sampling phase is not evident in case of strongly distorted signal, specially when oscillations at signal slopes cause multiple crossing of discrimination level, as illustrated in Fig. 3(a) by black lines. Thus the operation of the clock recovery PLL with Hogge's phase detector [11] was simulated to determine the sampling phase. To get more realistic results the power penalty was calculated not only for signal sampling phase determined as described above, but also with ±0.1 UI offset, and the worst value was taken as final result. This way some possible phase offset of clock recovery circuit and nonzero aperture of decision circuit are taken into account, what is specially important in case of strong horizontal eye closure (see fig 3(b)).

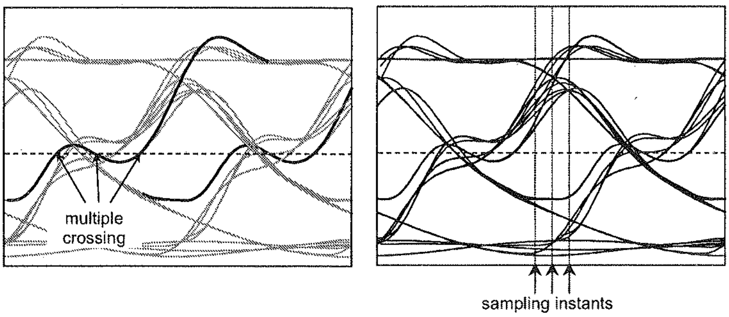

(a) (b)

Fig. 3. A distorted eye pattern with: (a) multiple discrimination level crossing marked, (b) three sampling phases shown

In the following investigations the power penalty will be related to transmission distance, with dispersion coefficient of 17 ps/nm*km assumed. Generally, the penalty depends on the product $D * z$, called accumulated dispersion, so this quantity will be also specified.

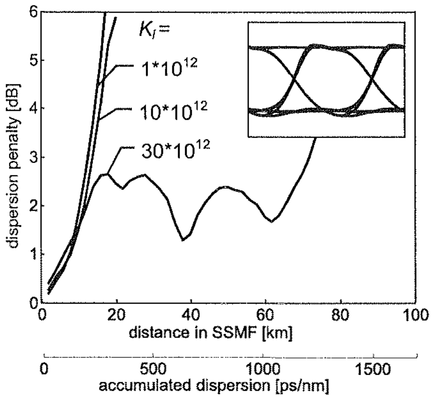

Fig. 4. Dispersion penalty versus distance (accumulated dispersion). The laser output eye pattern in inset

In Fig. 4 the dispersion induced power penalty is plotted for the moderate value of line enhancement factor $\alpha = 3.0$, and adiabatic chirp coefficient K_ν varied from $1*10^{12}$ Hz/W to $30*10^{12}$ Hz/W. The modulation and bias currents were chosen to obtain the moderate extinction ratio (ER) of 5 dB, and 3 dBm laser output power in high state (P_H). The D1861A device dynamic model was used; resulting laser output eye pattern is presented in inset.

It may be noticed that for distances up to about 10 km the dispersion penalty increases monotonically with the distance, being practically independent on the laser adiabatic chirp coefficient. However, the significance of adiabatic chirp manifests for longer distances – higher values of adiabatic chirp coefficient can mitigate dispersion penalty and allow transmission for much longer distances. Similar results were obtained using the PT3563 device dynamic model, and also idealized laser dynamics.

Taking different values of the line enhancement factor, the extension of moderate dispersion penalty region also occurs in case of high adiabatic chirp coefficient (see Fig. 5). However, ignoring some local perturbations, higher values of α lead to much worse results.

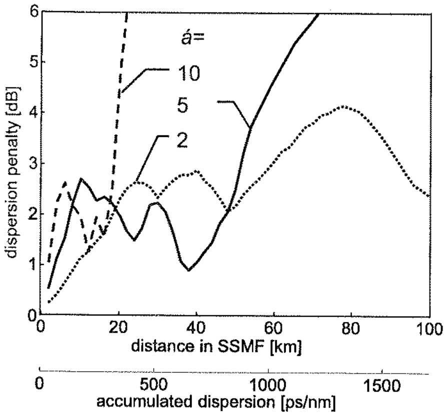

Fig. 5. Dispersion penalty for different values of line enhancement factor. $K_\nu = 30*10^{12}$ Hz/W

The observation that significant adiabatic chirp reduces the signal degradation caused by the transient one may be, with some simplification, explained with help of Fig. 6. In this simulations $\alpha = 2.0$, $K_\nu = 40*10^{12}$ Hz/W, and idealised laser dynamics were assumed. The separated "1" pulse at the laser output is shown in Fig. 6(a), together with the eye pattern in the inset. In case when only transient chirp is present (shown in Fig. 5(b) by the dashed line), the rising edge of the pulse travels faster, and falling one slower than the central part, so the pulse is significantly spread at the fiber output. Its shape, after 30 km of SSMF is presented in Fig. 6(c) by the dashed line. Summing the transient chirp with sufficient amount of adiabatic one may form nearly rectangular shape of total chirp, as shown in Fig. 6(b) by solid line. In this case main part of the pulse energy (entire rising edge and the central part) undergoes large, but nearly constant (!) chirp, thus is "left shifted" in time domain, without significant deformation. Only falling edge undergoes varying chirp and so is seriously extended. The resulting pulse is presented in Fig. 6(c) by solid line, together with the fiber output eye pattern. As may be observed, the eye is not seriously distorted, and resulting power penalty is only 0.5 dB. In contrast, the transient chirp alone will cause 8 dB penalty in the same circumstances.

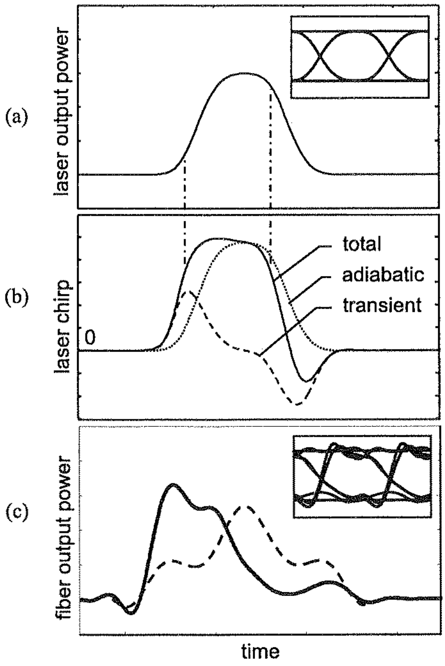

Fig. 6. The illustration of transient and adiabatic chirp interaction

Comparing many simulations with idealized and realistic models of laser dynamics it was observed that in case of realistic model the positive influence of adiabatic chirp is usually less efficient. It was found that any oscillations presented in the laser output waveform (caused by laser relaxation characteristics and/or by driver and interconnection circuitry) acts destructively. Oscillating signal produces also oscillating and less regular chirp, resulting in greater dispersion induced signal distortions. Additionally, the nonlinear laser dynamics causes output power rising slope steeping, what enhances transient chirp and disturbs the desired balance between chirp components.

In transmitters working with 10 Gb/s modulation laser output rise and fall times should be very short and so the transient chirp is extremely pronounced. Thus the adiabatic component needed for the described above pulse "reshaping" is also large, calling for laser with high value of K_v. Among the lasers characterized in Tab. 1 only the last one has adiabatic chirp coefficient sufficient to balance the transient chirp in circumstances taken in above reported simulations. However, the proportions between transient and adiabatic chirp components may be affected by modification of laser modulation conditions, thus their influence should be investigated in following section.

6. OPTIMISATION OF LASER MODULATION

First the depth of modulation, characterized by the resulting extinction ratio will be discussed. From Eq. 1 it may be found that for any given power waveform lifting its DC pedestal reduces the transient chirp (because it reduces the $1/P(t)$ term not changing the $dP(t)/dt$). The adiabatic chirp component is not affected by the DC pedestal value (neglecting some constant frequency shift), thus also the proportion between chirp components may be affected by changing of ER. On the other hand the value of optical modulation amplitude (OMA) for given, constant ER affects only adiabatic chirp, so it is also the factor influencing the desired chirp components balance.

Looking for laser driving conditions leading to maximum transmission distance not only the dispersion induced power penalty but also the transmitter penalty resulting from limited ER should be taken into account. The transmitter penalty is defined herein as the difference in system power budget between the cases of ideal transmitter with on-off optical power modulation, and actual transmitter with given limited extinction ratio (and also some signal distortions caused by the non-ideal laser dynamics). In following figures the sum of transmitter and dispersion penalty will be plotted versus transmission distance, together with the limit resulting from receiver sensitivity. This limit is defined as idealized link power budget minus fiber attenuation minus some additional "lumped" attenuation, caused for instance by CWDM multiplexers, optical switches, connectors etc. The idealized link budget is transmitter OMA (in dBm) when ideal on-off power modulation is assumed, minus receiver sensitivity (in OMA, dBm). The receiver sensitivity of −16 dBm, fiber attenuation 0.2 dB/km, and lumped attenuation 5 dB were taken in simulations presented below. The laser ER was modified in the manner that high-state power (P_H) was constant, and only low-state value was adjusted.

Fig. 7 shows the transmitter plus dispersion penalty against sensitivity limit in case of very low laser adiabatic chirp coefficient, for ER varying from 3 dB to 8 dB. It may be noticed that maximum transmission distance is around 20 km, nearly regardless on taken ER. Also possible increasing of laser output power, although lifts up the sensitivity limit, will result only in minor improvement, because of very rapid growth of the dispersion penalty. Similar plots obtained for higher values of line enhancement factor show nearly proportional reduction of attainable distances (e.g. about 12 km for $\alpha = 5$), without any qualitative differences observed in the plots. Thus for transient chirp dominated laser there is in fact no room for any efficient optimisation of driving conditions.

More promising results were obtained in case of medium adiabatic chirp coefficient (see Fig. 8). Taking (as previously) 3 dBm high-state laser power (see Fig. 8(a)) the maximum transmission distance is still about 20 km, similarly as for low adiabatic

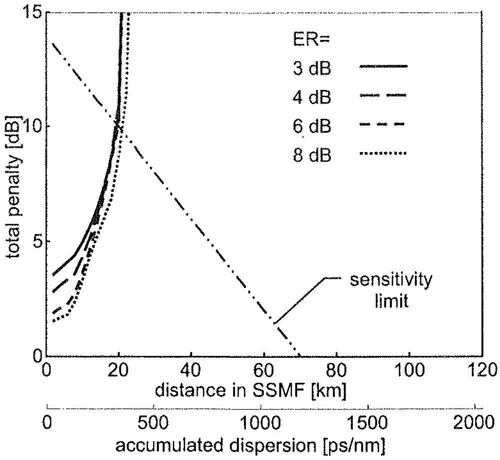

Fig. 7. Total power penalty versus distance; $\alpha = 3$, $K_{\nu} = 1*10^{12}$ Hz/W, $P_H = 3$ dBm

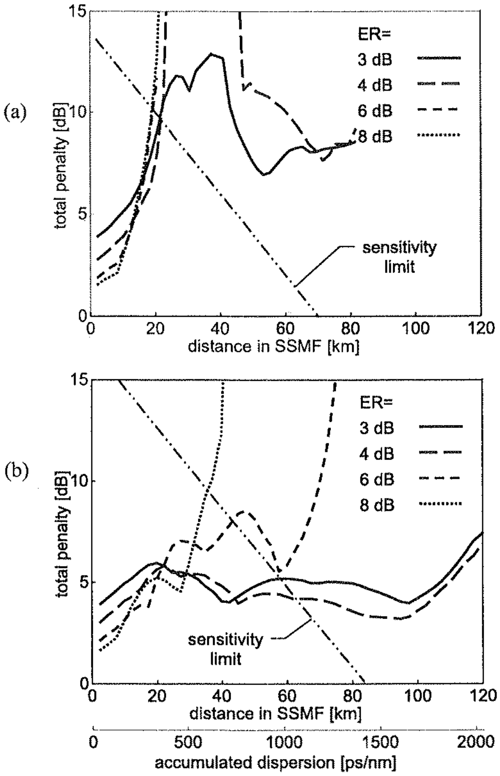

Fig. 8. Total power penalty versus distance; $\alpha = 3$, $K_{\nu} = 10*10^{12}$ Hz/W, (a) for $P_H = 3$ dBm, (b) for $P_H = 6$ dBm

chirp case, presented in Fig. 7. Although for low ER the dispersion penalty growth tends to be limited for greater distances, the total penalty still exceeds the sensitivity limit for relatively short distances. However, for laser high-state power increased to 6 dBm, the situation is significantly improved (see Fig. 8(b)). The main difference is that power penalty is dramatically reduced, particularly for lower values of ER. As it was already mentioned, the transient chirp does not depend on magnitude of optical power waveform, so for given ER it is not affected by power increase. Adiabatic chirp however, is twice as much for two times higher power, what in our case is sufficient to limit the dispersion penalty. Additionally, the increased laser power lifts 3 dB up the sensitivity limit. Finally, for ER in range of 3 ... 4 dB spectacular improvement of transmission distance, to about 60 ... 65 km, may be achieved for laser allowing strong enough driving. (It may be noticed that moderate power penalty extends up to about 100 km so even such distance may be achieved using optical amplification or more sensitive, avalanche photodiode based receiver.)

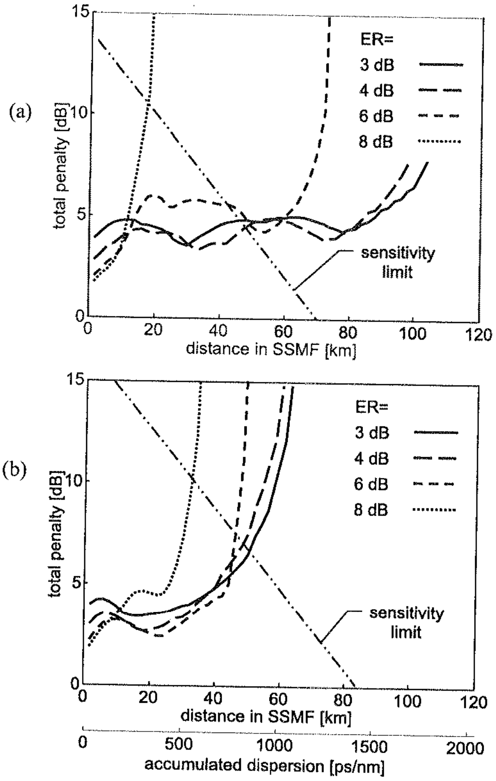

Fig. 9. Total power penalty versus distance; $\alpha = 3$, $K_\nu = 30 * 10^{12}$ Hz/W. (a) for $P_H = 3$ dBm, (b) for $P_H = 6$ dBm

For high adiabatic chirp coefficient (see Fig. 9(a)) the maximum transmission distance of about 50 km can be obtained for ER in range of 3 ... 4 dB and $P_H = 3$ dBm.

Fig. 9(b) shows the plots obtained for the same adiabatic chirp coefficient, but stronger laser driving (P_H = 6 dBm). In present case (i.e. high value of K_ν) the increasing of laser power does not improve, even deteriorates the situation. Although the maximum distance is still about 50 km, but the power penalty is evidently rising for distances greater than 20 km, which means serious dispersion induced signal distortions. It was also observed that besides the dispersion penalty, being related rather to vertical eye closure, additionally significant horizontal closure arises. Even for small ER horizontal eye opening drops below 0.5 UI at distance about 40 km. Comparison of eye patterns obtained for weaker and stronger laser driving is presented in Fig. 10. (ER = 3 dB and transmission distance of 40 km were taken.) Significant oscillations and horizontal closure are visible in Fig. 10(b), in contrast to quite "clear" eye in Fig. 10(a).

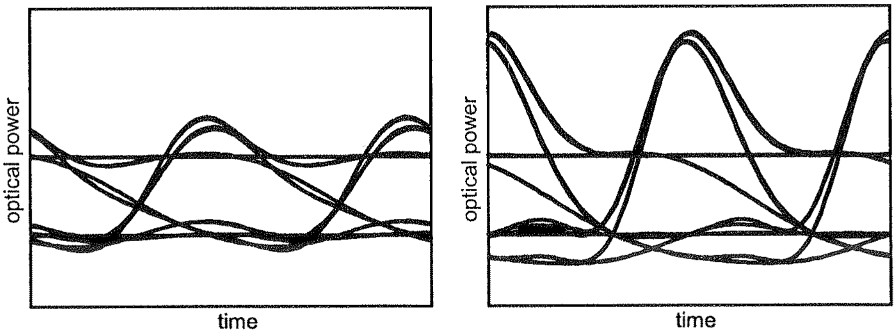

(a) (b)

Fig. 10. Filtered eye patterns at the output of 40 km fiber; α = 3, K_ν = 30*10^{12} Hz/W, ER = 3 dB. (a) for P_H = 3 dBm, (b) for P_H = 6 dBm

Concluding the question of optimum laser driving and maximum transmission distance somehow irregular and not always monotonic influence of many factors on dispersion induced power penalty (and other signal distortions) should be pointed out first. From the engineering point of view the optimal laser driving is not exactly one that gives the maximum distance (or smallest power penalty) in some very particular circumstances, but rather giving good results for possibly wide range of accompanying factors. Simulations presented above, together with a lot of others (in those such factors as driver rise/fall time, laser dynamic model, receiver transfer function were modified) lead to general remarks as follows.

Generally optimal laser ER is about 3 ... 4 dB. Lower values reduce the OMA without significant gain in terms of dispersion penalty. Higher values usually strongly increase dispersion penalty and other signal distortions, as oscillations, pattern dependent slope jitter, horizontal eye closure. What is also important in practice, for high ER the dispersion penalty dependence on transmission distance and other accompanying factors is more irregular and less predictable. (Some additional advantage of recommended herein, relatively low ER is that it substantially relaxes the demands on laser dynamic behaviour, and gives the possibility of using even 2.5 Gb/s rated lasers in 10 Gb/s transmitters.)

Absolute values of laser output power levels, even for constant, desired ER, is important factor in cases of medium and high values of laser adiabatic chirp coefficient. For medium values of K_ν sufficiently high value of OMA leads to desired balance between transient and adiabatic chirp components and thus significantly extend the transmission distance. In case of very high K_ν, the adiabatic chirp may be much bigger that desired, which manifests in high dispersion penalty and/or significant horizontal eye closure. In such situation reduction of laser power (in manner not affecting ER) improves the situation. Generalizing this observations it may be stated that optimal amount of adiabatic chirp occurs when the product K_ν*OMA is in range $2*10^{10}$ ... $3*10^{10}$ Hz, or equivalently, $K_\nu * P_H$ is in range $4*10^{10}$ ... $6*10^{10}$ Hz.

The maximum attainable transmission distance depends strongly on laser chirp characteristics. For transient chirp dominated (i.e. with low K_ν) device it is determined mainly by the value of line enhancement factor. For $\alpha = 3$, which is rather a small value, it is about 20 km, for bigger α is nearly proportionally shorter. For lasers with greater adiabatic chirp coefficient, when the desired value of $K_\nu * P_H$ can be achieved, the maximum transmission distance in range of 50 ... 60 km may be obtained for devices with line enhancement factor not greater than 4.

Finally, the results of above investigations may be related to the existing standard specifications for 10 Gb/s transmitters. The ITU recommendations on STM-64/OC-192 systems demand minimum 8.2 dB ER and maximum 1 dB path penalty (including the dispersion penalty) [12], which in fact exclude the DML based transmitters in case of significant fiber dispersion. In contrast, IEEE 10GbEthernet standard specifies the 3 dB minimum ER, and up to 3 dB dispersion penalty [13] and thus accommodate properly designed DML based transmitters even for maximum specified operating distance (i.e. 40 km).

7. EXPERIMENTAL RESULTS

For verification of the above investigations some eye pattern measurements will be presented in following. The device under test was PT3563 laser. Taking into account its chirp characteristics (see Tab. 1) and the results of above discussions, it may be concluded that low ER and high value of P_H should be desired for proper transient to adiabatic chirp relation. P_H in range of +6 ... +8 dBm seems to be the best choice, however a bit smaller value (5 dBm) was chosen not to significantly exceed vendors specification on recommended output power. ER of 3 dB was taken.

The measurements were performed using the HP83480A digital communication analyzer (DCA) with HP83485B optical plug-in. The DCA bandwidth was reduced by internal 7.5 GHz low pass filter.

Eye patterns, measured at laser output and after 20, 40 and 60 km of SSMF are presented in Fig. 11. Although the presented eyes are strongly affected by DCA noise, theirs good opening, even after 60 km long fiber, is evident. Next the laser driving was modified to reduce P_H to +3 dBm, and increase the ER to 6 dB (which gives nearly the same OMA as previously). This time however, the eyes after 40 and 60 km of fiber were completely closed, and even this after 20 km fiber was seriously distorted.

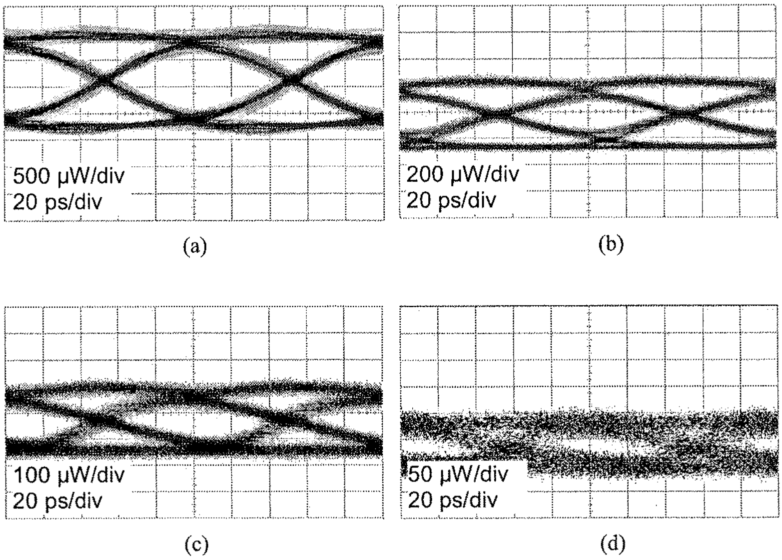

(a) (b)

(c) (d)

Fig. 11. Eye patterns measured after: (a) 0 km, (b) 20 km, (c) 40 km and (d) 60 km of standard fiber

Noticing that the chirp characteristics of the laser used are similar to that taken in considerations concerning the case of "moderate adiabatic chirp coefficient", the results agree very well with conclusions of above investigations, and shows the significance of laser driving conditions on transmitter performance.

8. CONCLUSIONS

The laser chirp characteristics and driving conditions are crucial factors determining performance of 10 Gb/s, DML based transmitters operating in 1.55 μm window over SSMF. As it was shown the chirp-dispersion caused signal distortions may be reduced to the amount allowing transmission distances even in range of 60 km, which is dramatically greater than a few kilometres, usually regarded as maximum distance [14].

To obtain high dispersion tolerance the laser with possibly low line enhancement factor (not greater than about 4) and, what is less evident, not too small adiabatic chirp coefficient is needed. It was found that relatively low dispersion penalty may be obtained taking ER in range of 3 ... 4 dB, and the OMA leading to desired balance between transient and adiabatic chirp components. Practical problem is that the lower is the adiabatic chirp coefficient, the greater power levels are needed for the balance. Thus the sufficient product of K_v by rated maximum output power determines the usefulness of a given laser in long haul application.

9. REFERENCES

1. G. P. Agrawal: *Fiber-Optic Communication Systems*. Wiley, 1997.
2. G.P. Agrawal, N.K. Dutta: *Long-Wavelength Semiconductor Lasers*, Van Nostrand Reinhold, New York, 1993.
3. G. Morthier, P. Vankwikelberge: *Handbook of Distributed Feedback Laser Diodes*, Artech House, London, 1997.
4. I. Tomkos *et al*: Extraction of laser rate equations parameters for representative simulations of metropolitan-area transmission systems and networks. Optics Communications, 194 (2001), 109-129.
5. K. Hinton, T. Stephens: Modelling high-speed optical transmission systems. *IEEE* J. Select. Areas Commun. 11 (1993) 380-392.
6. P. J. Corvini, T. L. Koch: *Computer simulation of high-bit-rate optical fiber transmission using single-frequency lasers*. Journal of Lightwave Technology 5 (1987) 1591-1595.
7. P. Krehlik: Characterization of semiconductor laser frequency chirp based on signal distortion in dispersive optical fiber. to be published in Opto-Electron. Rev. 14 (2006).
8. I. Tomkos *et al*: 10-Gb/s transmission of 1.55-μm directly modulated signal over 100 km of negative dispersion fiber. IEEE Phot. Tech. Lett. 13 (2001) 735-737.
9. B. Huiszoon *et al*: Cost-Effective Up to 40 Gb/s Transmission Performance of 1310 nm Directly Modulated Lasers for Short-to Medium-Range Distances, Journal of Lightwave Technology 23 (2005) 1116-1124.
10. B. E. A. Saleh, M. C. Teich: *Fundamentals of Photonics*. Wiley, 1991.
11. B. Razavi: *Design of Integrated Circuits for Optical Communications*. McGraw-Hill, 2002.
12. ITU-T 959.1 Recommendation on Optical transport network physical layer interfaces. ITU, 2003.
13. IEEE 802.ae Amendment to Standard 803.3. IEEE, 2002.
14. M. D. Feuer *et al*: Electronic dispersion compensation for a 10-Gb/s link using a directly modulated laser. IEEE Phot. Tech. Lett. 15 (2003), 1788-1790.

F
(
p
a
(
F
fi
st
n
e
a

K

Fro
interest
machin
of work
spite of
decidin
Th
In diffe
the me

ELECTRONICS AND TELECOMMUNICATIONS QUARTERLY, 2007, 53, no 2, pp. 193–219

Ferroic smart materials

ZYGMUNT SUROWIAK, DARIUSZ BOCHENEK, JOANNA KORZEKWA

Faculty of Computer Science and Materials Science
University of Silesia, Sniezna 2, 41-200 Sosnowiec
surowiak@us.edu.pl, dbochene@us.edu.pl

Received 2007.03.30
Authorized 2007.05.31

This paper presents the general properties of ferroic materials (crystals, ceramics). *Ferroics* is the general term covering ferromagnetic materials (FM), ferroelectric materials (FE) and ferroelastic materials (FES). Those three groups of materials are called "simple primary ferroics". *Ferroelasticity* is the mechanical or elastic analogue for ferromagnetism and ferroelectricity. The materials which exhibit both ferrioelectric (FE) and ferroelastic (FES) properties are described as *ferroelastoelectrics* (FE+FES=FESE). The ferroics (FM, FE, FES) and ferroelastoelectrics (FE+FES) belong to smart family materials. They are defined as materials which have some properties that can be altered and controlled by external stimuli (magnetic, electric, mechanical, thermal). Smart materials can be used in many technology fields such as automation, control process, robotics, material processing, aerospace engineering, automotive and electronic industry, defense technology, medical technology and biotechnology.

Keywords: ferroics, ferromagnetics, ferroelectrics, ferroelastics, smart materials

1. INTRODUCTION

From the beginning of mankind one of the most important fields of activity and interest of man was to design and construct implements of labour, installations and machines. Those conveniences main role was to make job easy, extend productivity of work, replace the man or animals muscles energy with another energy sources. In spite of huge technical achievements, the man, his intellect and intelligence still remain deciding factors of civilizations' evolution.

The intelligence (from Latin: *intelligentia*) is a notion from the psychology field. In different handbooks, encyclopedias and tracts there is no general definition but the meanings of definition are the same. One says that "*intelligence is the ability to* *understand surrounding situations and to find purposeful reactions for them*" [1], others say "*is the ability to understand at all; readiness; toward*" [2], or "*specific ability powers making individual possible to make efficient use of acquired knowledge and effective behaviour towards new problems and life conditions*" [3]. Despite compounds definition the "*intelligence*" term serves in psychology mainly to describe the level of general intellectual proficiency of people. The objective indicator or the measure of intelligence level is the intelligence quotient – IQ.

In the psychological literature *theoretical intelligence* (its task is to gain "pure" knowledge) contrasts with *practical intelligence* (which reveals in people action); with the practical intelligence *the technical intelligence* is related [3].

As a matter of fact, the intelligence notion is connected mainly with psyche and intellect of man but in parallel the intelligence investigations of another being (mammals, birds) are made, particularly of these, which serve man or often replace and help people out. Exceptionally "*high intelligence level*" is ascribed to dogs, horses, dolphins, monkeys, etc.

For many years it was only a dream but then also a human pursuit to construct a device (machine) designed to achieve some of manipulative, locomotive, informative or intellectual human actions. Such devices (to look like man, to have some intellectual properties, free from any feelings and capable of taking responsible decisions) for the first time were called Rossums Uniwersal Robots R.U.R. in 1920 by K. Capka. First built robots (**first generation robots**) realize task moving programs, i.e. they are capable of responsible carrying out and repeating programmable simple activities. **Second generation robots** (Massachusetts Institute of Technology, USA, 1961, i.e. Ernst manipulator) have different "*senses*" (touch, sight, hearing), they react to touch and sound signal, they have some ability to distinguish shape and colour, they react to ionization by radiation as well as react to changes of temperature, pressure, moisture, gas concentration, etc. The newest robots (**third generation robots**) are equipped with more "*developed senses*" (vision – that makes possible to observe environment changes and hearing – that makes it possible to voice communicate). They make use of *artificial intelligence systems*, which are based on computer technology.

The main purpose of artificial intelligence is solving problems with the help of computers to model on nature working, behavior and experience process of human being. The recognition of learning process and making use of knowledge by man in order to solve the problem that determines main matter of artificial intelligence and starting point to design computer programs, which stimulate human behavior and experience process. Some of the application examples of artificial intelligence are programs to shape recognition (i.e. writing letters or figures), sound recognition (i.e. language), game (i.e. chess), learning computer demand behavior, conversion mathematic formula, theorem provement, music composition, translation one nature language into another, etc.

When in 1955 J. McCarty from Massachusetts Institute of Technology (USA) thought up *the artificial intelligence* term and he probably did not realize how wise would the machines at the beginning of XXI century be. Nowadays computers control production process, airplane flight (automatic pilot), ship, train and road traffic, space and ballistic rocket flight. They also control the measurements system working and advanced automatic household equipment (kitchen equipment), etc.

There is no possibility to detail even the main area of application for the newest generation robots with artificial intelligence just in one article. In the developed countries there exist industrial plants (i.e. *unmanned* factory in Japan), where all activities, connected to production, are made by robots and the role of man here is only to be interested in observation of all production processes.

Robotics is the field of automation, which takes up the usage of robots, their mechanics, steering and design of machine intelligence.

Computer specialists equip computers more and more with new and excellent software, which systematically increases intelligence of electronic systems controlled by computers. We should think about scientific research on so-called *neuron network*, which means that programs imitate work of the particular cell in human brains. The essence of such network is possibility to learn through form connection between *neurons*. It has been successfully managed to create a network built up of a few hundred or thousands of neurons which are used in different ways for instance to detect suspicious shapes in passengers' luggage at the airport, to analyze roentgen pictures as far as various damages are concerned or to predict stock exchange tendencies. In each of these examples, network learns to recognize some formula by trial and error method and after many tests the network starts to be an expert in narrow given field. Since 1992 computer specialists have proposed the neutron network, which uses an evolution mechanism. They have carried out millions of tests and have rejected solutions witch suitability is the least.

Computer specialists and other researchers also observe nature and they think about the solution of coordinating work of many computers together. They observed, e.g. that insects colony exhibit intelligence although none of individual must not ascribe to it (*intelligence of million organisms*). It is about transferring that kind of solution to the world of computers and connecting millions of microprocessors to make an integral network. Vision of intelligent yoghurt, the artificial intelligence of future, has come out. It is, of course, not about yoghurt that we drink, but about suspension full of microprocessors, which seem to be like yoghurt. Creating that kind of suspension would be the crown of investigations about neutron network and civilization turning point. We should leave distant future for outstanding futurologists who are currently engineers, physicists, automation specialists and computer specialists working e.g. for British Telecom.

Nowadays, computers control activities of different sets of tools either in accordance to advance programs or in accordance to orders transfered with the use of radio waves or electrical impulses that have their source in different *sensors* types (sensing element, detector), and *transducers*. The temperature, pressure or radiation sensors, etc. and pyroelectric or piezoelectric transducers, etc. meet the role as nerves end in system with artificial intelligence. An inseparable part of these systems is specialized system of computer's memory.

The basis of building a system with artificial intelligence are special materials, which are characterized by specific physical activity. Getting such materials requires application of specialized technology, also nanotechnology. That type of materials was named *smart materials* in Massachusetts Institute of Technology (USA) already in the sixties. That notion is defined in a different way. Functional characteristic of such materials convey definition proposed in 2001 by A. Lawver from Face Intern. Corporation in Norflock (USA) [4]: "*The intelligent materials are materials, which react strongly and answer an external reaction* (sensors, transducers, etc.) and/or *serve to build various memory elements* (shape, information, etc.)". The family of smart materials is very numerous. Examples of such materials are shown in Fig. 1 and enclose both crystals, polycrystals (ceramic materials), composite materials and thin films and multilayer systems.

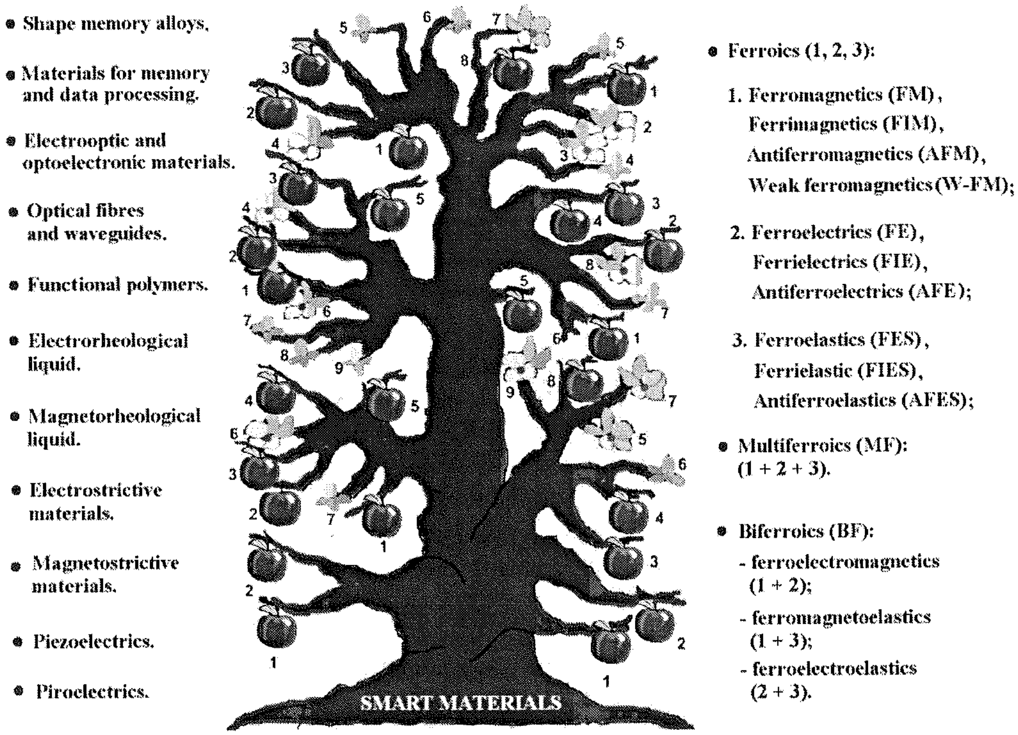

Fig. 1. The smart materials examples

Smart materials are not those, which have constant properties, which do not change under the influence of external reaction and those materials, which have inability to save the information, shape, etc. Materials are the smarter, the stronger they change their properties under the influence of external impulse or exhibit bigger capacity of the informatics memory etc. The answering function (response from stimuli) of smart materials is connected to strictly specified type of external reaction (i.e. electric impulse, radiation quantum with precise energy etc.) called *smart materials of first generation.* While materials, which strictly specify properties could undergo violent changes under influence of two or more different external stimuli (e.g. T, p, E, H etc.) exhibit higher intelligence, which means that they are *smart materials of second generation.*

In smart materials family there is no place for gold, silver, platinum, diamond and many other commonly respected and well known elements and compounds, which distinguish one's high stability, its physical properties and parameters. These materials do not react under influence of external reaction and in this way they behave according to the maxim: "*grandpa says to the picture whereas picture to grandpa neither one word*".

Among smart materials, which are used widely in electronics vision, ferroics (smart materials of first generation) and multiferroics (smart materials of second generation) take special place.

The following article, based on many references, include [23–47] as well as the results of own examinations. There will be smart material group (which have common name – ferroics) characterized in general way. There will be presented also some of the problems connected to their artificial intelligence (flexibility on external influence). In the field of ferroics more attention is given to ferroelastic and ferroelastoelectric materials as less known materials against to ferroelectric and ferromagnetic materials.

2. GENERAL CHARACTERISTICS OF FERROICS

The term ferroics was introduced by A. Aizu [27] in 1969 and it included a wide family of different materials that had in their name a prefix "ferro". Ferroics materials must not be associated with iron (from Latin. *ferrum*) or with its compounds.

Ferroics as smart electronic materials exhibit one of the following ordered states:

- the spontaneous state of magnetic ordered moments (ferromagnetic materials, antiferromagnetic materials, ferrimagnetic materials);
- the spontaneous state of electric ordered moments (ferroelectric materials, antiferroelectric materials, ferrielectric materials);
- the spontaneous state of structure deformation (ferroelastic materials).

In the ferroics classification the *type of order* is taken into consideration, which is the magnetic, electric or elastic system ordering. Thanks to this classification it was possible to include to ferroics family antiferromagnetic materials (AFM), ferrimagnetic materials (FIM) and antiferroelectric materials (AFE), ferrielectric materials (FIE) as well as antiferroelastic materials (AFES), and also paramagnetic materials (PM), paraelectric materials (PE) and paraelastic materials (PES), that is materials with disordered magnetic, electric or elastic states (Fig. 2).

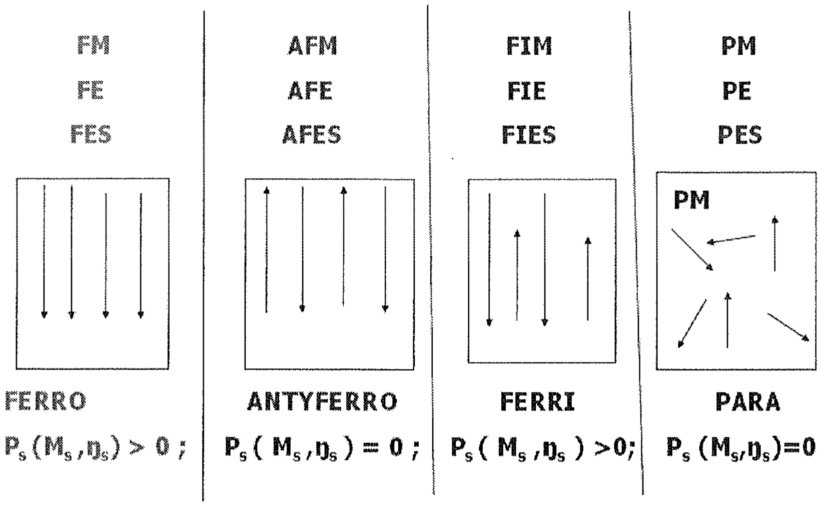

Fig. 2. The types of magnetic systems' order (PM, FM, AFM, FIM), electric systems' order (FE, AFE, FIE) and elastic systems' order (FES, AFES, FIES)

Having in mind different mechanisms describing the physical nature of spontaneous ordering of magnetic, electric and elastic systems it must not be disregarded that the whole conceptual, definitional and linguistic sphere concerning ferroelectric and ferroelastic materials has been drawn by analogy from knowledge about magnetism. It is fully justified not only for historical sake but also for the sake of considerably higher state of investigations within the range of ferromagnetic materials in relation to the rest' of ferroics.

The ferroics concept, which arose as a result of permanent tendency to generalization, which had been observed by years, has been accepted in physics, chemistry of the solid state and materials science, materials engineering, electronic engineering, etc. It also has been accepted for the language and definition analogies and analogies in properties range and practical application of these three groups of materials (FE, FM, FES), which are defined by common name.

The properties that integrate ferroics family among others are:

- ferroic state formation in *point of phase transition* as a result of small prototype crystalline structure deformation;
- *domain state* formation (as a consequence of spontaneous change of crystals symmetry);
- high value of some materials' *answer functions* in surroundings of a phase ferroics transition point;
- corresponding to their specific properties the order parameter (polarization P_s – for ferroelectric materials, magnetization M_s – for ferromagnetic materials and self-deformation η_s – for ferroelastic materials), which spontaneously takes the non-zero values in $T < T_C$, even in external influences absence;

- *hysteresis behaviour* of order parameters under the impact of external influence: (polarization P – under the influence of electric field E, magnetization M – under the influence of magnetic field H and deformation η – under the influence of mechanical stress σ (Fig. 3));
- ability to *store and release a huge energy under control* (electric, magnetic, mechanical energies), which has been found in many applications (Fig. 4).

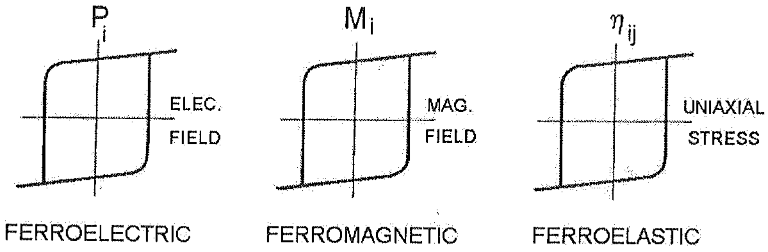

Fig. 3. Hysteresis behaviour of order parameters in ferroics under the impact of external influence [9]:

- in ferroelectric materials: polarization P_s – under the influence of electric field E;
- in ferromagnetic materials: magnetization M_s – under the influence of magnetic field H;
- in ferroelastic materials: deformation η_s – under the influence of mechanical stress σ

Artificial intelligence systems, based on ferroics, are controlled by strictly determined type of external influences (ferromagnetic elements with the help of magnetic field, ferroelectric elements – electric field and ferroelastic elements – mechanical stress field). However, ferroics' intelligence manifests not only in exhibiting main properties (FM, FE, FES) but also in exhibiting extra properties (i.e. ferromagnetic materials: pyromagnetic effect, magnetostrictive effect etc., ferroelectric materials: pyroelectric effect, electrostrictive effect, piezoelectric effect etc.). That is why ferroics elements could react also on the other stimuli (mechanical stress sensors, thermal radiation sensors etc.) and could convert one type of energy into another (magnetomechanical transducers, electromechanical transducers etc.).

For the hysteresis behaviours of order parameters reason, both ferromagnetic and ferroelectric based, the *informatics memory* systems could be built. In fig. 4 illustrating the possibilities of ferroics applications, purposefully did not ascribe mentioned examples to specific ferroics (FM, FE or FES), because most of the mentioned systems could work both on the basis of ferromagnetic and ferroelectric materials. Depending on specific application ferromagnetic or ferroelectric materials are preferred. The decisive meaning have set values of proper utilitarian ferroics parameters, compatibility with rest of the system elements and level of advance, simplicity and efficiency of production technology. Ferroics materials are obtained as monocrystal forms, polycrystal (ceramic) forms and thin-layer forms and also as composite forms. Nowadays, in the age of permanently progressive tendency to miniaturization of electronic smart materials and in the age of sudden development of nanotechnology, more and more massive monocrystals are supplanted by nanocrystalline ceramic powders and massive ceramic materials by ceramic layers and multilayer composite.

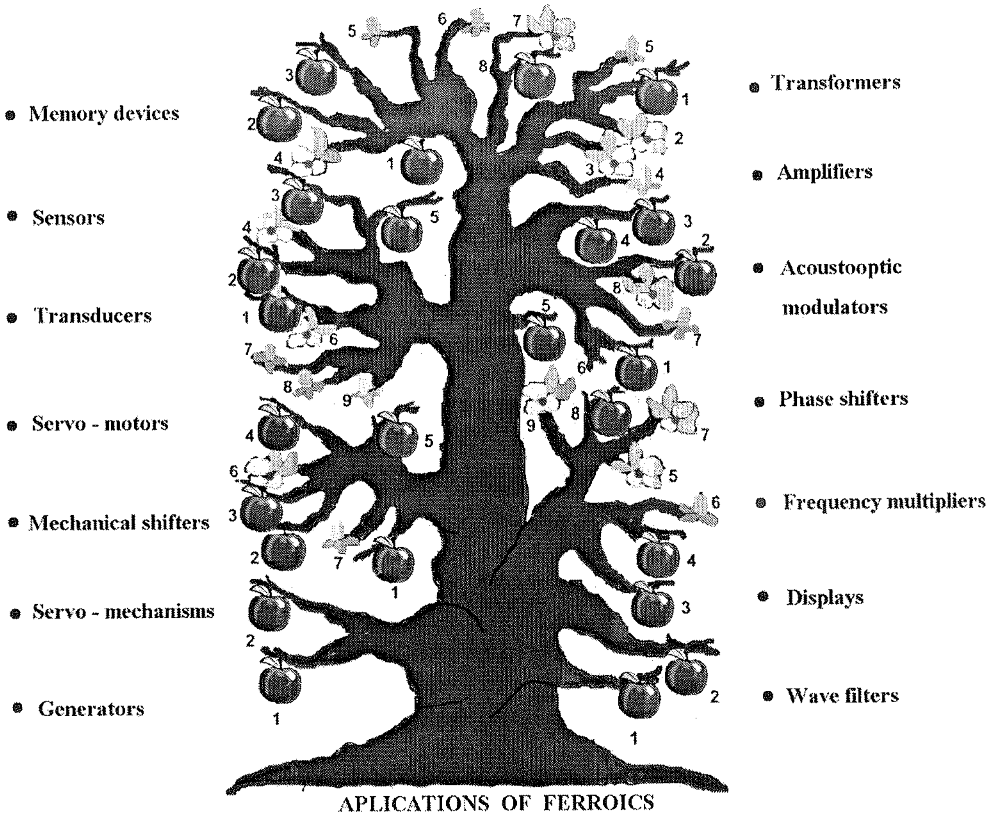

Fig. 4. Examples of ferroics applications

Each of crystalline body is characterised by precise *symmetry*. This symmetry could spontaneously change in suitable external conditions (temperature, pressure, electric field, magnetic field). Symmetry modification indicates the crystal transition from one phase to another. That effect is called *phase transition*. The most often crystals are not isotropic and exhibit different properties in different directions. In the phase transition spontaneous breach or decrease of directional symmetry is observed.

Ferroics are those crystals, where at least one phase transition occurs and changes directional symmetry in crystal (the lower directional symmetry the higher anisotropy of physical properties of crystals. Spontaneous transition of symmetry, during phase transformation, appearances in all ferroics (FM, FE, FES) and bonds ferromagnetic, ferroelectric and ferroelastic materials.

3. SPONTANEOUS CHANGES OF DIRECTIONAL SYMMETRY IN FERROICS

3.1. FERROMAGNETIC MATERIALS

A lot of monographs, textbooks and articles have described ferromagnetic (FM) properties, therefore this paper would be limited with information, which is connected to qualifications of that ferroic to smart materials family. First of all the subject of analysis will be iron.

In high temperature ($T > T_{CM}$) iron is in *paramagnetic phase* (PM). External magnetic field (H), which is applied to paramagnetic material, induces reaction in the form of magnetic moment with value proportional to field value H. In that case response function is *single – valued function*, i.e. function exhibits unequivocal value of induced magnetization M for all values of applied magnetic field H.

Transformation of paramagnetic phase (PM) to *ferroelectric phase* (FM) appears as a result of cooling iron crystal to T_{CM} temperature. In FM phase, crystal exhibits non – zero magnetic moment even during absence of external field H. This kind of magnetic moment was named *spontaneous magnetic moment* or spontaneous magnetization M_s. The appearance of spontaneous magnetization means that crystal got lower directional symmetry then the one in paramagnetic state. It is one of the examples of spontaneous symmetry breaking. Appearance of M_s is the consequence of spontaneous symmetry breaking, but it is just one of the effects. Recognition of the right mechanism of M_s appearance itself does interpret why the direction of M_s is not the same in whole crystal.

Imagine a square, with two sides in vertical direction and two sides in horizontal direction. Square transits to rectangle as a result of spontaneous decrease symmetry at Curie point. It could happen in two equally probable ways: vertical pair of square sides lengthen and horizontal pair becomes shorter or the other way round. Two equivalent orientation state of rectangle: parallel or perpendicular could be obtained. In that way in ferromagnetic crystal the domain structure could be form, indicate that regions with different direction of magnetization are formed. The least number of such directions has to equal at least two, but that kind of directions could be more. Domains are divided by domain walls (so-called Bloch walls), where progressive transition M_s, from one direction to the other, proceeds. When the magnetic field is high enough ($H > H_c$), the orientation M_s in whole domains could be the same. Transformation from one phase two another has hysteresis character (Fig. 3). When magnetic field is switched off ($H = 0$) magnetization does not disappear to zero, because the crystal is spontaneously magnetized. The *residual magnetization* M_R maintains. In order to remove the magnetization state ($M_R = 0$), appropriate strong magnetic field, which has opposite direction to this which produce $M_R \neq 0$, should be applied to crystal. Possibility of switching $M_R^{(+)} - M_R^{(-)}$ by external field is a basis of ferromagnetic information memory elements functioning at binary system.

Iron exhibits spontaneous magnetization state not only as crystalline element but also as a component of molecules which form crystal (e.g. FeO_4).

Practical application of ferromagnetic materials has made a significant contribution to civilizing evolution of humanity. Particularly there are three fields worth mentioning: (1) generation and distribution electric energy; (2) telecommunications and (3) storing and processing of data (computer science and computerization). In these applications ferromagnetic materials are presented as alloy forms (e.g. Fe-Si), ferrites (e.g. MnO, ZnO, Fe_2O_3) and composites (e.g. epoxide resin Terfenol D that is $Tb_{0.3}Dy_{0.7}F_{1.9}$) [e.g. 12–23].

3.2. FERROELECTRIC MATERIALS

Similarly, to ferromagnetic materials, there are a lot of monographs and books about ferroelectric materials [e.i. 5, 6, 8], therefore the information contained in this article would be concerning just the place of ferroelectric materials in crystalline family.

The crystallography basis shows that each crystal could be ascribed to one of the 32 crystallographic groups (points groups), according to symmetry elements of crystal [28]. Analysis of 32 symmetry classes points out that 11 of them (with abridged international symbols: 1, *4/m*, *4/mm*, *6/m*, *6/mm*, *2/m*, *mmm*, $\bar{3}$, $\bar{3}m$, *m*3, *m*3*m*) are distinguished by centre of symmetry presence (Table 1). Those crystals are named as centrosymmetric. The *centrosymmetric* crystal due to electrical properties is defined as non-polar. If homogenous mechanical strain is applied to that kind of crystal then small shift of charges in crystalline lattice comes out. On account of centrosymmetric presence the individual displacements are compensated. If electric field is applied to centrosymmetric crystal then it generates crystal deformation, which does not change after sign change of applied field [30]. This deformation is proportional to square of applied field; it is named square effect or *electrostriction*. This effect can appear in dielectric crystalline and amorphous materials as well as in solid or liquid. Electrical crystal properties are strictly connected to their symmetry. Special role plays the character of electrical charges distribution in crystalline lattice. Different variants of those distributions can be observed depending on crystal symmetry. In case of centrosymmetric crystals the distribution of positive and negative charges is also centrosymmetric and centers of symmetry of each sign charges overlap. In one elementary cell dimension that kind of correspondence means that centers of symmetry of charges are covered with centers of symmetry at the same time. Therefore the crystals, which exhibit centrosymmetric charges distribution, are named *non-polar*.

The rest of 21 crystallographic classes, which form non - centric crystal classes, do not have center of symmetry. Because of lack of symmetry center, all the non – centre-symmetric crystals classes, except for *423* class, exhibit piezoelectric effect. Crystals of *432* = 0 = $L_z^4 L_y^4$ class (pentagonal triooctahedron), which belong to cubic configuration do not have center of symmetry, however the symmetry they have excludes possibility of piezoelectric effect appearance. Therefore piezoelectric effect exhibits crystals which belong to 20 non-centric crystal classes. It means that after mechanical stress is applied the polar state in crystal is arisen (or change is sustained). Piezoelectric effect is a linear effect and could be as well direct $\boldsymbol{P}_i = \boldsymbol{d}_{ij}\boldsymbol{\sigma}_{ij}$, as inverse $\boldsymbol{\eta}_j = \boldsymbol{d}_{ij}\boldsymbol{E}_i$, where: $\boldsymbol{P}_i$ – polarization, $\boldsymbol{d}_{ij}$ – tensor of piezoelectric modules, $\boldsymbol{\sigma}_{ij}$ – mechanical stress tensor, $\boldsymbol{\eta}_j$ – deformation tensor, $\boldsymbol{E}_i$ – electric field intensity. The values of $\boldsymbol{d}_{ij}$ create third row tensor. The number of piezoelectric modules, which are necessary to determine piezoelectric properties of crystal, is dependent on symmetry class. This matter could be solved with Neumann [37] principle help or easier with help of Voigt [38] principle, which springs from Neumann principle. The most useful to settlement of independent components tensor's $\boldsymbol{d}_{ij}$ number depending on symmetry class of crystal, the groups theory turned out [31]. Precise discussion of the problem could be found in references [32, 37].

From 20 piezoelectric classes of crystals only 10 (*1,2,m,2mm,4,4mm,3,3m,6,6mm*) have the polar axis, such as:

a) in their positive and negative direction crystal exhibits different properties,
b) they could not have crystallographic equivalent axis.

Crystals of those 10 polar classes are spontaneously polarized and values of their spontaneous polarization ($\boldsymbol{P}_S$) depend on crystal temperature according to formula: $\Delta\boldsymbol{P}_s = \gamma p^{\sigma}\Delta T$, where: $\Delta\boldsymbol{Ps}$ – change of spontaneous polarization vector, ΔT – change of temperature, γ_p^{σ} – pyroelectric coefficient (polar vector). This effect is called pyroelectric effect, while crystals which exhibit these properties are called pyroelectrics.

In polar crystals family (pyroelectric) *ferroelectric materials* take up a special place. These are materials which characterize among others: high values of spontaneous polarization and electric permittivity, domain structure, non-linear and electro-optic properties. Necessary condition for crystal to be ferroelectric material is its adjunction to one of the *10 polar symmetry classes*. However this requirement is not sufficient. According to many authors [e.g. 33, 34] as ferroelectric is considered pyroelectric crystal with *reversible spontaneous polarization* in external electric field (repolarization effects or switching polarization). Crystallographic criterion is not enough for describing ferroelectric state, because all ferroelectric materials are pyroelectric materials, but not all pyroelectric materials are ferroelectric materials. Indispensable are additional experimental criterions. One of them, very essential, is reversibility spontaneous polarization in external field and connected with this *dielectric hysteresis*. Equally important experimental criterion is the presence of domain structure, electric permittivity peak in Curie temperature (T_C), and modifications of dielectric properties above T_C, as a result of phase transition.

Table 1

Place of ferroelectric materials in crystals family [30]

Symmetry classes	No class	Symbols			Centro-symmetric crystals	No – centric crystal classes		
		Krentz	Schoenflies	International		Piezoelectrics	Piroelectrics	Polar neutral crystals
Triclinic	1	L^1	C_1	1	–	x	x	–
	2	C	C_i	$\bar{1}$	x	–	–	–
Monoclinic	3	L_y^2	C_2	2	–	x	x	–
	4	P_y	C_s	m	–	x	x	–
	5	L_y^2C	C_{2h}	$2/m$	x	–	–	–
Orthorhombic	6	$L_x^2P_y$	C_{2v}	$2mm$	–	x	x	–
	7	$L_x^2L_y^2$	D_2	222	–	x	–	x
	8	$L_z^2L_y^2C$	D_{2h}	mmm	x	–	–	–
Tetragonal	9	A_z^4	$_4$	$\bar{4}$	–	x	–	x
	10	L_z^4	C_4	4	–	x	x	–
	11	L_z^4C	D_{4h}	$4/m$	x	–	–	–
	12	$A_z^4L_y^2$	D_{2d}	$\bar{4}2m$	–	x	–	x
	13	$L_z^4P_y$	C_{4v}	$\bar{4}mm$	–	x	x	–
	14	$L_z^4L_y^2$	D_4	422	–	x	–	x
	15	$L_z^4L_y^2C$	D_{4h}	$4/mmm$	x	–	–	–
Trigonal	16	L_z^3	C_3	3	–	x	x	–
	17	L_z^3C	S_6/C_{3i}	$\bar{3}$	x	–	–	–
	18	$L_z^3P_y$	C_{3v}	$3m$	–	x	x	–
	19	$L_z^3L_y^2$	D_3	322	–	x	–	x
	20	$L_z^3L_y^2C$	D_{3d}	$\bar{3}m$	x	–	–	–
Hexagonal	21	$L_z^3P_z$	C_{3h}	$\bar{6}$	–	x	–	x
	22	$L_z^3L_y^2P_z$	D_{3h}	$\bar{6}m2$	–	x	–	x
	23	L_z^6	C_6	6	–	x	x	–
	24	L_z^6C	C_{6h}	$6/m$	x	–	–	–
	25	$L_z^6P_y$	C_{6v}	$6mm$	–	x	x	–
	26	$L_z^6L_y^2$	D_6	622	–	x	–	x
	27	$L_z^6L_y^2C$	D_{6h}	$6/mmm$	x		–	–
Cubic	28	$L_1^3L_2^3$	T	23	–	x	–	x
	29	$L_1^3L_2^3C$	T_h	$m3$	x	–	–	–
	30	$A_z^4A_y^4$	T_d	$\bar{4}3m$	–	x	–	x
	31	$L_z^4L_y^4$	O	432	–	–	–	x
	32	$L_z^4L_y^4C$	O_h	$m3m$	x	–	–	–
The sum total					–	20	–	–
					11	–	10	11
					32			

Ferroelectric materials are part of polar crystals subgroup that is pyroelectric crystals. Each of ferroelectric structure could be ascribed as weak deformed, suitably non-polar structure, which exhibits above Curie temperature (T_C). Regardless some deficiency of the statement, it would be accepted as basis of ferroelectric definition. Some materials ($BaTiO_3$, $NaNbO_3$, etc.), in specified temperature rages, have different ferroelectric structures. I.S. Zheludev and L.A. Shuvalov [35] showed that in similar cases each of ferroelectric structures does not relate to the nearest (on account of temperature) crystal phase but to its non-ferroelectric phase. Each of ferroelectric phases (e.g. in $BaTiO_3$ case: tetragonal *4mm*, orthorhombic *2mm* and rhombohedral *3m*) presents slightly distorted structure of non-ferroelectric phase (paraelectric phase, non-polar); in $BaTiO_3$ case – regular phase *m3m* (above T_C = 393 K). Possible directions of spontaneous polarization are determined not by given or next ferroelectric phase symmetry but symmetry of initial non-ferroelectric (prototype) phase, spontaneously deform during phase transformation.

Changes of external conditions could alter the crystal symmetry. Comparing to the polar class symmetry, the non-polar class symmetry – in general – is higher. Knowing crystallographic class only, it is impossible to show, which of piezoelectric materials could be repolarized and finally which of them is ferroelectric material. *However if after change of external condition (temperature, electric field, mechanical stress) the pyroelectric material could change from polar to class with higher symmetry, it is possible to say, that in polar phase it is the ferroelectric material* [31].

The searching problems with ferroelectrics could be divided into three groups: mono-domains crystal properties, polydomains crystal properties and polycrystals ceramic materials properties. In investigations concerning problems of second and third group as a point of reference the results of monodomains crystal investigations are always accepted. Special meaning have also investigations of *domain structure in equilibrium state*, i.e. structure, which is taken by isolated ferroelectric crystal, when whole energy of crystal gets minimal value. About properties of given ferroelectric material with domain structure in equilibrium state, decide first of all the crystalline structure and dynamical properties of crystalline lattice [36]. Ferroelectric state appears in crystal as a result of phase transformation and it often combines with low-temperature phase ($T < T_C$). Simplifying, it could be accepted that below Curie temperature energy of dipole interaction exceeds the value of elastic energy, which is requisite to dipoles moment creation and then crystal spontaneously polarizes. Finding the connection of spontaneous polarization with crystal structure and dynamical properties of its crystalline lattice is very difficult and not completely understood till now. In case of crystals with domain structure in equilibrium state there were found a lot of regularity in common relation: ferroelectric state – crystal structure. It mainly concerns the determination of symmetry crystals classes where ferroelectric state could appear, direct relation of low-temperature symmetry phase to high-temperature symmetry phase and dependence of many ferroelectric materials properties on their symmetry classes in high-temperature phase, particularly dependence between domain structure, direction of spontaneous polarization appearance and low and high-temperature symmetry.

Ferroelectric materials create today a tremendous monocrystals family with different structure types and even bigger group of ceramic materials.

3.3. FERROELASTIC MATERIALS

Ferroelasticity (FES) is mechanical (elastic, springy) analogue of *ferromagneticity* (FM) and *ferroelectricity* (FE). By analogy it is easy to define and understand such notions, which are connected with ferroelastic materials, as paraelastic, antyferroelastic, spontaneous deformation, ferroelastic hysteresis loop, coercive stress, ferroelastic domains, ferroelastic phase transition (ferroelastic FES – paraelastic PES).

Ferroelastic crystal, in absence of external mechanical stress, has two or more stable orientation states where it is not strained. In ferroelastic materials the reversible transformation from one to the other state is possible as a result of applying the external mechanical stress in specified direction. Any of two orientation states in ferroelastic crystal are identical for structural reason (enantiomorphism) but they are different in tensor of mechanical deformation in absence of external stress.

Therefore ferroelastic material is a crystal where spontaneous deformation could be switched by applying external mechanical stress (Fig. 3).

Ferroelastic crystals exhibit spontaneous deformation (directional deformation) of crystalline lattice, with accompany of domains structure. As a consequence the hysteresis is observed, where the volumetric total spontaneous deformation (η_s) changes in a function of mechanical directional stress appliance (σ).

Ferroelectricity issue appeared in 1950's in investigations of high-elastic alloys Au-Cd and In-Ti so in metallurgy.

In physics ferroelasticity: 1) proper and 2) improper are distinguished.

Proper ferroelasticity is an independent property of solid state, occurring there apart from other properties (ferromagneticity or ferroelectricity). This kind of ferroelasticity has been observed in metals and non-defected alloys, which were free from any defects (also hydrogen admixture) [10]. The proper ferroelectricity term is known not very well, often incomprehensible in proper way. Imagine that square or cube, which undergos *spontaneous distortion*, (spontaneous deformation) during absence of mechanical external stresses and changed in rectangle or regular rectangular prism, respectively. In three-dimensional case after spontaneous deformation one of the edges of rectangular prism is a bit longer then edge of initial cube, while two of the others are a bit shorter then edges of cube. Spontaneous deformation of cube to rectangular prism could appear with the same probability in three different directions, which are perpendicular one to another. In other words, longer edge of rectangular prism could take the one of the three perpendicular directions (three deformation states without internal stress). Clenching stress with proper value applied along longer edge generates switching to the other alternative state, when one of the two remaining edges gets longer (dependence of deformation from stress has *hysteresis character*). Materials, where such effect could appear are named as proper ferroelastic materials.

Improper ferroelasticity is ferroelasticity, which is accompanied with ferromagneticity and/or ferroelectricity, more or less coupled with it. Materials, where ferroelasticity appears in connection with ferromagneticity, are called *ferromagnetoelastic materials or ferroelastomagnetic materials* (FE+FES), whereas materials, where ferroelasticity appears together with ferroelectricity are called *ferroelectroelastic materials* or *ferroelastoelectric materials* (FE+FES).

Materials, which exhibit at the same time two ferroic states e.g. ferroelectric state (FE) and ferroelastic state (FES), ferroelectric state (FE) and ferromagnetic state (FM) or ferroelastic state (FES) and ferromagnetic state (FM) are called *biferroic materials*.

In biferroic materials the stress state among ordered subsystems (magnetic, electric or elastic) could be different and could include: (1) complete coupling, (2) partial coupling or (3) uncoupled.

That problem will be illustrated on example of selected ferroelastoelectric materials.

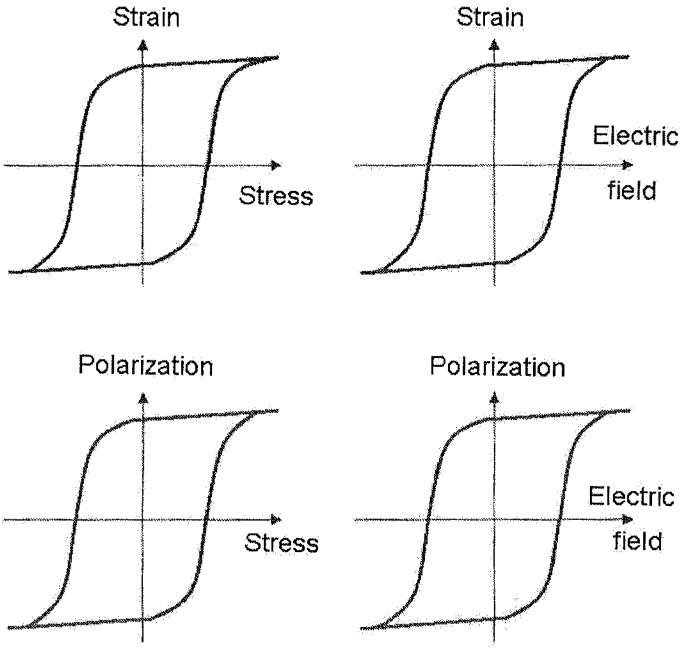

Fig. 5. Four hysteresis cycles in biferroic materials with complete coupling ferroelectric phase (FE) and ferroelastic phase (FES) in $T < T_{CE}$ (e.g. in $BaTiO_3$ and $Na_5W_3O_9F_5$): η – deformation; σ – mechanical stress; P – polarization; E – electric field intensity [11]

Proper ferroelastic materials are not the polar crystals (do not exhibit spontaneously polarize state), while in improper ferroelastic materials case, that is biferroic materials (e.g. ferroelastoelectric materials) smaller or bigger coupling between ferroelectric and ferroelastic properties could appear. One of the symptoms of this kind of coupling is simultaneous (in the same temperature T_{CE}) appearance of transition of low-temperature ($T < T_{CE}$) ferroelectric phase (FE) and ferroelastic phase (FES) in high-temperature ($T > T_{CE}$) paraelectric phase (PE) and paraelastic phase (PES). In *strong coupling case* of FE and FES phases the spontaneous polarization (P_S) could be modified as well with electric field (E) help as properly oriented mechanical external stress (σ) help, whereas deformation (η_s) could be changed not only with properly oriented mechanical external stress (σ) but also with electric external field (E). As a consequence in such ferroelastoelectric materials there could be observed four hysteresis cycles: (1) $\eta - \sigma$; (2) $\eta - E$; (3) $P - \sigma$; (4) $P - E$ (Fig. 5).

During ferroelastoelectric crystals growth the ferroelectric or/and ferroelastic domain structure is formed. In absence of coupling FE-FES the polydomains ferroelastic crystal could be changed in monodomains state through mechanical external stress (σ) operating, while ferroelectric crystal with help of electric external field (E). If in ferroelastoelectric materials the strong coupling FE-FES appears, the monodomenization process becomes more effective, because simultaneously could affect crystal with electric field (E) or mechanical stress (σ). First tests were made on $Na_5W_3O_9F_5$ example [39].

The example of ferroelastoelectric materials with complete coupling FE and FES phase are $K_3\ (Fe_3^{2+}Fe_2^{3+})F_{15}$ and $Gd_2(MoO_4)_3$, with partial coupling - $Pb_2KNb_5O_{15}$ and uncoupled - $Ba_4Na_2Nb_{10}O_{30}$, and $Pb_5(Cr_{1-x}Al_x)_3F_{19}$.

- **BaTiO₃** (complete coupling of FE-FES subsystems)

Barium titanate is model of ferroelastoelectric material with complete coupling of FE-FES phases. It has the *perovskite type* ABO_3 (Fig. 6) crystalline structure and it is the oxygen-octahedron ferroelectric material with phase transformation of displacement type. In $BaTiO_3$ crystalline lattice the big ions of Ba^{2+} in bends with coordination 12 are surrounded by oxygen regular octahedron TiO_6, where on centre the small ion of Ti^{4+} occurs. The prototypal crystalline phase is cubic phase (*m3m*), which appears above ferroelectric Curie point ($T_{CE} \approx 393$ K).

During cooling process the crystallographic distortion is in T_C and then the crystal $BaTiO_3$ transits to ferroelectric and simultaneously to ferroelastic tetragonal phase (*4mm*). During further cooling in $T_{p1} = 278$ K, the phase transformation *4mm→mm2* appears, which causes forming of the orthorhombic phase (FE-FES) and in $T_{p2} = 183$ K the transformation *mm2→3m* follows and the rhombohedral ferroelectric also ferroelastic phase appears (Fig. 7).

All of mentioned structure transitions are first type of phase transitions. During next phase transitions the spatial orientation of spontaneous polarization vector ($\boldsymbol{P_S}$) changes. In tetragonal phase this vector is parallel to $[100]_c$ direction of prototype cubic cell in $T > T_C$, in orthorhombic phase it is parallel to $[110]_c$, and in rhombohedral phase to $[111]_c$. The direction of $\boldsymbol{P_S}$ vector is always compatible with the direction of spontaneous deformation prototype's elementary cell. Therefore in $BaTiO_3$ occurs

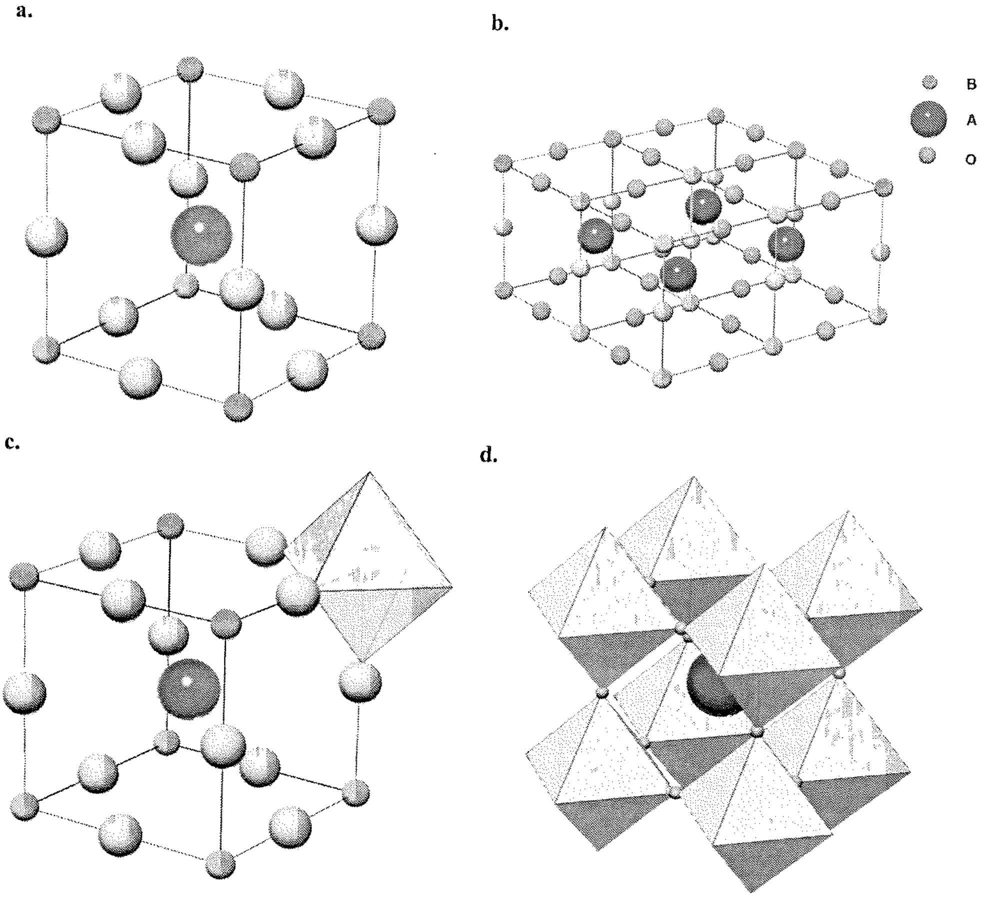

Fig. 6. Structure of perovskite type ABO_3

the complete coupling of electric (FE) and elastic (FES) subsystems during phase transformation:

$$\begin{array}{ccccccc} & T_c & & T_{p1} & & T_{p2} & \\ m3m & \rightarrow & 4mm & \rightarrow & mm2 & \rightarrow & 3m \\ \mathrm{PE} & & \mathrm{FE} & & \mathrm{FE} & & \mathrm{FE} \\ \mathrm{PES} & & \mathrm{FES} & & \mathrm{FES} & & \mathrm{FES} \end{array} \qquad (1)$$

The number of stable deformation and polar states is different in each of the three phases (e.g. in *4mm* phase occur 3 different stable elastic states but 6 different stable polar states).

Replacement in $BaTiO_3$ in Ba^{2+} place the Ca^{2+} or Sr^{2+} ions slightly modifies the temperatures of transitions (T_C, T_{p1}, T_{p2}) but does not influent their kind and order. Whereas replacement of Pb^{2+} – Ba^{2+} (with amount 20at%) causes the decay of low-temperatures phase transitions in T_{p1} and T_{p2}, and stays only in the transition *m3m*→*4mm* in T_C. The progressive substitution of Ti^{4+} with considerable bigger Zr^{4+}

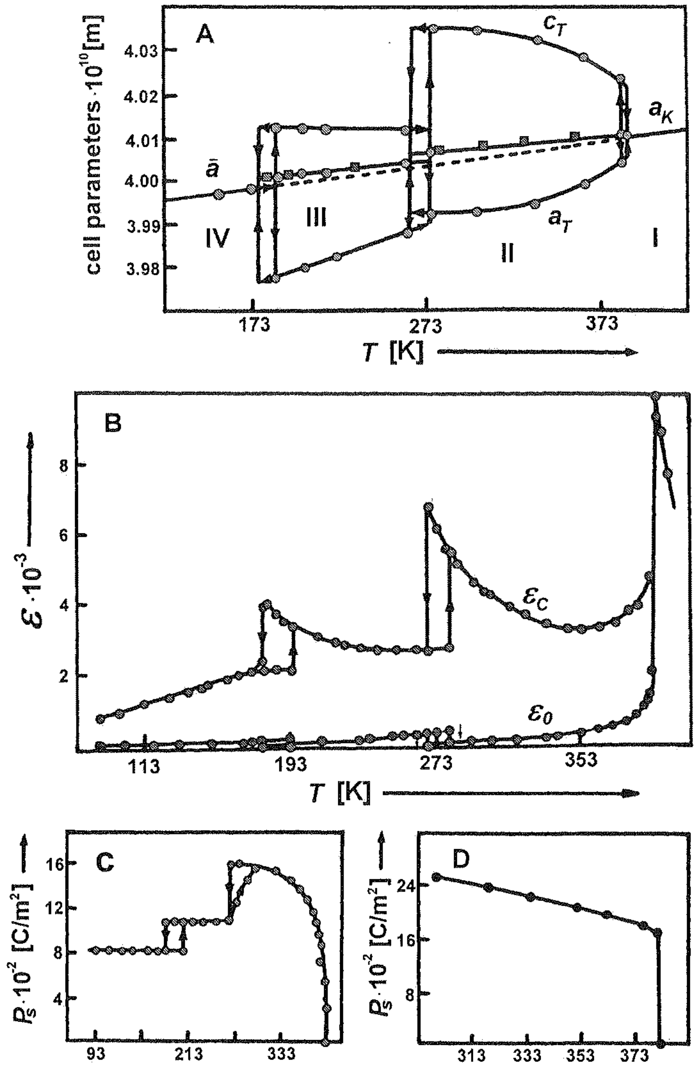

Fig. 7. The structural phase transition in $BaTiO_3$ and their influence on $\varepsilon(T)$ and $P_S(T)$ changes: A: I – cubic phase (*Pm3m*), II tetragonal phase (*P4mm*), III – orthorhombic phase (*Amm2*), IV – rhombohedral phase (*R3m*); B: The values of ε_0 and ε_C for mono-domains crystal; C, D: P_S – measured along pseudo-regular direction [*100*]; The leap of P_S in T_C occurs only in crystals with high quality (D)

ions causes the decay of tetragonal and orthorhombic distortion and leads to appearance just one phase transition *m3m*Ⓣ*3m*. In all mentioned cases the substitutions of Ba^{2+} and Ti^{4+} do not influence on coupling of Fe-FES systems.

- **$K_3(Fe_3^{2+}Fe_2^{3+})F_{15}$** (complete coupling of FE-FES subsystems)

These fluorite posses *the structure of tetragonal tungsten bronze* (TBW) and in *mm2* phase there is the ferroelectric material with order-disorder type. This means that in PE phase the ions are random arranged in proper positions, while in FE phase the ions are preferentialy arranged in some of these positions, which leads to forming of the local P_S. In polar phase the Fe ions with changeable valence (Fe^{2+} and Fe^{3+}) are arranged in non-equivalently octahedral positions as a result of displacement along polar axis (Oz). The phase transitions PE – FE leads to orthorhombic distortion with 2 deformation states and corralled with them 2 polarization states. Transition from one deformation state to the other (inversion of the Ox and Oy axis), leads to change of P_S direction according to Oz axis at the same time. FE and FES subsystems are completely coupled so in Curie point one phase transition follows [40]:

$$\begin{array}{ccc} & T_c & \\ 4/mm & \rightarrow & mm2 \\ \text{PE} & & \text{FE} \\ \text{PES} & & \text{FES} \end{array} \tag{2}$$

- **$Gd_2(MoO_4)_3$** (complete coupling of FE-FES subsystems)

Gadolinium molybdate (GMO) is a leading ferroelastoelectric material that belongs to $R_2(MoO_4)_3$ family, where R represents elements of rare earths, e.g. Sm, Cd, En, Tb etc. [4]. Ferroelectric properties along with ferroelastic properties exhibit just the β gadolinium molybdate phase (β-GMO). The Curie temperature of β-GMO is T_{CE} = 436 K. The first kind of phase transformation appears in this temperature.

$$\begin{array}{ccc} & T_c & \\ \bar{4}2/m & \rightarrow & mm2 \\ \text{PE} & & \text{FE} \\ \text{PES} & & \text{FES} \end{array} \tag{3}$$

In $T < T_{CE}$ the two polar states $\pm \boldsymbol{P_S}$ are observed, they can be shifted with external electric field help ($E_C \approx$ 1,4 kV/cm). Those two kinds of polar states $\pm \boldsymbol{P_S}$ are coupled with two mechanical configurations described by two deformations at shearing $\pm \boldsymbol{x}_{XY}$. Both mechanical states could be reversed by external mechanical stress. Because of strong FE-FES coupling the parameters of $\boldsymbol{P_S}$ and $\boldsymbol{x}_{XY}$ change simultaneously and both could be shifted with external electric field (E) help as well as mechanical stress (σ) help [42].

In ferroelectric state ($T < T_{CE}$) the elementary cell of β-GMO includes four molecular units. In $T > T_{CE}$ temperature (at paraelectric state) the volume of elementary cell reduces by half in relation to volume in $T < T_{CE}$. Crystal stops being ferroelectric but keeps piezoelectric properties. In β-GMO structure there can be distinguished three different tetrahedral cells $(MoO_4)_{2-}$ situated successively along *c* axis with type ordering as layer by layer (Fig.8).

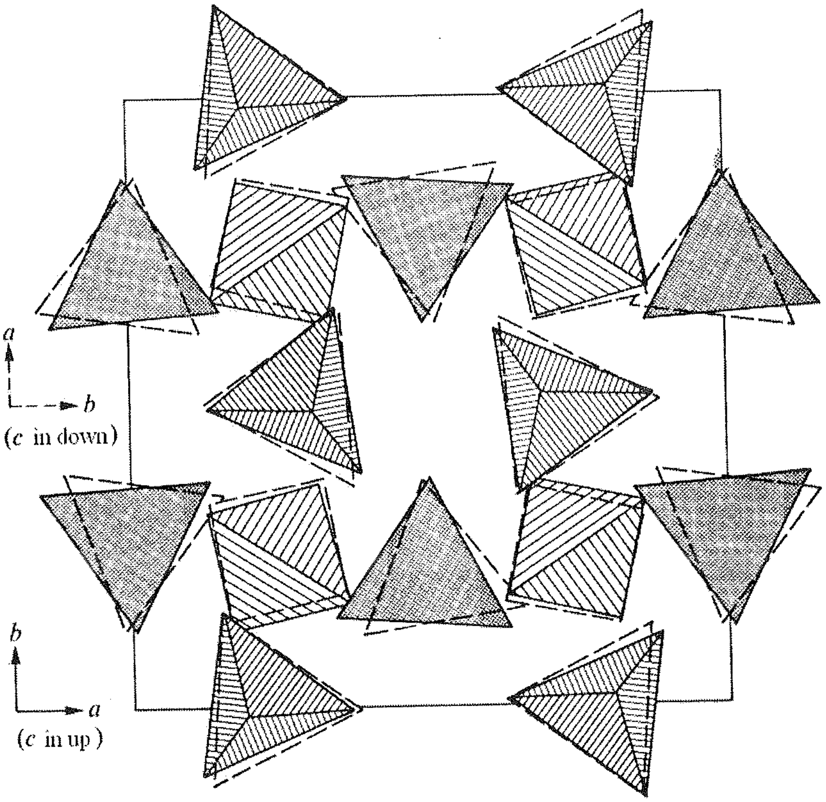

Fig. 8. Projection of β-GMO structure on (*001*) plane; Dashed and continuous lines represent accordingly two types of ferroelectric –ferroelastic structures [43]

If in orthorhombic state ($T < T_{CE}$) the pressing stress along *b* axis is applied to the crystal then the *a* and *b* axes mutually exchange and electric dipoles are shifted. In fact the difference between *a* and *b* axes in orthorhombic phase is not big (about 0.3%). Dashed and continuous lines in Fig. 8 represent small movements of tetrahedrons $(MoO_4)^{2+}$ suitable before and after switching.

At schematic diagram (Fig. 9) two possible configurations of β-GMO are presented, in paraelectric state ($T > T_{CE}$). Continuous lines show the view of elementary cell in paraelectric phase on XY plane and dashed lines – the view of elementary cell in ferroelectric phase. The "+" and "-" signs indicate the direction of $\boldsymbol{P_S}$ along *c* axis.

- **$Pb_4K_2Nb_{10}O_{30}$** (partial coupling of FE-FES subsystems)

This crystal possesses *the structure of tetragonal tungsten bronze* (TBW). Anisotropic nature of free electron couple of Pb^{2+} cation leads to orientation of $\boldsymbol{P_S}$ according to Oy axis. In this way the *b* parameter of crystalline lattice becomes bigger then *a*

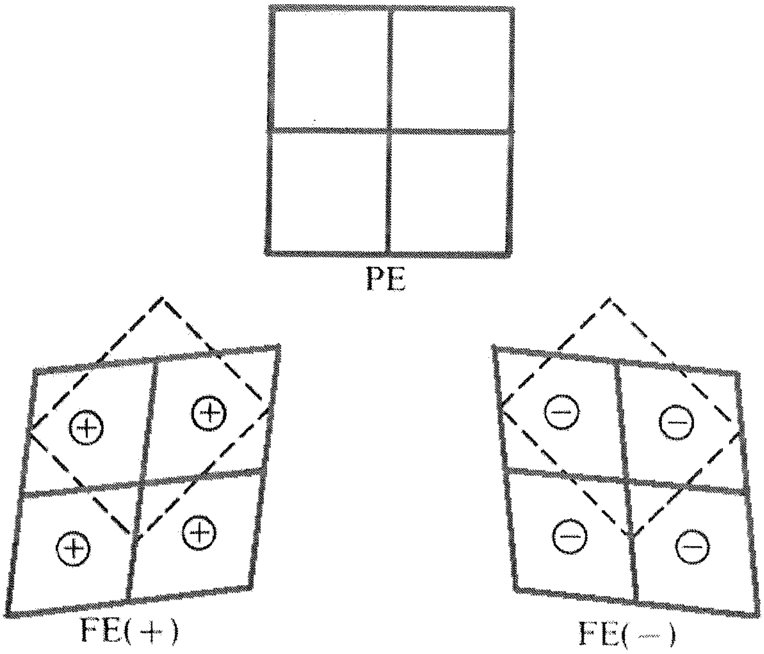

Fig. 9. Scheme of paraelectric and ferroelectric elementary cells in β-GMO crystal [30]

parameter. Crystal in *m2m* phase possesses 6 stable states: 2 deformation states and 4 polar states. The direction of spontaneous polarization $\boldsymbol{P_S}$ could be reversed (switched) with external electric field help (E) but it does not cause the change of state in ferroelastic subsystem (lack of the FE-FES coupling). E field as well as stress σ(apply along Ox axis) could cause rotation of $\boldsymbol{P_S}$ over 90° (from Oy to Ox) what leads to new stable state. Therefore the external mechanical stress could change the orientation of $\boldsymbol{P_S}$, but could not cause the change of its turn to the opposite, i.e. could not switch $\boldsymbol{P_S}$. This proofs partial coupling of FE-FES subsystems only. In ferroelastoelectric material $Pb_4K_2Nb_{10}O_{30}$ only one common phase transition [44] appears:

$$\begin{array}{ccc} & T_c & \\ 4/mm & \longrightarrow & mm2 \\ \mathrm{PE} & & \mathrm{FE} \\ \mathrm{PES} & & \mathrm{FES} \end{array} \qquad (4)$$

- **$Ba_4Na_2Nb_{10}O_{30}$** (uncoupled FE-FES)

This crystal also possesses the structure of TBW type. The prototype phase in it, is the tetragonal phase (*4/mmm*), while ferroelectric phase is orthorhombic phase (*mm2*). Crystal possesses 4 stable states: 2 deformation states and 2 independent polar states (polar axis is the same as Oz axis). External mechanical stress (σ) or electric field (E) causes respectively just the change in deformation value (η) or polarization value

($\boldsymbol{P_S}$), according to their tensors nature (lack of the FE-FES coupling). In the crystal two independent phase transitions [45] occur:

$$\begin{array}{ccccc} & T_c & & T_{pl} & \\ 4/mm & \rightarrow & 4mm & \rightarrow & mm2 \\ \text{PE} & & \text{FE} & & \text{FE} \\ \text{PES} & & \text{PES} & & \text{FES} \end{array} \tag{5}$$

- **$Pb_5(Cr_{1-x}Al_x)_3F_{19}$** (uncoupled FE-FES)

The phase diagram of that type of solid solution (1-x)$Pb_5Cr_3F_{19}$ – (x) $Pb_5Al_3F_{19}$ is shown in Fig. 10. It means that in solid state three characteristic regions for (1) x = 0; (2) x = 1 and (3) x = 0,96 appear [46, 47].

(1) **$Pb_5Cr_3F_{19}$** (x=0)

This relation does not exhibit the ferroelastic properties and as result of phase transition just the ferroelectric state occurs (Fig. 10):

$$\begin{array}{ccc} & T_c & \\ 4/mm & \rightarrow & mm2 \\ \text{PE} & & \text{FE} \end{array} \tag{6}$$

(2) **$Pb_5Al_3F_{19}$** (x=1)

Due to replacement in $Pb_5(Cr_{1-x}Al_x)_3F_{19}$ the bigger Cr^{3+} ions with the smaller Al^{3+} ions, with connection to free electron couple of Pb^{2+} ions, the new polar and distortion states are formed. Between paraelectric state (I) and ferroelectric state (V), during temperature increase, the new intermediate phases appear (Fig.10): II (paraelastic phase), III (ferroelastic phase), and IV (antiferroelectric phase).

In ferroelastoelectric material $Pb_5Al_3F_{19}$ the following phase transitions occurs proving that FE-FES subsystems are uncoupled:

$$\begin{array}{ccccc} \text{I}(4/mm)- & \text{II}(4/m)- & \text{III}(2/m)- & \text{IV}(4/m)- & \text{V}(4mm) \\ \text{PE} & \text{PES} & \text{FES} & \text{AFE} & \text{FE} \end{array} \tag{7}$$

(3) **$Pb_5(Cr_{0,04}Al_{0,96})_3$** (x=0,96)

In case of small concentration of Cr^{3+} cations with bigger ionic ray then Al^{3+} cations the antiferroelectric phase (IV) disappear in the room temperature (T_r = 293 K) and just three phase transitions stay:

$$\begin{array}{cccc} I(4/mm)- & II(4/m)- & III(2/m)- & V(4mm) \\ PE & PES & FES & FE \end{array} \tag{8}$$

The FE and FES subsystems remain still uncoupled.

The investigations of *proper* (intrinsic) *ferroelastics* are relatively poorly advanced, it concerns experimental and theoretical investigations as well as applied investigations. The important achievement of these investigations, which allows to understand and describe the physical nature of PES-FES phase transformation, is relating it on the

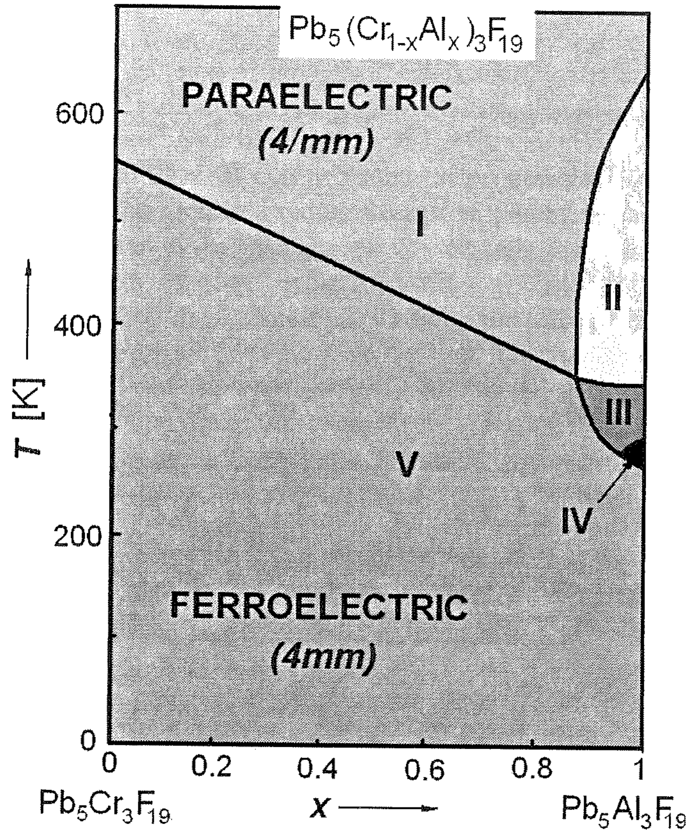

Fig. 10. Phase diagram of ferroelastoelectric material $Pb_5(Cr_{1-x}Al_x)_3F_{19}$ [46, 47]:

I – tetragonal (*4/mm*) paraelectric phase (PE);
II – tetragonal (*4/m*) paraelastic phase (PES);
III – monoclinic (*2/m*) ferroelastic phase (FES);
IV – tetragonal (*4/m*) antiferroelectric phase (AFE);
V – tetragonal (*4mm*) ferroelectric phase (FE)

ground of lattice dynamics with *soften effect* of elongated acoustic phonons in surrounding temperature of phase transition. For that reason, by the analogue to ferroelectric materials the term of *ferroelastic soft* (low-frequency) *mode* was introduced [29].

The investigation state of *improper* (nonintrinsic) *ferroelastic materials*, including ferroelastoelectric materials, shows much better. *The ferroelastoelectric state is there a result of mutual influence of spontaneous deformation in crystalline lattice with initial ordering parameter of electrical subsystem that is a spontaneous polarization.* As a consequence the ferroelectric and ferroelastic properties are more or less coupled.

4. SUMMARY

Research of the ferroic materials carried out in complex way (Fig. 11) i.e. with varied research methods help, with participation of specialists from different disciplines (physicists, chemist, computer scientists, technologists, electronics engineers, engineers etc.), taking wide ferroic range into consideration (FE, AFE, FIE, FM, AFM, FIM, FES, AFES etc.), continuously brings the important input in different types of smart structure development.

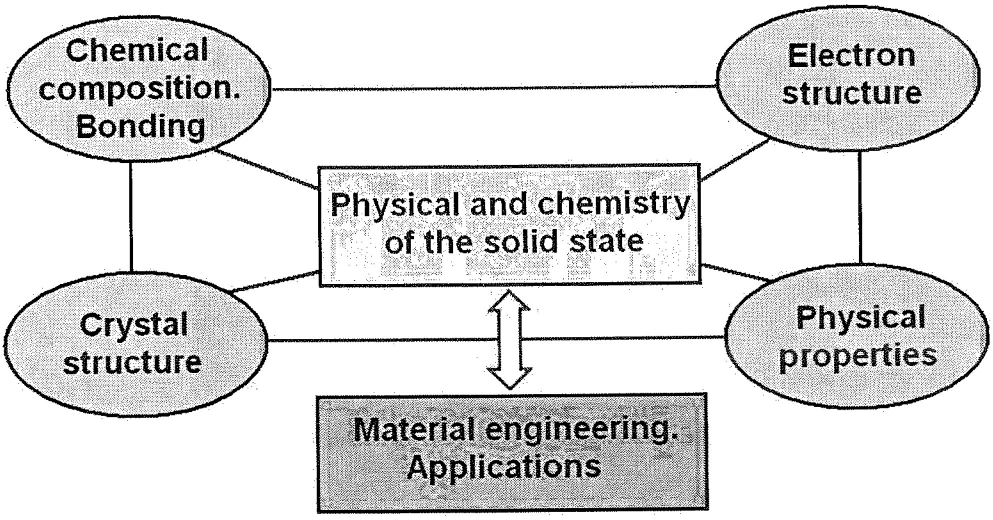

Fig. 11. Range of integration in ferroic smart materials investigations [11]

The new materials are searched for but first of all, the improvement of the production technology of ferroic materials, which are already known due to improvement of their level of perfection of crystalline structure, chemical and physical homogeneous etc. The electronic smart structure based on ferroic materials should by characterized not only by strong and quick reaction to the external stimuli but simultaneously by reaction to stimulus, which is weakly developed. The world of smart structure is not the word of gigavolts or gigapascals but the world of nanovolts and nanopascals.

The huge value of ferroic materials is that their defining property it is in precise connection to the other also essential properties for smart structure. For example, ferroelectrics always exhibit strong piezoelectric and pyroelectric properties. There are well – known dielectric ferroelectrics but also semiconducting ferroelectrics. During temperature increase the specific electrical resistance usually decreases (ferroelectric resistors with NTC-R effect) but there are also the ferroelectrics with posistor properties where the electric resistance increases with the temperature increase (PTC-R effect). Transparent crystals, ceramic materials, thin layers and ferroelectric fibres characterized by optical birefringence and electrooptical properties (quadratic Kerrs effect, linear

Pockels effect, electooptical memory). Depending on intensity of the external stimuli and work temperature the ferroelectric elements could exhibit linear or non-linear properties. These which are heated up above Curie point (T_{CE}) get the new properties, typical for paraelectric state. Similar integration of many varied properties could also take place in ferromagnetic materials.

The region of ferroic materials investigation includes also the problem of properties changes by chemical composition, crystalline structure, electron structure, domain structure modifications and in the case of ceramic materials also microstructures (grain size distribution).

Parallel with works of the technological nature and experimental investigations the theoretical works concerning ferroic state develop. They concern especially phase transitions, the problem of spontaneous ordering of electric, magnetic and elastic systems and also the connection of the observed effects in ferroic materials with dynamics of crystalline network, quantum physics and quantum chemistry etc.

The family of equipment, which contains smart ferroic elements, is really reach and includes different applications and industrial fields (automatics, robotics, control of the producing process, technology of materials, aerospace engineering, automotive industry, defense technology, medical technology and biotechnology, computer technology etc.).

On account of mostly popularized character of this article, it would be finished with futuristic vision of artificial intelligence development, which was presented by outstanding scientist Jan Person from British Telecom to editor Paweł Górecki from NEWSWEEK (19.03.2006):

- 2008-2012: the virtual clothes and virtual make-up will be formed, which allows to change the appearance of man in network;
- 2001-2015: the content of dreams will be partly programmable;
- 2013-2017: an excessive appetite will be limited with computer help, which will be connected with brain;
- 2015 : the being with artificial intelligence (SI) and self-consciousness comes into existence;
- 2020 : the being with SI will become the member of parliament and will be gaining the scientific titles;
- 2030 : appear the machines which will fight with people like terminator from the movie;
- 2030 : it will be possible to use network connecting computer directly to human brain;
- 2040 : come into being the implants, thanks to primate animals reach the human intelligence;
- 2075 : we will be able to transfer contents of our brains to network, gaining immortality.

In the other interview I. Person's co-operator and co-originator of present *"Technology Timeline"* I. Neilod on the question if he believes in this futuristic vision said:

"Yes, if the physicists, chemists, engineers, computer scientists, electronic engineers and mathematicians do in that time what they should do in the range of structure and smart materials development".

Futuristic predictions could come true, sooner or later because the issue of Science magazine informs that American scientists built a robot, which recognizes the world latest totally like a baby. H. Lipson from Cornell University said that most of robots are programmed by engineers, while their robot could programme itself. This robot right in its "birth" has known just what it is made of. By experiment it learnt how to walk. When one of his legs was damaged, it reprogrammed itself in that way that it could walk with a limp on three legs. According to Bongard from Vermont University their robot while getting to know the world wonders: "what happen if I do that". It could be said that he has really fragmentary consciousness.

5. ACKNOWLEDGMENT

This article was realized in the frame of research project N507 142 31/3568 financed by MNiSzW.

6. REFERENCES

1. W. Witwicki: *Psychologia* T.II. Warszawa, PWN 1963.
2. P. Guillaume: *Podręcznik psychologii.* Warszawa, PWN 1959.
3. *Encyklopedia Powszechna PWN.* T.2. Red. W. Kryszewski. Warszawa, PWN 1984.
4. A. Lawver: Smart Mater. Bull., 8 (2001) 5-9.
5. Z. Surowiak, V. P. Dudkevich: *Cienkie warstwy ferroelektryczne*, Uniwersytet Śląski, Katowice 1996.
6. *Elektroceramika ferroelektryczna.* Red. Z. Surowiak. Uniwersytet Śląski, Katowice 2004.
7. N. A. Hill: Annu.Rev.Mater.Res., 32 (2002) 1.
8. Z.-G. Ban, S. P. Alpay: Phys.Rev.B., 67 (2003) 184104.
9. V. K. Wadhawan: Resonance, 7, 6 (2002) 91.
10. N. A. Hill, A. Filippeti: J. of Magnetism and Magnetic Materials, 242-245 (2002) 976-979.
11. J. Ravez: C.R. Acad. Sci.Paris, Serie IIc, Chemic/Chemistry, 3 (2002) 267-283.
12. J. Ryn, S. Priya, K. Uchino, H.- E. Kim: J.Electroceram., 8, (2002) 107-119.
13. Y. X. Liu, J. G. Wan, J.-M. Lin, C. W. Nan: J.Appl.Phys., 94, 8 (2003) 5118-5122.
14. T. Ueno, J. Qiu, J. Tani, J. of Magnetizm and Magnetic Materials, 258-259 (2003) 490-492.
15. J. L. Prieto, C. Aroca, P. Sanchez, E. López, M. C. Sanchez: J. of Magnetizm and Magnetic Materials, 174 (1997) 289-294.
16. J. L. Prieto, C. Aroca, E. López, M. C. Sanchez, P. Sanchez: J. of Magnetizm and Magnetic Materials, 215-216 (2000) 756-758.
17. S. B. Kim, K. T. Park, C. S. Kim: J.Appl.Phys., 89, 11 (2001) 7681-7683.
18. H. Tabata, K. Ueda, T. Kawai: Mater.Sci.Eng., B56 (1998) 140-146.
19. A. P. Douvalis, M. Venkatesan, P. Velasco, C. B. Fitzgerald, J. M. D. Coey: J.Appl.Phys., 3, 10 (2003) 8071-8073.
20. J. P. Zhou, R. Dass, H. Q. Yin, J.-S. Zhou, L. Rabenberg, J. B. Goodenough: J.Appl.Phys., 7, 9 (2000) 5037-5039.

21. H. Hauser, G. Stangl, J. Hochreiter: Sensors and Actuators, 81 (2000) 27-31.
22. H. Zheng, J. Wang, S. E. Lofland, Z. Ma, L. Mohaddes-Ardabili, T. Zhao, L. Salamanca-Riba, S. R. Shinde, S. B. Ogale, F. Bai, D. Viehland, Y. Jia, D. G. Schlom, M. Wutling, A. Roytburg, R. Ramesh: Science, 303 (2004) 661-663.
23. T. Wada, Y. Tokunaga, A. Kajima, M. Inoue, T. Fujii, B. Jeyadevan, K. Tohji: Appl.Surface Sci., 113/114 (1997) 212-216.
24. J. S. Kim, C. I. Cheon, P. W. Jang, Y. N. Choi, C. H. Lee: J.Europ.Ceram.Soc., 24 (2004) 1551-1555.
25. M. Mahesh Kumar, V. R. Palkar, K. Srinivas, S. V. Suryanarayana: Appl. Phys.Lett., 76, 19 (2006) 2764-2767.
26. A. Srinivas, M. Mahesh Kumar, S. V. Suryanarayana: Mater.Res.Bull., 34, 6 (1999) 989-996.
27. A. Aizu, J.Phys.Soc.Jpn., 27 (1969) 387.
28. Z. Bojarski, E. Łągiewka: *Materiały do ćwiczeń z rentgenowskiej analizy strukturalnej.* Katowice, Uniwersytet Śląski 1982.
29. Y. Xu: *Ferroelectric materials and their applications*, Amsterdam, Nort-Holland, 1991.
30. M. E. Lines, A. M. Glass: *Principles and application of ferroelectrics and related materials.* Oxford, Clarendon Press 1977.
31. R. Blinc, B. Žekš: *Soft modes in ferroelectrics and antiferroelectrics.* Amsterdam, Nort-Holland Publishing Company 1974.
32. W. G. Cady: *Piezoelectricity.* New York - London, Pergamon Press 1946.
33. J. Burfoot: *Ferroelectrics.* London, University 1967.
34. F. Jona, G. Shirane: *Ferroelectric crystals.*, Oxford, Pergamon Pres 1962.
35. I. S. Zheludev, L. A. Shuvalov: Izv. AN SSSR, Ser.fiz., 21 (1967) 266.
36. A. Jaśkiewicz: *Struktura domenowa ferreoelektryków.* Wrocław, Uniwersytet Wrocławski 1975.
37. J. F. Nye: *Physisal properties of crystals.* Oxford, Claredon Press 1957.
38. W. Voigt: *Lehrbuch der Kristallphysik.* Leipzing, Universität 1928.
39. J. Ravez, M. Laatmani, J. P. Chaminade: Solid State Commun., 32 (1979) 749.
40. J. Ravez, S. C. Abrahams, A. Simon, Y. Calage, R. De Pape: Ferroelectrics, 108 (1990) 91.
41. H. J. Borchard, P. E. Biersted: J.Appl.Phys., 38, (1967) 2057.
42. A. Kumada, H. Yumoto, S. Ashida: J.Phys.Soc.Jpn., 28 (1970) Suppl 351.
43. E. T. Keve, S. C. Abrahams, J. L. Bernstein: J.Chem.Phys., 54 (1971) 3158.
44. J. Ravez, B. Elorsadi: Mater.Res.Bull., 10 (1976) 949.
45. J.-C. Toledano, Ann. Telecom., 29 (1974) 249.
46. J. Ravez, S. C. Abrahams, C. R. Acad. Sci. Paris, serie IIc, Chimie/Chemistry, 1 (1998) 15.
47. J.-M. Reau, M. El Omari, J. Raves: Phase Transition, 69 (1999) 227.

INFORMATION FOR AUTHORS OF E.T.Q.

An article published in other magazines can not be submitted for publishing in E.T.Q. TThe size of an article can not exceed 30 pages, 1800 character each, including figures and tables.

Basic requirements

The article should be submitted to the editorial stuff as a one side, clear, black and white computer printout in two copies. The article should be prepared in English. Floppy disc with an electronic version of the article should be enclosed. Preferred wordprocessors: WORD 6 or 8.

Layout of the article.

- Title.
- Author (first name and surname of author/authors).
- Workplace (institution, adress and e-mail).
- Concise summary in a language article is prepared in (with keywords).
- Main text with following layout:
  - Introduction
  - Theory (if applicable)
  - Numerical results (if applicable)
  - Paragraph 1
  - Paragraph 2
  - ....
  - ....
  - Conclusions
  - Acknowledgements (if applicable)
  - References
- Summary in additional language:
  - Author (firs name initials and surname)
  - Title (in Polish, if article was prepared in English)
  - Extensive summary, hawever not exceeching 3600 characters (along with keywords) in Polish, if artide was prepared in English). The summary should be prepared in a way allowing a reader to obtaoin essential information contained in the artide. For that reason in the summary author can place numbers of essential formulas, figures and tables from the article.

Pages should have continues numbering.

Main text

Main text cannot contain formatting such as spacing, underlining, words written in capital letters (except words that are commonly written in capital letters). Author can mark suggested formatting with pencil on the margin of the article using commonly accepted adjusting marks.

Text should be written with double line spacing with 35 mro left and right margin. Titles and subtitles should be written with small letters. Titles and subtitles should be numberd using no mor than 3 levels (i.e. 4.1.1.).

Tables

Tables with their titles should be places on separate page at the end of the article. Titles of rows and columns should be written in small letters with double line spacing. Annotations concerning tables should be placed directly below the table. Tables should be numbered with Arabic numbers on the top of each table. Table can contain algorithm and program listings. In such cases original layout of the table will be preserved. Table should be cited in the text.

Mathematical formulas

Characters, numbers, letters and spacing of the formula should be adequate to layout of main text. Indexes should be properly lowered or raised above the basic line and clearly written. Special characters such as lines, arrows, dots should be placed exactly over symbols which they ar attributed to. Formulas should be numbered with Arabic numbers place in brackets on the right side of the page. Units of measure, letter and graphic symbols should be printed according to requirements of IEE (International Electronical Commission) and ISO (International Organisation of Standardisation).

References

References should be placed at the and of the main text with th subtitle „References". Refrences should be numbered (without brackets) adequately to references placed in the text. Examples of periodical [@], non-periodical [2] and book [3] references:

1. F. Valdoni: A new milimetre wave satelite. E.T.T. 1990, vol. 2, no 5, pp. 141–148
2. K. Anderson: A resource allocation framework. XVI International Symposium (Sweden). May 1991. paper A 2.4
3. Y.P. Tvidis: Operation and modeling of the MOS transistors. Nw York. McGraw-Hill. 1987. p. 553

Figures

Figures should be clearly drawn on plain or milimetre paper in the format not smaller than 9 × 12 cm. Figures can be also printed (preferred editor – CorelDRAW). Photos or diapositives will be accepted in black and whit format not gratd than 10 × 15 cm. On th margin of each drawing and on th back side of each ohoto authorp name and abbreviation of the title of article should be placed. Figure's captures should be given in two languages (first in the language the article is writtes in and then in additional language). Figure's captures should be also listed on separate page. Figures should be cited in the text.

Additional information

On the separate page following information should be placed:

- mailing address (home or office),
- phone (home or/and office),
- e-mail.

Author is entiled to free of charge 20 copies of article. Additional copies or the whole magazine can be ordered at publisher at th one's expense.

Author is obliged to perform the author's correction, which should be accomplished within 3 days starting from the date of receiving the text from the editorial stuff. Corrected text should be returned to the editorial stuff personally or by mail. Correction marks should be placed on th margin of copies received from the editorial stuff or if needed on separate pages. In the case when the correction is not returned within said time limit, correction will be performed by technical editorial stuff of the publisher.

In case of changing of workplace or home address Authors are asked to inform the editorial stuff.